Stony Brook University

Novel Processing of Ceramics with Polymorphic Control

A Dissertation Presented

by

Gagan Jodhani

to

The Graduate School

in Partial Fulfillment of the

Requirements

for the Degree of

Doctor of Philosophy

in

Materials Science and Engineering

Stony Brook University

December 2016

Stony Brook University

The Graduate School

Gagan Jodhani

We, the dissertation committee for the above candidate for the

Doctor of Philosophy degree, hereby recommend

acceptance of this dissertation.

Dr. Pelagia-Irene Gouma, Advisor
Adjunct Professor, Materials Science and Chemical Engineering

Dr. Gary Halada, Chairperson of Defense
Associate Professor, Materials Science and Chemical Engineering

Dr. T.A.Venkatesh
Associate Professor, Materials Science and Chemical Engineering
.

Dr. Mingzhao Liu
Adjunct Professor, Materials Science and Chemical Engineering

Dr. Fernando Camino

Staff Scientist, BNL-Center for Functional Nanomaterials.

This dissertation is accepted by the Graduate School

Charles Taber

Dean of the Graduate School

Abstract of the Dissertation

Novel Processing of Ceramics with Polymorphic Control

by

Gagan Jodhani

Doctor of Philosophy

in

Materials Science and Engineering

Stony Brook University

2016

Polymorphism is an important phenomenon exhibited by many materials, including ceramic oxides. The availability of multiple structural configurations for the same chemical composition opens the pathway to a large number of phases with distinct properties. The formation of the crystal structures can be directly correlated to the processing temperature and/or pressure as well as the particle size for nanomaterials. This work focuses on the tailored synthesis of the desired polymorphs of binary and ternary metal oxides through nanoscale processes with emphasis on flame spray pyrolysis.

Flame spray pyrolysis (FSP) is a scalable nano-manufacturing process used for the synthesis of oxide based ceramics. The advantage of this process lies in ease of operation and inexpensive processing as well as the uniformity in the particle size distribution of the products. It is a rapid solidification process involving the atomization of precursor using high temperature gradients and low residence times in the flame. Thus, metastable polymorphs have successfully been synthesized by FSP. Although a wide variety of studies have been conducted on the synthesis and applications of ceramics via FSP there has been scarce knowledge on the actual dynamics of crystal structure formation during the process. Various solution parameters were studied to understand the particle and crystal structure formation for the FSP powders. The process parameters were kept the same; 1.5 slm methane and 3.0 slm O_2 was used as fuel for the flame,

5slm oxygen was used as dispersion gas and the precursor was fed at 5ml/min. MoO_3 was synthesized using different concentrations of precursor and the particle sizes obtained were correlated to the materials parameters such as solution concentration and amount of organic precursor solvent.

Another study was conducted on formation of WO_3 polymorphs using organic precursor salts dissolved in organic solvent. The solution was prepared to obtain low particle sizes and to obtain the metastable ε-WO_3, which only exists below -17ºC in bulk.

The study was further extended to ternary system by synthesizing $VOPO_4$. The effect of solvent on the polymorphic behavior was evaluated. The use of ammonium salts in aqueous solutions led to lower temperatures and resulted information of intermediate compounds and micron sized particles. $VOPO_4$ was easily obtained from the intermediate compounds by calcination. Secondary phases were obtained upon calcination and were related to the processing parameters.

The result of the study showed that the precursor solution had a direct correlation with the formation of different polymorphs through fsp. Aqueous precursors resulted in partial decomposition of solute and resulted in secondary salts with large particle sizes. The addition of organic solvent resulted in formation of a nano-sized particles, the amount of particles formed was directly proportional to the % organic precursor used. Use of a combustible organic solute favors formation of nanoparticles by increasing the flame temperature and lowering the residence time of the particles in the chamber. The smaller sizes and low residence time may result in formation of metastable phases. This study can further be extended to other oxide ceramics and will aid in precursor selection for their synthesis.

Dedicated to

My Family

Table of Contents

List of Figures ix

List of Tables xi

Preface xii

List of Abbreviations xiv

Acknowledgments xv

Vita xvi

Chapter 1: Introduction 1

1.1 Polymorphism 1

1.2 Polymorphism in MoO_3 1

1.3 Polymorphism in WO_3 3

1.4 Polymorphism in $VOPO_4$ 5

1.5 Polymorphism in other oxide ceramics 6

1.6 Applications of polymorphic materials 7

1.7 Factors affecting polymorphism and metastability 10

1.8 Flame spray pyrolysis method 11

1.8.1 Types of Flame Spray Pyrolysis 11

1.8.2 Components of FSP 13

1.8.3 Liquid precursor selection: 14

1.8.4 Mechanism for formation of particles in FSP 14

1.8.5 Formation of metastable phases 16

1.9 Research Statement 17

References 18

Chapter 2: Materials synthesis and characterization methods 25

2.1 Materials Synthesis 25

2.1.1 Sol Gel Synthesis: 25

2.1.2 Electrospinning: Principles and Operation 25

2.1.3 Flame Spray Pyrolysis 27

2.2 Materials characterization techniques 31

2.2.1 X-ray Diffraction (XRD) 31

2.2.2 Scanning Electron Microscopy (SEM) 31

2.2.3 Transmission Electron Microscope (TEM) 32

2.2.4 Fourier Transform Infrared Spectroscopy 33
2.2.5 UV-Vis Spectroscopy 33
2.2.6 Thermal Analysis 33
References 34
Chapter 3: Flame Spray Synthesis and Ammonia sensing properties of pure α-MoO_3 nanosheets 37
3.1 Introduction 37
3.2 Experimental Method 38
3.3 Results 39
3.3.1 X-Ray Diffraction 39
3.3.2 Fourier Transform Infrared Spectroscopy 39
3.3.3 Thermogravimetric analysis 40
3.3.4 Scanning Electron Microscopy 41
3.3.5 Transmission Electron microscopy 43
3.3.6 Ammonia Sensing 45
3.4 Discussion 46
3.5 Conclusion 48
References 48
Chapter 4: Effect of precursor solution on flame spray synthesis of ε-WO_3 polymorphs 51
4.1 Introduction 51
4.2 Experimental Methods 52
4.3 Results 53
4.3.1 X-Ray Diffraction 53
4.3.2 Scanning Electron Microscopy 54
4.3.3 Transmission Electron Microscopy 55
4.3.4 Fourier Transform Infrared Spectroscopy 57
4.3.5 Differential Scanning Calorimetry 58
4.3.6 UV-Vis spectroscopy 58
4.4 Discussion 59
4.5 Conclusion 62
References 62
Chapter 5: Flame spray synthesis of $VOPO_4$ Polymorphs 64
5.1 Introduction 64

5.2 Experimental methods 65
5.2.1 FSP $VOPO_4$ using aqueous solution with sucrose 65
5.2.2 FSP $VOPO_4$ using aqueous solution with DMF 65
5.2.3 Material Characterization 65
5.3 Results 66
5.3.1 X-Ray Characterization 66
5.3.2 Thermal Analysis 67
5.3.3 Fourier Transform Infrared Spectroscopy 68
5.3.4 Scanning Electron Microscopy 70
5.3.5 Transmission electron microscopy 72
5.4 Discussion 74
5.5 Conclusion 76
References 76
Chapter 6: Processing of and phase selection in oxide ceramics through FSP 80
6.1 Scalable manufacturing through FSP 80
6.2 Factors affecting polymorph formation 80
6.3 Precursor selection 81
6.4 Precursor preparation and effect on polymorphic behavior 82
6.5 Polymorphic control through FSP 86
References 87
Chapter 7: Conclusion and future work 90
7.1 Conclusions 90
7.2 Future Research Directions 92
Appendix A: Novel synthesis of Cu-Fe mix metal oxides 94
Appendix B. Self-Supported Nano-WO_3 Foams formed by Self-Assembly of Non-Woven Mats 101

List of Figures

Figure 1-1: Formation of particles from different types of FSP methods, redrawn from ref. #[77] 13
Figure 1-2: Formation of particles through gas phase mechanism 16
Figure 2-1: Electrospinning setup 26
Figure 2-2: Process maps for electrospinning [5] 27
Figure 2-3 Schematic diagram of Flame Spray pyrolysis (FSP) setup[11] 28
Figure 2-4: Principles of formation of particles in FSP [25] 29
Figure 2-5: NPS 10 desktop FSP used in this work (P. Gouma's lab SBU) 30
Figure 3-1: XRD spectra (a) as-synthesized and calcined .68M FSP particles (b) as-synthesized and calcined .05M FSP particles 39
Figure 3-2: FTIR spectra for assynthesized and calcined powders 40
Figure 3-3:TGA analysis of as synthesized particles 41
Figure 3-4: Scanning Electron micrographs for (a,b) 0.68M as-synthesized, (c,d) 0.05M as-synthesized, (e,f) 0.68M calcined, and (g,h) 0.05M calcined powders 42
Figure 3-5: TEM images and corresponding SAED patterns for (a,e) 0.68M as-synthesized (b,f) 0.05M as-synthesized (c,g) 0.68M calcined and (d,h) 0.05M calcined particles 44
Figure 3-6: (a) Sensing data for ammonia at 485^{0}C (b) Sensitivity plot for ammonia 45
Figure 3-7: Process map for fsp of Mo-precursors 47
Figure 4-1: X-ray diffraction pattern for (a) As-synthesized pure WO_3 (b) calcined pure WO_3 (c) As-synthesized Cr-doped WO_3 (d) calcined Cr-doped WO_3 53
Figure 4-2: (a) Scanning Electron Micrograph for Cr-doped WO_3 (b) EDS for Cr-doped WO_3 55
Figure 4-3**:** TEM images and corresponding SAED patterns for (a,e) pure WO_3 as-synthesized (b,f) Cr-doped WO_3 as-synthesized (c,g) pure WO_3 calcined and (d,h) Cr-doped WO_3 calcined particles 57
Figure 4-4: FTIR characterization of as-synthesized nanopowders 57
Figure 4-5: DSC (a) pure WO_3 (b) Cr-doped WO_3 58
Figure 4-6: UV-Vis spectra for pure and Cr-doped WO_3 particles. 59
Figure 4-7: process map for formation of WO_3 particles through fsp 60
Figure 5-1: Results of XRD analysis of (a)as-synthesized and (b)calcined powders (A: Ammonium Vanadyl Hydrogen phosphate hydrate ($NH_4VOVO_2(HPO_4)_2.1.5H_2O$), α: α-$VOPO_4$, β: β- $VOPO_4$, δ: δ-$VOPO_4$) 66
Figure 5-2: TGA-DTA analysis for (a) FSP powders with sucrose (b) FSP powders with DMF 68
Figure 5-3: FTIR images for (a) as-synthesized and calcined FSP DMF powders (b) assynthesized and calcined FSP sucrose powders 69
Figure 5-4: Scanning electron microscopy images for as-synthesized particles from (a,b,c) sucrose based solutions (d,e,f,) DMF based solutions 71
Figure 5-5: Scanning electron microscopy images for calcined particles from (a,b,c) sucrose based solutions (d,e,f,) DMF based solutions 72
Figure 5-6: TEM images and corresponding SAED pattern for as-synthesized particles from (a,b,c) sucrose based solutions (d,e,f,) DMF based solutions 73
Figure 5-7: TEM images and corresponding SAED pattern for calcined particles from (a,b,c) sucrose based solutions (d,e,f,) DMF based solutions 74
Figure 5-8: Process map for fsp synthesis of powders 75

Figure A-1: XRD of self-supported $CuFe_2O_4$ grids 95
Figure A-2: UV-Vis spectra of $CuFe_2O_4$ after calcination at 400 and 500°C 96
Figure A-3: SEM images of (a) electrospun PVP+$FeNO_3$ nanofibers (b) High-magnification image of electrospun PVP+$FeNO_3$ nanofibers (c) $CuFe_2O_4$ grids calcined at 400°C (d) High-magnification image of $CuFe_2O_4$ grids calcined at 400°C (inset EDS spectra) (e) $CuFe_2O_4$ grids calcined at 500°C (f) High-magnification image of $CuFe_2O_4$ grids calcined at 400°C (inset EDS spectra) 97
Figure A-4: TEM images and SAED patterns for (a) samples calcined at 400°C (b) high magnification image for samples calcined at 400°C (c) SAED pattern for samples calcined at 400°C (d) samples calcined at 400°C (e) high magnification image for samples calcined at 400°C (f) SAED pattern for samples calcined at 400°C 98
Figure B-1: X-ray Diffraction pattern for foam structure 103
Figure B-2: FTIR spectra of foams 104
Figure B-3:a) SEM image of as spun fibers, highlighting the formation of honeycomb structures b) High magnification SEM image of fibers highlighting the sol particles in the fibers c) SEM image of foam structures obtained after thermal treatment at 375^0C d) High magnification SEM image of foam surface showing the agglomerated sol particles and nano porosity. 105
Figure B-4: SEM image of thermally treated spin coated films coated (a,b) 3 times, (c,d) 2 times (e,f) 1 time 106
Figure B-5: (a, b) TEM images and SAED pattern of foam structure respectively 107
Figure B-6: (a) UV-Vis absorption spectra of foam (b) the plot of band gap energy and $(\alpha h\nu)^2$ of WO_3 foam 108

List of Tables

Table 1-1: MoO_3 Polymorphs 2
Table 1-2: WO_3 polymorphs 3
Table 1-3: Average bond lengths (angstroms) in $VOPO_4$ polymorphs[35] 5
Table 1-4: Polymorphic metal oxide sensors 7
Table 3-1: morphology and particle size for fsp powders 45
Table 4-1**:** Phase content and size of WO_3 nanopowders based on the XRD data 54
Table 4-2: Particle sizes of WO_3 Nanopowders based on TEM images 55
Table 5-1 Phase content and crystallite sizes for FSP $VOPO_4$ 67
Table B-0-1 Reported Band Gap values for WO_3 Structures 108

Preface

The work done here focuses on understanding and controlling formation of polymorphs through FSP. Different ceramics are evaluated by varying the precursor parameters and polymorphic formation and transitions are evaluated.

Chapter 1 introduces the concept of oxide polymorphism and discusses polymorphism in various ceramics. Subsequently importance of polymorphic ceramics with respect to applications is discussed. The factors that affect polymorphic behavior for ceramics and flame spray pyrolysis process are also discussed.

Chapter 2 focuses on the experimental details and both synthesis techniques and characterization techniques used for flame synthesized nanomaterials.

Chapter 3 discussed the formation of MoO_3 through FSP. The particles are processed by varying the concentration of metals in precursor solution and varying the organic content in the solvent. The phase and morphology of synthesized particles as well as particles obtained upon calcination are analyzed and discussed.

Chapter 4 focuses on novel synthesis of metastable ε-WO_3 through fsp process. The effect of using a combustible solute on the formation of ε-WO_3 is discussed. The results are compared with an earlier study that led to synthesis of ε-WO_3 with the help of Cr as dopants. Further the phase stability and retention of ε-WO_3 upon calcination are discussed.

Chapter 5 analyzes the formation of $VOPO_4$ polymorphs through fsp. The effect of organic content on phase and morphology of the particles are discussed. Further phase formation and changes are discussed upon calcination. The study relates the type of precursor used to the size and polymorphic behavior of final products.

Chapter 6 discusses the parameter that govern the synthesis of polymorphs through FSP. The effect of precursor with respect to polymorph formation and particle size through fsp are discussed. An overview is generated on selection of precursors to monitor temperature of operation and control phase formation through FSP.

Chapter 7 lists the concluding remarks from the study and outlines the future research directions.

List of Abbreviations

LVP: Lithium Vanadium Phosphate

FSP: Flame Spray pyrolysis

VAFS: Vapor Assisted Flame Spray Pyrolysis

FASP: Flame Aerosol Spray Pyrolysis

LF-FSP: Liquid Feed Flame Spray Pyrolysis

ODOP: One Droplet to One Particle

ODMP: One Droplet to Multiple Particles

XRD: X-Ray Diffraction

SEM: Scanning Electron Microscopy

EDS: Energy Dispersive Spectra

TEM: Transmission Electron Microscopy

SAED: Selected Area Electron Diffraction

FTIR: Fourier Transform Infrared Spectroscopy

UV-Vis: Ultraviolet- Visible light Spectroscopy

TGA: Thermogravimetric Analysis

DTA: Differential Thermal Analysis

DSC: Differential Scanning Calorimetry

JCPDS: Joint Committee on Powder Diffraction Standards

RT: Room temperature

SA: Surface area

3D: Three-dimensional

Acknowledgments

I would like to offer my sincerest gratitude to my supervisor, Prof. P. I. Gouma. Prof. Gouma has been a great mentor and support throughout the whole period of my Ph.D. study in all aspects. Her enthusiasm, her inspiration, as well as her constructive criticisms have been of great value for me. A short paragraph cannot be enough to thank her for her guidance and patience for past so many years. It would not have been possible to complete this doctoral thesis without her mentorship and support. I will always be grateful to her for accepting me as her Ph.D. student and introducing me to this field.

I would like my committee members Prof. Gary Halada, Prof. Venkatesh, Dr. Liu and Dr. Camino for their helpful suggestions and insightful comments on my thesis. I thank to Jim Quinn for helping and allowing me to use SEM and XRD at his facility. I am also thankful to Kim Kisslinger for his strong technical support on TEM at Brookhaven National Laboratory. My express my sincere gratitude towards Prof. Dilip Gersappe for his help and support as a graduate program director and also Mrs. Chandrani Roy for assisting me with various issues during my graduate studies. I would like to extend my thanks to all my current and past group members specially Jusang Lee, Selda Topcu, Owen Abe, Shantanu Sood and Wen-Ling Liao for their support.

I would also like to extend my thanks to all my friends who have extended their support to me throughout my Ph.D.: Pilar Espitia, Sumantu Iyer, T.Srivatsa Bhat, Saurabh Patel, Shishir Dash, Cagla Tasdemir, Gopal Diwedi, and Prashant Jha. Most of all, I would like to thank my parents for their love and support for me at all times.

Vita

Gagan Jodhani

EDUCATION

Stony Brook University, Stony Brook, NY

M.S., Materials Science and Engineering, Dec. 2010

National Institute of Technology Warangal, Warangal, India

B.Tech, Metallurgical & Materials Engineering, Apr. 2007

Experience:

Graduate Research Assistant, Center for Nanomaterials and Sensor Development,

Jan 2011- Present

Teaching Assistant, Department of Materials Science and Engineering, Stony Brook University

Aug 2011- Dec 2013

Guest Research Assistant, Brookhaven National Laboratory

May 2012- Present

Graduate Assistant for Department Website, Department of Materials Science and Engineering, Stony Brook University

Mar 2015- Present

Publications

Gagan Jodhani, Jiahao Huang and Pelagia I.Gouma, **"**Flame Spray Synthesis and Ammonia sensing properties of pure α-MoO3 nanosheets", Journal of Nanotechnology (In press)

Gagan Jodhani, Selda Topcu, Aisha Bishop-Haynes, Jusang Lee and Pelagia I.Gouma, "Self-Supported Nano-WO3 Foams formed by Self-Assembly of Non-Woven Mats", Journal of Advances in Nanomaterials (2016)

Selda Topcu, **Gagan Jodhani** and Pelagia I. Gouma, "Optimized Nanostructured TiO_2 Photocatalysts", Frontiers in Materials (2016)

Mehrnaz Mojtabavi, **Gagan Jodhani**, Ramya Rao, Jing Zhang and Pelagia-Irene Gouma, "A PANI–Cellulose acetate composite as a selective and sensitive chemomechanical actuator for acetone detection", Advanced Device Materials (2016)"

Chapter 1: Introduction

1.1 Polymorphism

According to reported literature, the concept of polymorphism was first discovered by Klaproth in 1798 by showing that the composition of calcite and aragonite is same. However, it wasn't until 1820s when polymorphism became a widely accepted phenomena when Mitscherlich stated polymorphic behavior in arsenates, phosphates and sulfur. Mitscherlich's "law of isomorphism" stated: Substances that crystallize in isomorphous forms (i.e. have identical crystalline forms and form mixed crystals) have similar chemical compositions. Since then polymorphism has widely been studied in bulk metal oxides. With the growing interest of nanoscience, new polymorphic states have been discovered for various materials; which were not feasible in bulk solids. For nanocrystalline ceramics, it was shown that certain compounds differ significantly from their bulk state phase transformation properties when they are subjected to similar conditions at nanoscale. The structure and polymorphs for various polymorphs are discussed in detail in the sections to follow.

1.2 Polymorphism in MoO_3

MoO_3 exhibits two polymorphic states in bulk, these two polymorphs are an orthorhombic α-MoO_3 and a monoclinic β-MoO_3. α-MoO_3 is the thermodynamically stable form for MoO_3 at room temperature while β-MoO_3 is kinetically stable form. For nanocrystalline solids, additional polymorphic states have been discovered for nanocrystalline MoO_3. A hexagonal MoO_3 was reported by low temperature hydrothermal method[1]. Table 1.1 lists the particle sizes & morphology, synthesis methods and conditions for formations of MoO_3 polymorphs.

The structure of MoO_3, comprises of MoO_6 octahedra. α-MoO_3 exhibits a layered structure, in which each layer is built up with MoO_6 octahedron at two levels. The octahedrons are connected together in y-direction, which result in zigzag rows[2]. For each MoO_6 octahedra there is only one O atom doubly bonded to Mo, all others oxygen atoms are shared by the different MoO_6 octahedrons. For β-MoO_3 the structure is similar to WO_3 and is related to the three-dimensional ReO_3 structure[3], which consists in corner-connected octahedral network. The β-MoO_3

exothermically transforms into α-phase at temperature above 400ºC and moderate heating rates. However, it has been shown that MoO_3 can be stabilized into ReO_3 structure by partial substitution with tungsten[4].

Table 1-1: MoO_3 Polymorphs

Phase	Synthesis Technique	Morphology	Particle size	Conditions P & T	Reference
α-MoO_3	Acidification & Hydrothermal Synthesis	nanorods	50nm dia. 150-300nm length	170-180ºC	[5]
	Thermal Evaporation	Nano sheets	1.4nm thickness	400ºC	[6]
	Topochemical synthesis	nanoplates	1-2 µm length nm thickness	550ºC	[7]
	Electrospinning	Single crystal nanorods	10-50nm dia.	500ºC	[8, 9]
β-MoO_3	Low temperature deposition	Thin films	100-200nm	200ºC	[10]
	Atmospheric microplasma	Nanosheets	1-2 µm length	RT	[11]
	Vacuum drying	-	-	250ºC	[12]
	Sol gel	Nanoparticles	50nm	<450ºC	[13, 14]

h-MoO_3	Solvothermal process	rods	500-800nm dia.	60-100ºC	[15]
	Acidic reaction	Nanorods	40nm diameter	190ºC	[16]
	Hydrothermal treatment	Rods	6-7µm diameter	100ºC	[17]
	Hydrothermal route	Nanobelts	20-30nm thick	150ºC	[18]
	Sonochemical method	Nanorods	.2-1.2µm width	50ºC	[19]

1.3 Polymorphism in WO_3

In bulk, WO_3 exhibits a monoclinic ε-phase between the temperature ranges of -273°C to -40°C; a triclinic δ-phase is found between -40°C to 17°C. The stable phase for WO_3 at room temperature is the monoclinic γ-phase that exists between the temperature ranges of 17-330°C. Over the temperature range of 330 WO_3 exhibits two more crystalline states which are an orthorhombic β-phase (330-740°C) and a tetragonal α-phase (740-900°C)[20]. However, the transition in nanocrystalline materials is different from bulk. The synthesis methods and conditions used greatly affect the phase of the materials. Two metastable phases have been reported for WO_3 which are a hexagonal phase[21] and a cubic phase[22], which didn't exist in bulk compounds. The nanocrystalline polymorphs of WO_3 are described in table 1.2.

Table 1-2: WO_3 polymorphs

Phase	Synthesis Technique	Morphology	conditions	Particle size	Reference
γ-WO_3	Flame Spray pyrolysis	Nanoparticles	RT	5-10nm	[23]

	Microwave assisted hydrothermal method	Nanoparticles	50-100nm	500-700ºC	[24]
	E-beam	Nanowires	20-30nm dia.	RT	[25]
	Sol gel	Nanoparticles	10-20nm	400ºC	[26]
h-WO_3	Microwave assisted hydrothermal method	Nanoparticles	20-50nm	250ºC	[24]
	Sol gel	Nanowires	40 nm dia.	400ºC	[21]
	Sol gel and hydrothermal synthesis	Nanorods	100-200nm dia.	180ºC	[27]
Cubic-WO_3	Sol gel	Nanoparticles	30-40nm	350ºC	[25]
	Sol gel	Petal shaped nanoparticles	200nm	250ºC	[28]
δ-WO_3	Pulsed laser deposition	Thin film	200nm	400ºC 150-200mTorr	[29]
	Sol gel	Nanoparticles	30-50nm	400-600ºC	[30]
	Sol gel	Nanoplates	50-80	250-500ºC	[31]
ε-WO_3	Flame spray pyrolysis	Nanoparticles	10-20nm	RT	[32]

	Magnetron sputtering	Nanoparticles	10-20nm	100-400ºC	[33]

1.4 Polymorphism in $VOPO_4$

There are seven reported polymorphs for $VOPO_4$. Among these polymorphs, four exhibit tetragonal structure (α_1, α_2, δ and ω), two exhibit orthorhombic structure (β and γ) and one monoclinic structure (ε) [34]. Among these polymorphs, β-$VOPO_4$ is of the lowest energy configuration. However, these polymorphs have been synthesized using various routes, although, due to close relation in the structures of all the polymorphs and their low energy difference, obtaining a single phase is almost impossible[34].

The structure of $VOPO_4$, comprised of VO_6 octahedron connected by PO_4 tetrahedron. However, due to long length of V---O bond, it is sometimes reported as a VO_5 pyramid, with a short O=V bond and a long V---O bond. The governing factor in formation of $VOPO_4$ polymorphs is caused by the bond length of V---O bonds, all other bonds exhibit similar lengths. The bond lengths for different polymorphs are shown in table 1.3.

Table 1-3: Average bond lengths (angstroms) in $VOPO_4$ polymorphs[35]

Polymorph	V=O	V---O	V-O	P-O
α_I-$VOPO_4$	1.57	2.67	1.85	1.55
α_{II}-$VOPO_4$	1.57	2.97	1.83	1.54
β-$VOPO_4$	1.57	2.57	1.85	1.55
ε-$VOPO_4$	1.57	2.63	1.84	1.54
δ-$VOPO_4$	1.56	3.14	1.84	1.54

1.5 Polymorphism in other oxide ceramics

Tin Oxide (SnO_2) exhibits five different polymorphs, the observed phases are a rutile type (tetragonal), $CaCl_2$ type (orthorhombic), α-PbO_2 type (orthorhombic), pyrite-type (cubic), ZrO_2 type (orthorhombic), contunnite-type (orthorhombic)[36]. The rutile-type phase and $CaCl_2$-type orthorhombic phase are the two most common and important polymorphs of SnO_2.

Titanium dioxide (TiO_2) occurs naturally in three different polymorphs, all of which exhibit TiO_6 octahedra, the coupling between the octahedral is slightly different among different octahedras[37]. The polymorphs of TiO_2 are anatase (tetragonal), rutile (tetragonal) and brookite (orthorhombic). Rutile is the thermodynamically stable form of TiO_2 at all temperatures and pressures, while anatase and brookite are kinetic products[38].

Vanadium Oxides (VO_2 and V_2O_5) exist in 2 forms due to the valency of V atoms. The +4 valency gives rise to VO_2, which exhibits two polymorphs. The polymorphs for VO_2 are a monoclinic phase and a tetragonal rutile type structure[39]. V_2O_5 on the other hand, exhibits multiple polymorphs, such as, α-V_2O_5 (monoclinic), β-V_2O_5 (monoclinic or tetragonal)[40] and γ-V_2O_5 (orthorhombic)[41]. Many metastable phases have also been reported from deintercalation of metal atoms from $M_xV_2O_5$ [42].

Manganese Oxide (MnO_2) exhibits two different polymorphs, namely, α-MnO_2 (tetragonal)[43] and β-MnO_2 (rutile type structure)[44]. Another reported structure for MnO_2 is the γ-MnO_2 which has a mixed ramsdellite and pyrolusite domains, upon heating the ramsdellite phase converts to pyrolusite[45].

Iron Oxide (Fe_2O_3) exists in four different polymorphs, namely, α- Fe_2O_3 (hexagonal), β- Fe_2O_3 (BCC), γ- Fe_2O_3 (BCC), and ε- Fe_2O_3 (orthorhombic)[46]. The β and ε phases are metastable and only exist in nanocrystalline solids. While both α and γ polymorphs exist naturally.

Zinc Oxide (ZnO) is reported to exhibit three polymorph, wurtzite (hexagonal B4), zinc-blende (hexagonal B3) and rock-salt (hexagonal B1)[47]. Wurtzite is the stable structure for ZnO, it transforms into B1 structure at high pressure.

1.6 Applications of polymorphic materials

Nanocrystalline ceramics have properties much different from their bulk counterparts. For e.g. the ε-phase for WO_3 is very important for gas sensing applications as it acts as a selective sensor for acetone detection[32]. Many other examples exist where nanocrystalline materials offer better results and are key towards the applications. These materials are discussed in more detail below and are categorized according to their applications.

I. Gas Sensing

The behavior of nanocrystalline metal oxides for gas sensing has been outlined by Gouma[48], gas selectivity is achieved with the help of specific crystallographic phase of a pure metal oxide. Conductimetric sensors based on semi-conducting oxide, offer low cost detection for reducing gases. The operation principles are associated with adsorption of gas molecules on the surface of the materials. The adsorption induces electric charge transport in the materials due to which the resistance of oxide changes[49]. The operating temperature for these sensors vary from 100-500ºC, the selectivity of gas at a particular temperature has been related to the crystal structure of the materials. Table 1.4 lists different materials and their polymorphs that have been applied as gas sensors.

Table 1-4: Polymorphic metal oxide sensors

Material	Polymorph	Gas selectivity	Operation temperature	Ref.
MoO_3	α-MoO_3	Ammonia	450ºC	[9, 13, 14]

		NO/NO_2	450ºC	[13, 14]
		H_2S	375ºC	[50]
	$\alpha + \beta$	Methanol	400ºC	[51]
		Isoprene	420ºC	[51]
WO_3	ε-WO_3	Acetone	400ºC	[32]
	γ-WO_3	NO	400ºC	[26, 52]
	h-WO_3	Ammonia	300ºC	[53, 54]
In_2O_3	Cubic	H_2	240ºC	[55]
	Cubic	NO_2	150ºC	[56]

II. Photocatalysis

Photocatalysis refers to the increase in the rate of a photoreaction in the presence of a catalyst. The photocatalytic activity (PCA) depends on the ability of a catalyst to create electron–hole pairs. These electron-hole pairs result in generation of free radicals like hydroxyl groups which are able to undergo secondary reactions. Titania is a widely used photocatalyst, its ability for water catalysis was discovered in 1970s[57]. Titania has two primary phases, rutile and anatase, both having different band gaps. Rutile exhibiting a lower band gap (3.0 eV) in comparison to anatase (3.2 eV) which can cause it to be excited by irradiation at longer wavelengths whereas anatase generally exhibits superior photocatalytic activity to rutile as a result of a significantly higher surface area and thus higher levels of adsorbed radicals[58, 59]. A recent study in our group resulted in nanofibers containing rutile and anatase phase[60]. The content of anatase/rutile was dependent on the calcination temperature. The results observed showed that the TiO_2 nanostructures containing a 90/10 anatase/rutile percentage, offered best photocatalytic properties. This material was active in visible light region, which was attributed to the growth of small rutile lathes on anatase grains. The photocatalytic activity dropped with the increase in rutile content.

Similarly, J.Y. Ying et al.[61] have earlier reported that grain size plays an important role in photocatalytic property of a material. . In their study, Ying et al., found the photocatalytic

activity of nanocrystalline titania was dependent on particle size. They reported that the maximum photocatalytic efficiency was obtained for a particle size of 10nm, a higher or lower particle size reduced the photocatalytic efficiency of titania nanocrystals. Our study is in accordance with the literature where the sample with smallest particle size (TiO_2 450, ~7nm) exhibited lower photocatalytic activity compared to the sample with a slightly bigger particle size (TiO_2 500, ~15nm). The photocatalytic activity further degraded as the particle size increased.

III. Li-ion batteries

Rechargeable batteries have always been a good power source for a wide variety of applications due to the fact that they are light weight, rechargeable and cost effective. Currently almost all electronic portable devices depend on Li-ion batteries for power.

A typical Li-ion battery consists of a cathode, an anode and an electrolyte for charge transport. A lot of research is being carried on to increase the capacity and recharging rates of these batteries. This is where metal oxides come in handy. It has been shown that transition metal oxides as negative electrodes are better than the conventional graphite electrodes used in Li-ion batteries as they demonstrate higher electrochemical capacity [62]. Oxides of transition metals such as Fe, Ni, Co, Mn, Sb, Sn etc. Nanostructured metal oxides are good choice for the anodes as they provide large surface area, also their porous nature enhances the diffusion of Li^+ ions which in turn yields in higher charge capacity.

Polymorphic metal oxides have also been used as a dopant on the cathode in Li-ion batteries. These electrodes are made as nanostructured Lithium Transition metal oxides and are low in cost, have high energy density and excellent cycle life than Lithium electrodes. Some of the examples of such materials are $LiCoO_2$[63], $LixNiO_2$[64], $LiMn_2O_4$[65]etc.

The polymorphic behavior of materials is an important phenomena w.r.t. batteries, as different polymorphs act differently to Li-ion insertion/extraction. For e.g. lithium vanadium phosphate, $Li_3V_2(PO_4)_3$ (LVP), has emerged as promising new cathode material due to the abundance of the transition metals, high thermal stability, and intrinsically high capacity (197 mAh/g) and high working potential (~ 4V) [66]. Apart from high capacity, the operating voltage which in turn gives the battery high specific energy, is suitable for electric vehicle use[67]. There

are two known polymorphs of LVP, the rhombohedral[68] and monoclinic phase[66]. The monoclinic phase of LVP is more thermodynamically stable and more appealing for lithium ion diffusion pathway with 3 Li^+ being (de) intercalated, whereas rhombohedral LVP, allows de-intercalation of 2 Li^+, with the electrochemical reinsertion only feasible for 1.3 Li^+.

1.7 Factors affecting polymorphism and metastability

I. Particle size

Particle size plays an important role in formation of a polymorphs. Low particles/grain size is beneficial for formation and stabilization of metastable polymorphs. Such was the case for formation of ε-WO_3 at room temperature[32]. The particles produced by fsp showed that smaller sized particles contained ε phase, whereas, larger sized particles formed a stable γ-polymorph. Upon annealing the content of ε-phase lowered as the particle sizes increased. Similarly, a study conducted on formation of titania at different annealing temperatures, resulted in formation of anatase for small grain sizes and low annealing temperature[60]. Increase in annealing temperature led to increase in grain size and thereby formation of rutile phase. Vast literature exist on the polymorphic transitions based on critical particle sizes.

A study conducted by our group resulted in formula for calculation/prediction of the critical size for a phase transformation[69]. The critical particle size is calculated by following equation:

$$r_c^{\beta\rightarrow\alpha}(T)= \{[M.(\gamma^\alpha/\rho^\alpha- \gamma^\beta/\rho^\beta+2.f_s^\beta/\rho^\beta-2.f_s^\alpha/\rho^\alpha)/(\Delta^\infty H_f^\alpha(T)- \Delta^\infty H_f^\beta(T))]\}-\alpha/2$$

Where,

$r_c^{\beta\rightarrow\alpha}(T)$ is the critical particle size required for β to α transformation at temperature T

M is the molar mass

γ is the interfacial energy

f_s is the surface stress due to excess internal pressure

ρ is the density of the phase

$\Delta^{\infty}H_f^{\alpha}(T)$- $\Delta^{\infty}H_f^{\beta}(T)$ is the difference of enthalpy of formation between α & β at temperature T

Based on the above equation, the critical particle size can be calculated and predicted for a phase transformation.

II. Processing parameters

For bulk solids, high temperatures and pressures are required for formation of metastable compounds. However, the same metastable components can be formed in nano-size at RT and 1atm pressure. The formation of metastable compounds has been related to Gibb's free energy; a material, during nucleation, will exhibit a polymorph that has lowest free energy at a particular temperature and pressure. At a given thermodynamic condition, both metastable and stable phases may coexist, but only one of the two phases is stable, with minimal free energy, and the other must be metastable and may transform into a stable state[70]. The free energy of a polymorph is governed by size, temperature and pressure. A slight change in either one of the condition may affect the formation of a polymorph.

To achieve a metastable form at room temperature, rapid solidification/quenching of these materials[71, 72]. Number of studies exist on the formation of metastable complexes at room temperature by obtaining nano-crystalline solids by quenching from high temperatures. Among the various methods used, flame spray pyrolysis is of prime interest as the process offers high temperature gradient and low residence time (start of nucleation-quenching)[73]. Thus, making it favorable towards formation of metastable phases. The process is described in detail in the section to follow.

1.8 Flame spray pyrolysis method

1.8.1 Types of Flame Spray Pyrolysis

Flame spray pyrolysis reactors have been categorized into three different categories, which are discussed below. The schematics of particle formation through different processes are shown in figure 1.1

I. Vapor Assisted Flame Spray Pyrolysis (VAFS)

VAFS is a commonly used industrial process for synthesis of various ceramics, such as, fumed silica, alumina and pigmentary titania[74]. The process uses volatile metal precursors, which are evaporated and then fed into a flame. The metal particles are converted into oxides and particle formation occurs by nucleation from gas phase. The major drawback of the process is its need for volatile precursors, which limits the variety of products that can be generated through the process.

II. Flame Aerosol Spray Pyrolysis (FASP)

FASP used non-combustible liquid metal precursors, the precursor liquid are dispersed into tiny droplets and pyrolyzed by an external flame[74]. Aqueous solutions of metallic salts are generally used, the flame is usually generated by hydrocarbons or H_2/O_2. Upon evaporation, the particle formation is similar to VAFS.

III. Liquid Feed Flame Spray Pyrolysis (LF-FSP)

LF- FSP was developed by R.M Laine at University of Michigan, Ann Arbor[75]. The liquid fed FSP was able to overcome the drawback of FASP by fabricating more complex metal oxide particles. The process uses a metal oxide precursor in the form of liquid; its composition is generally in the form of metal chlorides, metal nitrates or metal acetates dissolved in aqueous or alcohol based solutions[76]. The process features short residence times (a few milliseconds) and results in formation of homogenous, nanosized particles.

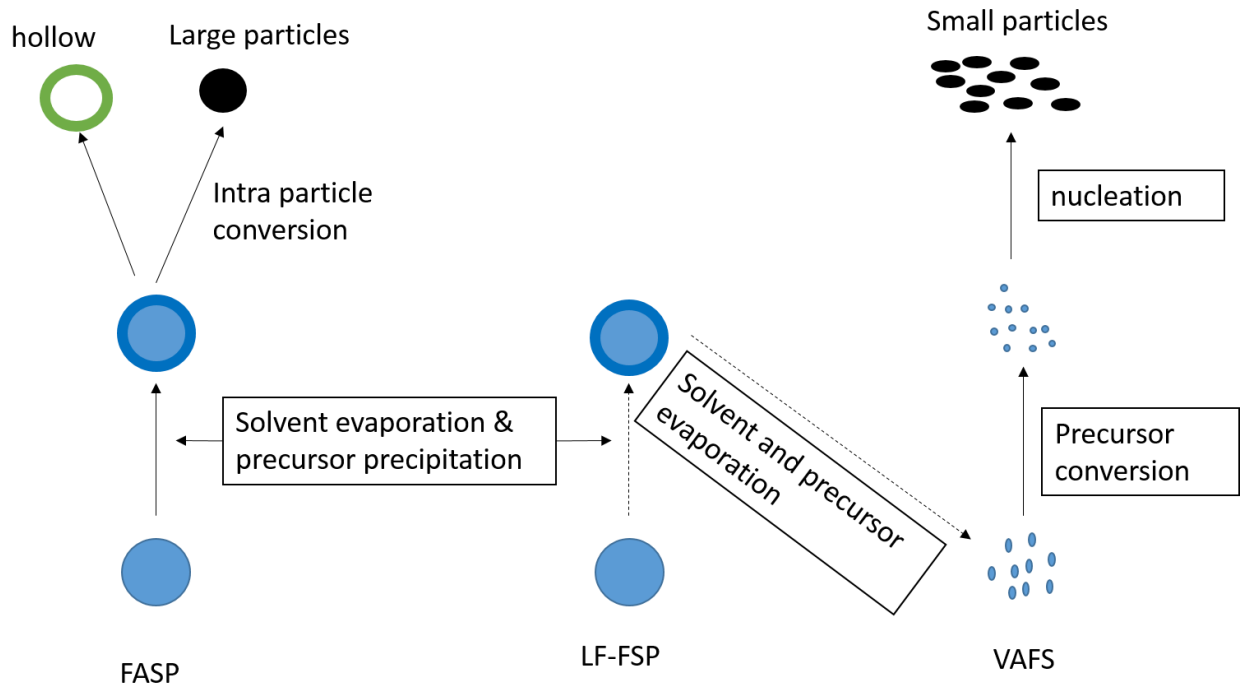

Figure 1-1: Formation of particles from different types of FSP methods, redrawn from ref. #[77]

1.8.2 Components of FSP

I. Atomizer: The purpose of Atomizer is to create droplets, three different kinds of atomizer[78] exist and are described below.

a) Ultrasonic nebulizer: Ultrasonic nebulizers form sprays using high-frequency vibrations and converting liquid into mist. The mist enters the flame and follows the VAFS route, giving small particles.

b) Two-fluid nozzle: A two-fluid nozzle is a device that disperses liquid into spray, the breakup of liquid into spray occurs with the help of an atomizing gas.

c) Electrosprayer: An electrosprayer uses high voltage to convert liquid into aerosol. It is useful for producing ions from macromolecules.

A two-fluid nozzle is the most commonly used atomizer for FSP system.

II. Burner: The purpose of burner is to generate a flame. Two different types of burner exist, which are, a premixed burner and a diffusion burner. The premixed burner mixes the fuel and oxidant[78]. FSP generates a self-sustaining flame so that the burner system for it is an ignition source. The advantage for it is that it could directly control the particle size by controlling the combustion enthalpy and the metal concentration of the precursor[73].

III. Collector: The purpose of collector is to collect the final product from FSP process. Usually a substrate or a filter is used for collection of particles.

1.8.3 Liquid precursor selection:

The selection of liquid precursor is an important step in FSP particle synthesis. The selection of metallic precursor and solvent should be performed with keeping various factors in mind, such as, melting/decomposition temperatures, miscibility and chemical stability. These factors govern the overall particle formation in flame. Nitrates, actetates and acetylacetonates are the natural choices for FSP as they were economical and readily available. However, they do not always yield homogeneous morphology[73].

The low combustion enthalpies of precursors coupled with high melting points results in formation of in-homogenous particles[79]. However, this drawback can sometimes be remediated by processing parameters. Following is how the particle formation is affected by liquid precursor formulation.

Hollow particles are formed when the boiling point of solvent is less than the melting point of solute or if the metal precursor precipitates on the surface of solvent. These parameters can be overcome by providing sufficient heat to the precursor. For formation of homogenous particles the melting point of precursor solute should be lower than the boiling point of solvent.

1.8.4 Mechanism for formation of particles in FSP

I. One droplet to one particle (ODOP)

As the name suggests, the formation of particles through this mechanism is by conversion of a single droplet into a single particle. The first step involves solvent evaporation and allows

solute to disperse in the reactor. The solute then reacts with carrier gas or one-another to form particles. In final step, the particles undergo sintering and densification. The resultant of ODOP mechanism, yields particle in the micron size range. A process usually follows ODOP when the melting point of solute is higher than solvent[73].

The particle size for ODOP[78] can be predicted and is given by:

$$dp = \left(\frac{CMd^3}{n\rho}\right)^{1/3}$$

Where,

dp is the average particle size

C is the concentration of the droplet

d is the diameter of the droplet

M is the molecular weight of particles

N is the stoichiometric ratio

ρ is the particle density

II. One droplet to multiple particle (ODMP)

The steps involved in this mechanism are similar to that of ODOP. The difference between the two mechanisms is based on the precursor. Precursors tend to follow ODMP if there is presence of an organic additive. The additive leads to crack down of particles during the sintering process, which results in formation of multiple particles. The particles obtained exhibit a wide size range and are usually nano-crystalline[78].

III. Gas phase mechanism

For this mechanism, the precursor is an organometallic compound. The precursor evaporates quickly once it enters the flame, producing metal vapors. The formation of particles occur in various steps[73] and are given as a flow chart in fig. 1.2 below:

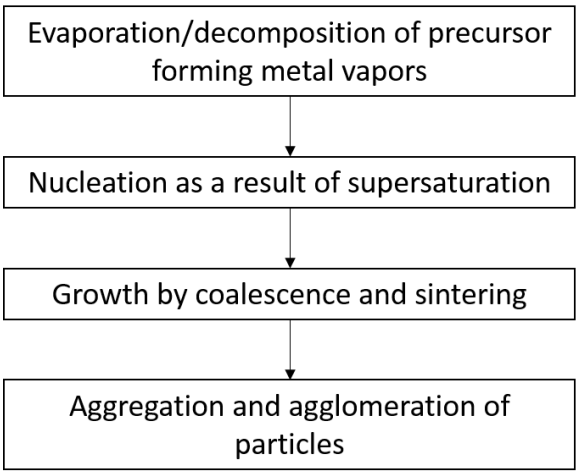

Figure 1-2: Formation of particles through gas phase mechanism

In the gas phase mechanism, the metal vapor could collide with the carrier gas to nucleate and thereby forming clusters. Alternatively, the vapor could also nucleate on the surface of formed clusters resulting in new particles growth. The higher the number of clusters being formed, the higher is the probability for them to collide with each other and form strong adhesive (physical) bonds or chemical bonds. The formation of bonds result in coagulation to produce nanoparticles. Finally, these nanoparticles produce single particles during coalescence process. The coalescence process results in aggregation of particles in the high temperature zone. To control the particle size by not allowing them to aggregate into larger particles, the lower residence time of precursor is needed[78]. The lower residence time can be achieved by a higher flow-rate of the precursor solution or high organic content of the organic precursor solvent, which results in bigger flame height.

1.8.5 Formation of metastable phases

Flame spray pyrolysis has resulted in formation of many metastable ceramics. The high temperature of operation coupled with rapid solidification and small particle sizes offer perfect conditions for formation of metastable polymorphs[73]. The size of particles formed through FSP are affected by various parameters such as composition of precursor, fuel and dispersion/oxidant flow rate, size of droplet and temperature of flame[80]. The parameters are inter-related as a high oxidant flow gives rise to low flame temperature, a non-combustible solute lowers the flame

temperature, and lower oxidant flow rate decreases the droplet atomization and yields larger droplet. Controlling the parameters, an optimum particle size and phase distribution can be obtained from same precursor. The parameters also affect the formation of a polymorph. For e.g. a metastable tetragonal-$BaTiO_3$ was reported using fsp[81], organic precursors of Ba and Ti were used in HNO_3 and citric acid. Pure phase with low particle size was achieved for precursor with highest concentration of citric acid and was associated with lower residence time of the vapors. In another study by a different group, the same recipe was used except citric acid was replaced with water[82]. The addition of water to the precursor mixture resulted in lower flame temperatures, bigger particle sizes and formation of a cubic-$BaTiO_3$ phase. The lower flame temperature due to addition of water, increases the residence time for the particles which in turn leads to formation of larger particles and stabilization of the cubic polymorph. Organic precursors (organic solute in organic solvent) offer the best chance at formation of metastable polymorphs as they offer a high temperature gradient and low residence time.

1.9 Research Statement

There is an abundance of polymorphic reactions in ceramics, due to the availability of numerous configurations. The availability of metastable structures offer a wider variety of possible configurations. Each configuration offers a specific property and is highly beneficial for an array of engineering applications.

Many of the metastable polymorphs only existed in high temperature/pressure conditions in bulk form or were completely unknown. Nanoscale engineering has opened the pathways for newer polymorphs, which were recently unknown.

The polymorphism behavior for nanocrystalline materials has been associated with the critical size of the grains. Traditional methods either offer less control over engineering the particle size or are not commercially viable. The drawbacks of traditional processes is overcome by flame spray pyrolysis, which offers homogenous size distribution (with control over particle sizes) and is an industrial process. Lot of research has been conducted on particle formation through fsp and many metastable materials have been reported. Literature review has indicated a close relation between the parameters, particle size and polymorph formation. However, no evaluation has been done, on formation of polymorphs that relate the effect of processing parameters to polymorphic states in materials.

Hence, this thesis aims at studying formation of polymorphs via fsp process. The effects of precursor concentration, precursor type, and precursor solvent are taken into consideration and their effect on polymorphic behavior is reported. Alternatively, this thesis also exploits formation of self-supported nanostructures through electrospinning process.

References

1. Hui, B. and J. Li, *Low-temperature synthesis of hierarchical flower-like hexagonal molybdenum trioxide films on wood surfaces and their light-driven molecular responses.* Journal of Materials Science, 2016. **51**(24): p. 10926-10934.
2. Oswald, H.R., J.R. Gunter, and E. Dubler, *Topotactic decomposition and crystal structure of white molybdenum trioxide-monohydrate: Prediction of structure by topotaxy.* Journal of Solid State Chemistry, 1975. **13**(4): p. 330-338.
3. McCarron Iii, E.M., *β-MoO<inf>3</inf>: A metastable analogue of WO<inf>3</inf>*. Journal of the Chemical Society, Chemical Communications, 1986(4): p. 336-338.
4. Salje, E., R. Gehlig, and K. Viswanathan, *Structural phase transition in mixed crystals WxMO1−xO3.* Journal of Solid State Chemistry, 1978. **25**(3): p. 239-250.
5. Lou, X.W. and H.C. Zeng, *Hydrothermal synthesis of alpha-MoO3 nanorods via acidification of ammonium heptamolybdate tetrahydrate.* Chemistry of Materials, 2002. **14**(11): p. 4781-4789.
6. Kalantar-zadeh, K., et al., *Synthesis of nanometre-thick MoO3 sheets.* Nanoscale, 2010. **2**(3): p. 429-433.
7. Chen, D.L., et al., *Single-crystalline MoO3 nanoplates: topochemical synthesis and enhanced ethanol-sensing performance.* Journal of Materials Chemistry, 2011. **21**(25): p. 9332-9342.
8. Gouma, P., K. Kalyanasundaram, and A. Bishop, *Electrospun single-crystal MoO3 nanowires for biochemistry sensing probes.* Journal of Materials Research, 2006. **21**(11): p. 2904-2910.
9. Gouma, P.I., A.S. Haynes, and K. Kalyanasundaram, *Electrospun single crystal MoO3 nanowires for bio-chem sensing probes*. 2011, Google Patents.
10. Shimizu, R., et al., *Low-temperature deposition of meta-stable β-MoO3(011) epitaxial thin films using step-and-terrace substrates.* Thin Solid Films, 2015. **595, Part A**: p. 153-156.

11. Davide, M., et al., *Monoclinic β-MoO 3 nanosheets produced by atmospheric microplasma: application to lithium-ion batteries.* Nanotechnology, 2008. **19**(49): p. 495302.
12. Juárez Ramírez, I. and A. Martínez-de la Cruz, *Synthesis of β-MoO3 by vacuum drying and its structural and electrochemical characterisation.* Materials Letters, 2003. **57**(5–6): p. 1034-1039.
13. Prasad, A.K. and P.I. Gouma, *MoO3 and WO3 based thin film conductimetric sensors for automotive applications.* Journal of Materials Science, 2003. **38**(21): p. 4347-4352.
14. Prasad, A.K., D.J. Kubinski, and P.I. Gouma, *Comparison of sol–gel and ion beam deposited MoO3 thin film gas sensors for selective ammonia detection.* Sensors and Actuators B: Chemical, 2003. **93**(1–3): p. 25-30.
15. Kumar, V., X. Wang, and P.S. Lee, *Synthesis of pyramidal and prismatic hexagonal MoO3 nanorods using thiourea.* CrystEngComm, 2013. **15**(38): p. 7663-7669.
16. Zhou, J., et al., *Synthesis of hexagonal MoO3 nanorods and a study of their electrochemical performance as anode materials for lithium-ion batteries.* Journal of Materials Chemistry A, 2015. **3**(14): p. 7463-7468.
17. Song, J., et al., *Preparation of hexagonal-MoO3 and electrochemical properties of lithium intercalation into the oxide.* Materials Research Bulletin, 2005. **40**(10): p. 1751-1756.
18. Zheng, L., et al., *Novel Metastable Hexagonal MoO3 Nanobelts: Synthesis, Photochromic, and Electrochromic Properties.* Chemistry of Materials, 2009. **21**(23): p. 5681-5690.
19. Wu, Z., et al., *Ultrasonic-assisted preparation of metastable hexagonal MoO3 nanorods and their transformation to microbelts.* Ultrasonics Sonochemistry, 2011. **18**(1): p. 288-292.
20. Sawada, S., *Microscopic and X-Ray Studies on Tungsten Oxide (WO3).* Journal of the Physical Society of Japan, 1956. **11**(12): p. 1246-1252.
21. Gouma, P.I. and K. Kalyanasundaram, *Novel synthesis of hexagonal WO3 nanostructures.* Journal of Materials Science, 2015. **50**(9): p. 3517-3522.
22. Detraux, F., P. Ghosez, and X. Gonze, *Anomalously large Born effective charges in cubic WO_3.* PHYSICAL REVIEW B, 1997. **56**(3).
23. Pokhrel, S., et al., *Growth of Ultrafine Single Crystalline WO3 Nanoparticles Using Flame Spray Pyrolysis.* Crystal Growth & Design, 2010. **10**(2): p. 632-639.

24. Hernandez-Uresti, D.B., et al., *Characterization and photocatalytic properties of hexagonal and monoclinic WO3 prepared via microwave-assisted hydrothermal synthesis.* Ceramics International, 2014. **40**(3): p. 4767-4775.
25. Sood, S., K. Kisslinger, and P. Gouma, *Nanowire Growth by an Electron-Beam-Induced Massive Phase Transformation.* Journal of the American Ceramic Society, 2014. **97**(12): p. 3733-3736.
26. Gouma, P.I. and K. Kalyanasundaram, *A selective nanosensing probe for nitric oxide.* Applied Physics Letters, 2008. **93**(24): p. 244102.
27. Kai, H., et al., *Controllable synthesis of hexagonal WO 3 nanostructures and their application in lithium batteries.* Journal of Physics D: Applied Physics, 2008. **41**(15): p. 155417.
28. Shang, F.L., H.T. Yang, and L. Gao, *Preparation and Photocatalytic Property of Cubic WO3.* Advanced Materials Research, 2015. **1081**: p. 304-307.
29. Fumiaki, M., et al., *WO 3 Thin Films Prepared by Pulsed Laser Deposition.* Japanese Journal of Applied Physics, 2002. **41**(8R): p. 5372.
30. Raman, G. and G. Aharon, *Synthesis of WO 3 nanoparticles using a biopolymer as a template for electrocatalytic hydrogen evolution.* Nanotechnology, 2008. **19**(2): p. 025702.
31. Deliang, C., et al., *The enhanced alcohol-sensing response of ultrathin WO 3 nanoplates.* Nanotechnology, 2010. **21**(3): p. 035501.
32. Wang, L., et al., *Ferroelectric WO3 Nanoparticles for Acetone Selective Detection.* Chemistry of Materials, 2008. **20**(15): p. 4794-4796.
33. Vemuri, R.S., et al., *Effect of Structure and Size on the Electrical Properties of Nanocrystalline WO3 Films.* ACS Applied Materials & Interfaces, 2010. **2**(9): p. 2623-2628.
34. Dupre, N., et al., *Phase transition induced by lithium insertion in αI- and αII-VOPO4*. Journal of Solid State Chemistry, 2004. **177**: p. 2896-2902.
35. Ling, C., R. Zhang, and F. Mizuno, *Phase stability and its impact on the electrochemical performance of VOPO4 and LiVOPO4.* Journal of Materials Chemistry A, 2014. **2**(31): p. 12330-12339.
36. Erdem, I., H.H. Kart, and T. Cagin, *High pressure phase transitions in SnO2 polymorphs by first-principles calculations.* Journal of Alloys and Compounds, 2014. **587**: p. 638-645.

37. Gateshki, M., et al., *Titania Polymorphs by Soft Chemistry: Is There a Common Structural Pattern?* Chemistry of Materials, 2007. **19**: p. 2512-2518.
38. Kumar, S.G. and K.S.R.K. Rao, *Polymorphic phase transition among the titania crystal structures using a solution-based approach: from precursor chemistry to nucleation process.* Nanoscale, 2014. **6**.
39. Wu, C., et al., *New Vanadium Oxide Nanostructures: Controlled Synthesis and Their Smart Electrical Switching Properties.* Advanced Materials, 2010. **22**(17): p. 1972-1976.
40. Filonenko, V.P., et al., *Structure of a high-pressure phase of vanadium pentoxide, β-V 2O5.* Acta Crystallographica Section B: Structural Science, 2004. **60**(4): p. 375-381.
41. Ganduglia-Pirovano, M.V. and J. Sauer, *Stability of reduced ${\mathrm{V}}_{2}{\mathrm{O}}_{5}(001)$ surfaces.* Physical Review B, 2004. **70**(4): p. 045422.
42. Parija, A., et al., *Topochemically De-Intercalated Phases of V2O5 as Cathode Materials for Multivalent Intercalation Batteries: A First-Principles Evaluation.* Chemistry of Materials, 2016. **28**(16): p. 5611-5620.
43. Kijima, N., et al., *Crystal structure of an open-tunnel oxide α-MnO2 analyzed by Rietveld refinements and MEM-based pattern fitting.* Journal of Solid State Chemistry, 2004. **177**(4–5): p. 1258-1267.
44. Tompsett, D.A., S.C. Parker, and M.S. Islam, *Rutile (β-)MnO2 Surfaces and Vacancy Formation for High Electrochemical and Catalytic Performance.* Journal of the American Chemical Society, 2014. **136**(4): p. 1418-1426.
45. Caltagirone, S. and J. Massingill, *Developing γ-MnO2 Models for XRD Analysis.* ECS Transactions, 2008. **11**(32): p. 29-35.
46. Thai, T.M.N., S.R. Kim, and H.J. Kim, *Synthesis of Fe2O3 Polymorph Thin Films via a Pulsed Laser Deposition Technique.* New Physics: Sae Mulli,, 2014. **64**(3): p. 252-255.
47. Wróbel, J. and J. Piechota, *Structural properties of ZnO polymorphs* physica status solidi (b), 2007. **244**(5): p. 1538-1543.
48. Gouma, P.-I., *Nanomaterials for Chemical Sensors and Biotechnology*. 2009.
49. Gouma, P.I., *Nanostructured Polymorphic Oxides for Advanced Chemosensors.* Reviews on advanced materials science, 2003. **5**(2).

50. Kim, W.-S., H.-C. Kim, and S.-H. Hong, *Gas sensing properties of MoO3 nanoparticles synthesized by solvothermal method*. Journal of Nanoparticle Research, 2010. **12**(5): p. 1889-1896.
51. Prasad, A.K., *Study of gas specificity in MoO3/WO3 thin film sensors and their arrays*, in *Materials Science & Engineering*. 2005, Stony Brook University: UMI.
52. Gouma, P.I. and L. Wang, *Flame Spray Synthesis of WO3 for NO Breath Monitors.* Journal of materials sciences & engineering, 2015. **4**(3).
53. Balázsi, C., et al., *Nanosize hexagonal tungsten oxide for gas sensing applications.* Journal of the European Ceramic Society, 2008. **28**(5): p. 913-917.
54. Wang, L., et al., *Synthesis and Sensing Properties to NH3 of Hexagonal WO3 Metastable Nanopowders.* Materials and Manufacturing Processes, 2007. **22**(6): p. 773-776.
55. Zheng, Z.Q., L.F. Zhu, and B. Wang, *In2O3 Nanotower Hydrogen Gas Sensors Based on Both Schottky Junction and Thermoelectronic Emission.* Nanoscale Research Letters, 2015. **10**(1): p. 293.
56. Ahmad, M., et al. *Non-aqueous synthesis of In2O3 nanoparticles and its NO2 gas sensing properties*. in *14th International Meeting on Chemical Sensors - IMCS 2012*. 2012. Nuremberg, Germany: AMA science.
57. Fujishima, A. and K. Honda, *Electrochemical Photolysis of Water at a Semiconductor Electrode.* Nature, 1972. **238**(5358): p. 37-38.
58. Linsebigler, A.L., G. Lu, and J.T. Yates, *Photocatalysis on TiO2 Surfaces: Principles, Mechanisms, and Selected Results.* Chemical Reviews, 1995. **95**(3): p. 735-758.
59. Paz, Y. and A. Heller, *Photo-oxidatively self-cleaning transparent titanium dioxide films on soda lime glass: The deleterious effect of sodium contamination and its prevention.* Journal of Materials Research, 1997. **12**(10): p. 2759-2766.
60. Topcu, S., G. Jodhani, and P. Gouma, *Optimized Nanostructured TiO2 Photocatalysts.* Frontiers in Materials, 2016. **3**(35).
61. Zhang, Z., et al., *Role of Particle Size in Nanocrystalline TiO2-Based Photocatalysts.* The Journal of Physical Chemistry B, 1998. **102**(52): p. 10871-10878.
62. Poizot, P., et al., *Nano-sized transition-metal oxides as negative-electrode materials for lithium-ion batteries.* Nature, 2000. **407**(6803): p. 496-499.

63. Bahn, C.S., et al., *Lithium Ion Diffusion Measurements in High Quality LiCoO2 thin Film Battery Cathodes*. MRS Proceedings, 1999. **575**.
64. Arai, H. and Y. Sakurai, *Lithium Nickelate with Cadmium Iodide Structure*. MRS Proceedings, 1999. **575**.
65. Singh, D., et al., *Pulsed laser deposition and characterization of LiMn2O4 thin Films for applications in Li Ion rechargeable battery systems*. MRS Proceedings, 1999. **575**.
66. M. Y. Saïdi, J.B., H. Huang, J. L. Swoyer and G. Adamson, *Electrochemical Properties of Lithium Vanadium Phosphate as a Cathode Material for Lithium-Ion Batteries*. Electrochemical and Solid-State Letters, 2002. **5**(7).
67. Andre, D., et al., *Future generations of cathode materials: an automotive industry perspective*. Journal of Materials Chemistry A, 2015. **3**(13): p. 6709-6732.
68. Gaubicher, J., et al., *Rhombohedral Form of Li3V2(PO4)3 as a Cathode in Li-Ion Batteries*. Chemistry of Materials, 2000. **12**(11): p. 3240-3242.
69. Sood, S. and P. Gouma, *Polymorphic Phase Transitions in Nanocrystalline Binary Metal Oxides*. Journal of the American Ceramic Society, 2013. **96**(2): p. 351-354.
70. Wang, C.X. and G.W. Yang, *Thermodynamics of metastable phase nucleation at the nanoscale*. Materials Science and Engineering: R: Reports, 2005. **49**(6): p. 157-202.
71. Gilgien, P., A. Zryd, and W. Kurz, *Metastable phase diagrams and rapid solidification processing*. ISIJ International, 1995. **35**(6): p. 566-573.
72. Shu-qing, Y., *Influence of Rapid Solidification on the Microstructural Development of Zinc–Aluminum Alloys*. Metallography, Microstructure, and Analysis, 2014. **3**(2): p. 147-151.
73. Teoh, W.Y., R. Amal, and L. Mädler, *Flame spray pyrolysis: An enabling technology for nanoparticles design and fabrication*. Nanoscale, 2010. **2**: p. 1324-1347.
74. Pratsinis, S.E., *Flame aerosol synthesis of ceramic powders*. Progress in Energy and Combustion Science, 1998. **24**(3): p. 197-219.
75. Laine and R.M.e. al. 2005: United States.
76. Helble, J., *Combustion aerosol synthesis of nanoscale ceramic powders*. JOURNAL OF AEROSOL SCIENCE, 1998: p. 721-736.
77. Strobel, R., A. Alfons, and S.E. Pratsinis, *Aerosol flame synthesis of catalysts*. Advanced Powder Technology, 2006. **17**(5): p. 457-480.

78. Purwanto, A., W.-N. Wang, and K. Okuyama, *Flame Spray Pyrolysis*, in *Handbook of Atomization and Sprays: Theory and Applications*, N. Ashgriz, Editor. 2011, Springer US: Boston, MA. p. 869-879.
79. Jang, Y.J., C. Simer, and T. Ohm, *Comparison of zinc oxide nanoparticles and its nano-crystalline particles on the photocatalytic degradation of methylene blue.* Materials Research Bulletin, 2006. **41**(1): p. 67-77.
80. Mädler, L., et al., *Controlled synthesis of nanostructured particles by flame spray pyrolysis.* Journal of Aerosol Science, 2002. **33**(2): p. 369-389.
81. Jung, D.S., et al., *Nano-sized barium titanate powders with tetragonal crystal structure prepared by flame spray pyrolysis.* Journal of the European Ceramic Society, 2008. **28**(1): p. 109-115.
82. Purwanto, A., et al., *Formation of BaTiO3 nanoparticles from an aqueous precursor by flame-assisted spray pyrolysis.* Journal of the European Ceramic Society, 2007. **27**(16): p. 4489-4497.

Chapter 2: Materials synthesis and characterization methods

2.1 Materials Synthesis

2.1.1 Sol Gel Synthesis:

A sol-gel is a colloidal suspension of solid particles in liquid. Sol-gel processing is a soft chemistry route used to prepare a sol, ensure its gelation, and removal of solvent [1]. The gel thus obtained consists of a continuous solid phase in a continuous liquid phase. The sol can be produced from either an organic or inorganic precursor. A precursor is the initial compound required to process the gel. The precursor readily reacts with water to give metal-based sol-gels. Metal alkoxides are typically used as a precursor for this purpose. Alkoxides have an organic ligand attached to the metal atom. The organic ligand reacts with water and giver metal hydroxide and alcohol. The equation for this is given by:

$M\text{-}(O\text{-}R)_x + xH_2O \rightarrow M\text{-}(O\text{-}H)_x + xR\text{-}O\text{-}H$

Where R is the alkyl group attached to the precursor.

After the formation of the sol-gel, there are number of ways in which metal oxides can be derived from them in the desired form. For example, thin films can be obtained by spin coating and followed by calcination of the material in order to achieve a desired phase change.

2.1.2 Electrospinning: Principles and Operation

Electrospinning was first patented by Formhals in 1934 for textile weaving [2]. A typical electrospinning setup consists of a syringe pump, a syringe with needle, a grounded collector and a high voltage power supply. The solution that is to be spun is filled in the syringe; the syringe is then loaded on the syringe pump which pumps the solution at a very low rate. The needle of the syringe is connected to the high voltage power supply, either a positive or a negative potential can be used. The collector is grounded, due to high potential difference developed in between the needle and the collector the fibers get deposited on the collector. Figure 2.1 below shows a traditional setup for electrospinning.

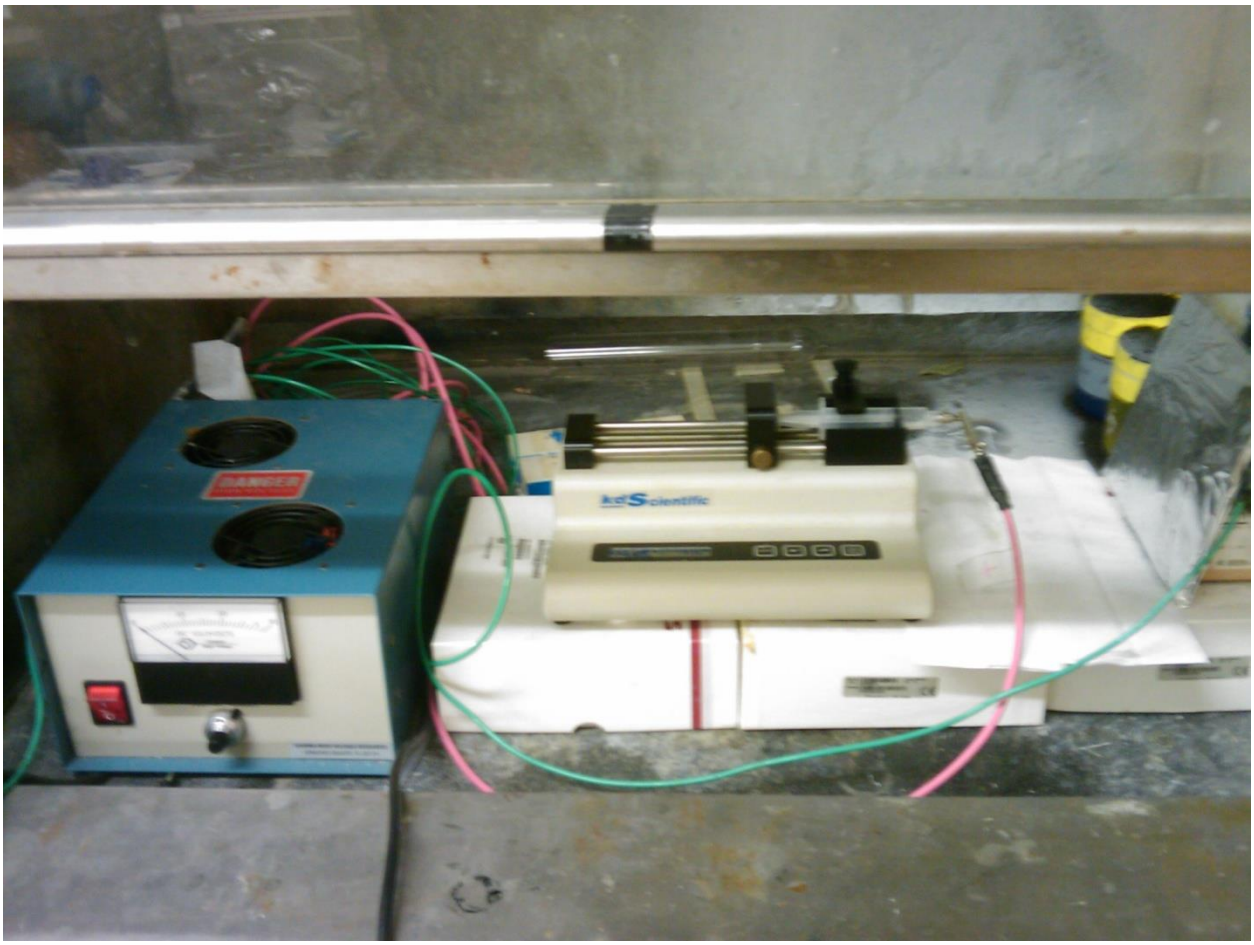

Figure 2-3: Electrospinning setup

The setup for electrospinning is easy to put together ("poor man's way to nanotechnology" as the process is known), but the science involved in making of the nanofibers is relatively complex. There are several parameters that affect the morphology of the spun nanofibers. These include: potential applied across the needle, viscosity of the solution, concentration of the solution, distance between the needle and the collector, conductivity of the solution, feed rate, internal diameter of the needle etc. Figure 2.2 below shows the different parameters that affect fiber diameter via electrospinning.

With regards to process parameters, surface tension plays an important role. The charge on the solution should be high enough to overcome the surface tension. A high surface tension may lead to breakup of the solution into droplets. For a pure liquid, a droplet will acquire a shape that has lowest surface area to volume ratio. In case of solvent mixtures the shape changes-due to the difference in viscosity of the mixture and the composition at surface is different than the bulk [3].

A high surface tension could also lead to formation of beads in the fiber trying to stabilize the drops by forming a spherical structure [4]. When the electrostatic force is large enough to counteract the surface tension, the solution is extended. At a critical point when the electrostatic forces overcome those of surface tension [5] a stream of liquid erupts from the surface. The extended solution is in the form of a cone, which is known as Taylor cone.

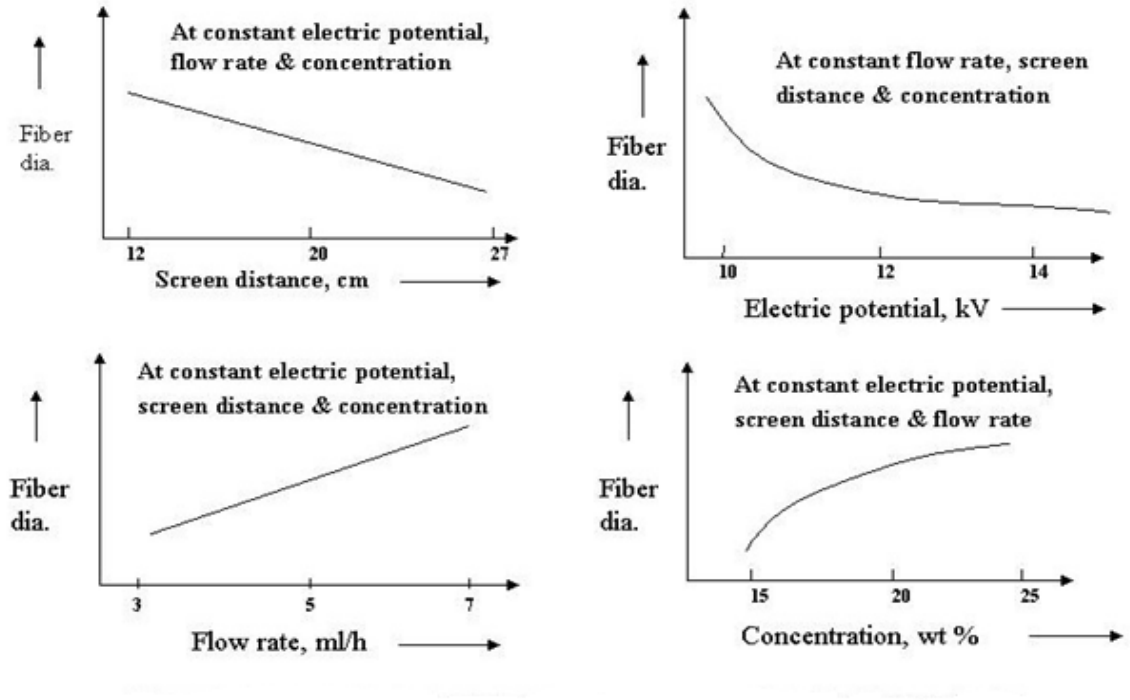

Figure 2-4: Process maps for electrospinning [5]

Precursor parameters include the viscosity of the solution for electrospinning to occur, jet stabilization is required. To achieve this; a sufficiently high extensional viscosity is required [6].

2.1.3 Flame Spray Pyrolysis

Flame spray pyrolysis (FSP) is a technique that is mainly applied for synthesis of nanoparticles in the form of nanospheres. This process, when used for synthesizing metal oxides requires a precursor to be fed in form of vapor[7] or liquid[8]. However, the vapor fed FSP, also known as vapor assisted flame spray(VASP), has its limitations as it has only be used for synthesizing oxides

of SiO_2, Al_2O_3, TiO_2 and ZrO_2[9]. To fabricate more complex metal oxides a liquid fed FSP was developed by R.M Laine at University of Michigan, Ann Arbor[10]. The liquid fed FSP was able to overcome the drawback of FASP by fabricating more complex metal oxide particles.

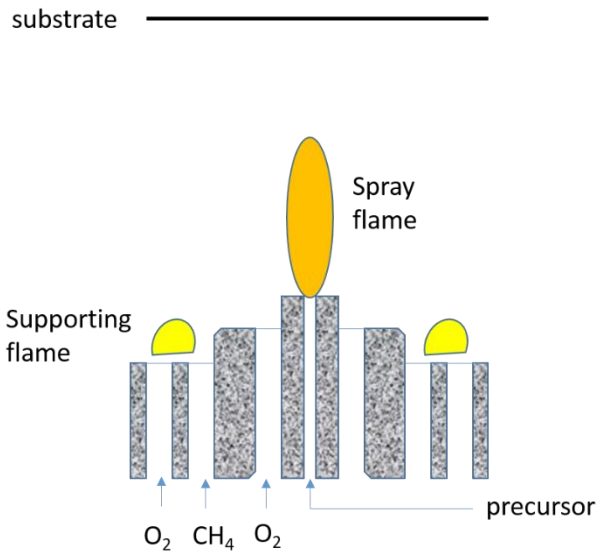

Figure 2-5 Schematic diagram of Flame Spray pyrolysis (FSP) setup[11]

The process uses a metal oxide precursor in the form of liquid; its composition is generally in the form of metal chlorides, metal nitrates or metal acetates dissolved in aqueous or alcohol based solutions[12]. However, during the selection of precursor solute the combustion enthalpies should be kept in mind. It has been found that the precursors with low enthalpies coupled with high melting/decomposition points yielded in non-homogenous metal oxide particles[13]. Figure 2.3 above shows the schematic diagram for FSP flame. The precursor is fed to the flame at a constant rate. The flame is generated via a combustible gas, mainly methane. The combustible gas is used to create an elevated temperature, once the solution enters the system the flame is self-sustainable as the solution fed is combustible. Once in contact with the flame the solution vaporizes. The vapor then reacts in the chamber with oxygen, which is used as a sheath gas, forming intermediate and product molecules. The formed molecules quickly grow into nanosize particles by coagulation and/or surface reactions, figure 2.4 shows the mechanism for formation of particles. Upon leaving the high temperature zone the particles slowly cool down to a low temperature for particle

collection. The particles are then collected on a filter and the gases formed as a result of combustion are vented out.

Due to the rapid cooling of the vapors to solid, the particles formed are in the form of spheres. The size of the particles varies from 50-200 nm in diameter. The particles formed are porous, which makes them an excellent choice as materials for batteries, fuel cells, catalysts.

Various metal oxide nanoparticles such as WO_3 [14], SnO_2 [15], ZnO [16], ZrO_2 [17], BiO_3 [18], CeO_2 [19], Y_2O_3 [20] etc have been successfully made using FSP process. Apart from single metal oxides, mixed metal oxides such as $LiCoO_2$ [21], LiV_3O_8 [22], (CeOx)(x)(Al2O3)(1-x) [23], $LiMn_2O_4$ [24] etc have also been synthesized using FSP. The advantage of using FSP over other methods is that such materials can be fabricated in a single step with ease. Other than the ease of processing the materials produced via FSP were also found better compared to the same materials processed through other techniques.

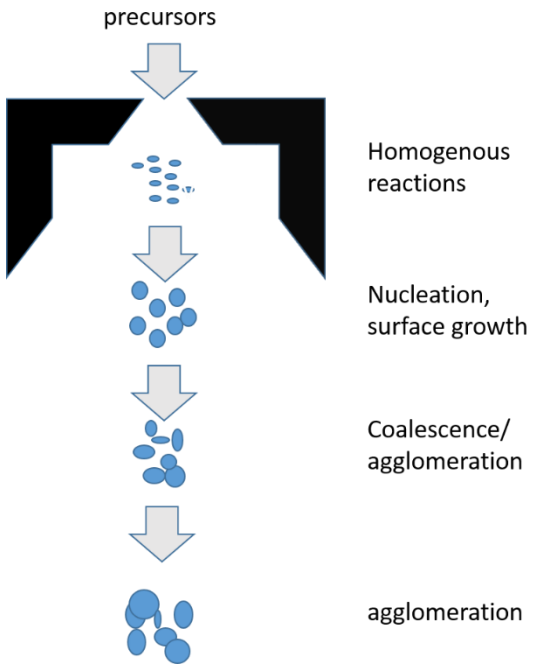

Figure 2-6: Principles of formation of particles in FSP [25]

Particles produced through FSP are in the form of nanospheres. Core shell nanospheres [21, 23] and hollow nanospheres[26] have also been reported. The formation of hollow, core shell or solid oxide is dependent on the precursor/solvent composition used. Formation of core shell (CeOx)(x)(Al2O3)(1-x) [23] occurred when a higher concentration of precursor was used in the

solvent. Lower concentration of precursor yielded Ce^{3+} ions in δ-Al_2O_3 or $CeAl_{11}O_8$. Similar results were found for $(ZrO_2)_x(Al_2O_3)_{1-x}$ [27]. Formation of hollow particles have been reported for low combustion enthalpy densities and when the solvent boiling point is less than the melting/decomposition point of the precursor. FSP has also been used to synthesize nanorods for ZnO [28], the nanorods were formed when ZnO was doped with In and Sn dopants. Li that had a lower valency and same ionic radius as Zn was also used as a dopant and had no effect on the shape of nanoparticles formed. Hence, the formation of nanorods were attributed to the higher valency state and coordination of the dopants to Zn.

FSP has also yielded in the formation of metastable phases at room temperature. The formation of these phases are due to the rapid quenching of particles. For e.g. the epsilon phase of WO_3 that was found to exist at below -15°C was stabilized at room temperature using FSP.

Figure 2-7: NPS 10 desktop FSP used in this work (P. Gouma's lab SBU)

The flame spray pyrolysis was carried in flame spray pyrolysis equipment (NPS10) purchased from Tethis (Italy) (Figure 2.5). The equipment is a bench top device and is to be

installed in a vented fume hood so the combustion gases do not pollute the lab environment. A custom-made fume hood was ordered from Hemco Corporation that fits the requirements of the bench top device. A vacuum pump is installed with the equipment to vent out the gases. A computer is connected to the FSP equipment that controls the operating parameters.

2.2 Materials characterization techniques

2.2.1 X-ray Diffraction (XRD)

XRD is a method used to identify crystalline phases in materials. It is a very useful and versatile non-destructive technique for characterization of samples. XRD is based on constructive interference of monochromatic X-rays, the X-rays are generated by a cathode ray tube. The interaction of the generated rays with the samples produces interference when conditions are satisfied for Bragg's Law:

$$n\lambda = 2d \sin \Theta \text{ [29]}$$

Where λ is the wavelength of X-Ray and Θ is the angle between the incident beam and the scattering planes.

A diffraction pattern is generated when the X-ray hits and interacts with the specimen. The X-rays diffracted are detected, processed, and counted. The intensity of diffracted X-rays at the detector at each angle makes up for a diffraction pattern. Each crystalline phase produces its own pattern, hence, the patterns are also considered as fingerprints for each phase.

Apart from phase identification, XRD peaks can also be used to compute the size of crystallinity by using Scherrer equation:

$$\tau = (\lambda\kappa)/(\beta \cos \Theta) \text{ [29]}$$

Where κ is the shape factor, λ is the wavelength of X-Ray, β is the line broadening at half the maximum intensity and Θ is the Bragg angle. A standard value for κ is usually 0.9, but can vary with the shape of crystallite.

2.2.2 Scanning Electron Microscopy (SEM)

Scanning Electron Microscopy (SEM) is an imaging technique to analyze the surface characteristics of materials with a resolution of 2nm. Discuss the specific SEMs you used in your research at SBU and BNLA focused high-energy electron beam is used for imaging the samples,

the beam interacts with the surface atoms causing energy exchange between the electron beam and the sample which results in reflecting the high energy electrons by elastic scattering. Secondary electrons are also generated due to inelastic scattering. The electrons are collected by detectors to produce an image of the surface.

Scanning Electron Microscopy (SEM) was carried out on a LEO-1550 Schottkey Field Emission Gun SEM to obtain the morphology of the particles. The powder samples were mounted on an aluminum plate with the help of carbon tape. The samples were sputter coated with gold to ensure conductivity. SEM images were obtained with back scattered signal of EHT 20 kV and 7~10 mm working distance, secondary electron detector was also used for surface analysis with EHT 5 kV and 7~10mm working distance.

2.2.3 Transmission Electron Microscope (TEM)

Transmission Electron Microscope (TEM) is an important instrument to analyze the structure of the nanomaterials. It is an imaging technique, which uses a high energy electron beam for imaging of samples. Unlike SEM where the beam is reflected and detected from the surface; the electron beam in TEM is transmitted through a sample producing high-resolution images and electron diffraction patterns.

The beam interacts with the components of the sample and the transmitted electrons hit a fluorescent screen. TEM images are formed with high resolutions and provide information on the internal composition of the sample. The imaging resolution of a TEM is higher compared to that of a SEM. Characteristic details such as particle size, shape, crystallization, stress, and morphology can be determined by TEM.

Energy dispersive X-ray analysis (EDX) is a technique used to identify the elemental composition of materials. When the electron beam hits the sample, X-rays are generated which have characteristic energies for each element. This provides a qualitative analysis of the elements present and with further analysis, a quantitative composition can be determined. Selected area electron diffraction (SAED) uses diffracted electrons to elucidate crystallographic information from selected regions of the sample. The spacings and the orientation of the diffraction spots can be interpreted in terms of planar spacings and orientations in the sample.

Transmission Electron Microscope (TEM) was carried on JEOL-1400 TEM. The nanoparticles were drop coated on a copper grid mesh (LaB6 cathode electron source) to determine the phase and observe the grains of nanoparticles.

2.2.4 Fourier Transform Infrared Spectroscopy

Fourier transform infrared spectroscopy (FTIR) is a technique used to obtain an infrared spectrum of absorption/emission of a substance. The substance can either be in the form of solid, liquid or gas. The concept of FTIR relies on shining a beam containing many frequencies at once. It then measures the amount of beam absorbed by the sample. The process is repeated multiple times; a computer is used to collect the data points, which analyzes and infers the absorption at each wavelength.

A Thermo Scientific Nicolet 6700 FTIR with ZnSe crystal ATR detector was used for the experiments.

2.2.5 UV-Vis Spectroscopy

UV-VIS Spectroscopy is used to determine the optical properties of photocatalyst such as light absorbance. Absorbance is a measurement of the attenuation of the photons that pass through a sample or after reflection from a sample surface to produce excited charge carriers. Absorption of visible or ultraviolet radiation corresponds to the excitation of outer electrons from their ground state to an excited state. The absorbance (A) of a sample is, according the Lambert Beer's law which states that $A = \varepsilon cl$, proportional to the concentration (c), path length (l) and extinction coefficient (ε). UV-Vis spectroscopy is an efficient method to characterize quantitative measurements, absorption, transmission, and reflectivity of a variety of materials. Bandgap can be estimated from information extracted from UV-Vis spectrum.

UV-Vis Spectroscopy experiment was carried on Lambda 950 UV-VIS spectrophotometer.

2.2.6 Thermal Analysis

Thermal analysis generally covers three different experimental techniques: Thermo Gravimetric Analysis (TGA), Differential Thermal Analysis (DTA), and Differential Scanning Calorimetry (DSC).

The basic principle in TGA is to measure the mass of a sample as a function of temperature. The method for example can be used to determine water of crystallization, study oxidation and reduction. Many thermal (enthalpy) changes in materials (e.g. phase transitions) do not involve a change of mass. In DTA one instead measures the temperature difference between an inert reference and the sample as a function of temperature. When the sample undergoes a physical or chemical change the temperature increase differs between the inert reference and the sample, and a peak or a dip is detected in the DTA signal. The technique is routinely applied in a wide range of studies such as identification, quantitative composition analysis, phase diagrams, hydration-dehydration, thermal stability, polymerization, purity, and reactivity.

TGA and DTA techniques are used in this project to study the phase stability of produced materials at elevated temperatures. They were accomplished on a Perkin Elmer TGA/DTA thermal analyzer under oxygen. The sample was heated to 550°C at a rate of 10°C/min. Aluminum was taken as the reference material.

References

1. A. K. Prasad, "Study of gas specificity in MoO3/WO3 thin film sensors and their arrays," in *Materials Science and Engineering*, Ed., SUNY Stony Brook, 2005.

2. F. Anton, "Process and apparatus for preparing artificial threads," Ed., Google Patents, 1934.

3. R. Seeram, F. Kazutoshi, T. Wee-Eong, L. Teik-Cheng and M. Zuwei, *An Introduction to Electrospinning and Nanofibers*, World Scientific, 2005.

4. H. Fong, I. Chun and D. H. Reneker, "Beaded nanofibers formed during electrospinning," *Polymer*, vol. 40, no. 16, pp. 4585-4592, 1999.

5. G. Wilkes, "Electrospinning," Ed., http://www.che.vt.edu/Faculty/Wilkes/GLW/electrospinning/electrspinning.html.

6. O. Regev, S. Vandebril, E. Zussman and C. Clasen, "The role of interfacial viscoelasticity in the stabilization of an electrospun jet," *Polymer*, vol. 51, no. 12, pp. 2611-2620, 2010.

7. J. e. a. Liu, "Flame Synthesis of Ball-in-Shell Structured TiO2 Nanospheres," *INDUSTRIAL & ENGINEERING CHEMISTRY RESEARCH*, pp. 735-739, 2009.

8. R. L. Laine, RM) et al., "Liquid-feed flame spray pyrolysis of nanopowders in the alumina-titania system," *CHEMISTRY OF MATERIALS*, pp. 2336-2343, 2004.

9. P. SE, "Flame aerosol synthesis of ceramic powders," *PROGRESS IN ENERGY AND COMBUSTION SCIENCE*, pp. 197-219, 1998.

10. Laine and R. M. e. al., Ed., United States, 2005.

11. J. Lee, "Synthesis and Characterization of Nanostructured Metal Oxide for Water Remediation and Energy Applications," in *Materials Science and Engineering*, Ed., Stony Brook University, ProQuest LLC, 2013.

12. J. Helble, "Combustion aerosol synthesis of nanoscale ceramic powders," *JOURNAL OF AEROSOL SCIENCE*, pp. 721-736, 1998.

13. L. e. a. Madler, "Flame Spray Pyrolysis: An enabling technology for nanoparticles design and fabrication," *NANOSCALE*, pp. 1324-1347, 2010.

14. K. K. Akurati, A. Vital, J.-P. Dellemann, K. Michalow, T. Graule, D. Fetti and A. Baiker, "Flame-made WO3/TiO2 nanoparticles: Relation between surface acidity, structure and photocatalytic activity," *Applied Catalysis B-Environmental*, vol. 79, no. 1-2, pp. 53-62, 2008.

15. T. Sahm, L. Madler, A. Gurlo, N. Barsan, S. E. Pratsinis and U. Weimar, "Flame spray synthesis of tin dioxide nanoparticles for gas sensing," *Sensors and Actuators B-Chemical*, vol. 98, no. 2-3, pp. 148-153, 2004.

16. T. Tani, L. Madler and S. E. Pratsinis, "Homogeneous ZnO nanoparticles by flame spray pyrolysis," *Journal of Nanoparticle Research*, vol. 4, no. 4, pp. 337-343, 2002.

17. A. I. Y. Tok, F. Y. C. Boey, S. W. Du and B. Wong, "Flame spray synthesis of ZrO2 nano-particles using liquid precursors," *Materials Science and Engineering B-Solid State Materials for Advanced Technology*, vol. 130, no. 1-3, pp. 114-119, 2006.

18. L. Madler and S. E. Pratsinis, "Bismuth oxide nanoparticles by flame spray pyrolysis," *Journal of the American Ceramic Society*, vol. 85, no. 7, pp. 1713-1718, 2002.

19. L. Madler, W. J. Stark and S. E. Pratsinis, "Flame-made ceria nanoparticles," *Journal of Materials Research*, vol. 17, no. 6, pp. 1356-1362, 2002.

20. B. Guo, A. Harvey, S. H. Risbud and I. M. Kennedy, "The formation of cubic and monoclinic Y2O3 nanoparticles in a gas-phase flame process," *Philosophical Magazine Letters*, vol. 86, no. 7, pp. 457-467, 2006.

21. S. H. Choi, J.-H. Lee and Y. Chan Kang, "One-pot rapid synthesis of core-shell structured NiO@TiO2 nanopowders and their excellent electrochemical properties as anode materials for lithium ion batteries," *Nanoscale*, vol. 5, no. 24, pp. 12645-12650, 2013.

22. T. J. Patey, S. H. Ng, R. Buechel, N. Tran, F. Krumeich, J. Wang, H. K. Liu and P. Novak, "Electrochemistry of LiV3O8 nanoparticles made by flame spray pyrolysis," *Electrochemical and Solid State Letters*, vol. 11, no. 4, pp. A46-A50, 2008.

23. M. Kim, T. R. Hinklin and R. M. Laine, "Core-shell Nanostructured Nanopowders along (CeOx)(x)(Al2O3)(1-x) Tie-Line by Liquid-Feed Flame Spray Pyrolysis (LF-FSP)," *Chemistry of Materials*, vol. 20, no. 16, pp. 5154-5162, 2008.

24. T. J. Patey, R. Buechel, M. Nakayama and P. Novak, "Electrochemistry of LiMn2O4 nanoparticles made by flame spray pyrolysis," *Physical Chemistry Chemical Physics*, vol. 11, no. 19, pp. 3756-3761, 2009.

25. P. Roth, "Particle Synthesis in Flames," in *Proceedings of the combustion Institute*, Ed., pp. 1773-1788, 2007.

26. S. E. P. R. Jossen, W. J. Stark, L. Mädler, "Criteria for Flame-Spray Synthesis of Hollow, Shell-Like, or Inhomogeneous Oxides," *Journal of the American Ceramic Society*, vol. 88, no. 6, pp. 1388–1393, 2005.

27. M. K. a. R. M. Laine, "Liquid-feed flame spray pyrolysis (LF-FSP) for combinatorial processing of nanooxide powders along the (ZrO2)1-x(Al2O3)x tie-line. Phase segregation and the formation of core-shell nanoparticles," *Journal of Ceramic Processing Research*, vol. 8, no. 2, pp. 129-136, 2007.

28. M. J. Height, L. Madler, S. E. Pratsinis and F. Krumeich, "Nanorods of ZnO made by flame spray pyrolysis," *Chemistry of Materials*, vol. 18, no. 2, pp. 572-578, 2006.

29. B. D. Cullity, *Elements of X-Ray Diffraction*, Prentice, Upper Saddle River, 3rd edition 2001.

Chapter 3: Flame Spray Synthesis and Ammonia sensing properties of pure α-MoO_3 nanosheets

3.1 Introduction

The orthorhombic phase of MoO_3, commonly known as α-MoO_3, has been used for variety of applications in gas sensing of ammonia[1, 2], Li-ion intercalation in batteries [3-5], pseudo-capacitors[6-8], and hydrogen absorption[9]. Recent studies have led to development of α-MoO_3-polymer composite electrodes with a greatly improved cycling behavior for use in aqueous lithium[10] and sodium[11] rechargeable batteries. The layered structure of the material consists of MoO_6 octahedra held together by Van der Waals forces. The layered structure and the ease of Mo(VI)/Mo(V) coupling makes MoO_3 of interest in electrochemical systems and displays[12] as the coupling generates holes and results in electrochromism.

α-MoO_3 was synthesized by our research group through various different routes (sol-gel process, sputtering, electron beam deposition, electrospinning etc.[2, 13, 14]). Also it was studied in diverse configurations (nanoparticles, nanowires[2, 13]). However, in order to be able to manufacture ammonia sensors based on nanostructured α-MoO_3 in large quantities, a scalable nano-manufacturing process needs to be used for the materials synthesis. Flame spray pyrolysis is such a process, and it is explored here for the synthesis of MoO_3. The methodology used to produce particles at a laboratory based FSP setup, can be transferred to a foundry for bulk synthesis of the material. Aeroxide P25 Titania, from Evonik industries, is example of commercial Titania nanopowder synthesized via flame aerosol technique. Apart from the commercial aspect, the advantage of flame spray synthesis lies in ease of fabrication, elimination for the use of expensive raw materials, uniform size distribution and high purity of product. Flame synthesized particles have small particle sizes and high surface area: volume ratios, which is desirable for gas sensing and electrochemical applications.

Earlier synthesis by other workers of MoO_3 via flame spray pyrolysis relied on TiO_2 doping to stabilize the α- phase[15]. However, doping agents tend to create long term stability issues in sensing materials[16] and thus pure α-MoO_3 is the desirable product of FSP processing.

In this study, pure α-MoO_3 particles were successfully synthesized through FSP using an aqueous precursor of ammonium molybdate tetrahydrate. The particles were analyzed as ammonia sensors and the results were compared with the literature.

3.2 Experimental Method

MoO_3 particles were synthesized via Flame Spray Pyrolysis (Tethis nps10) technique. Ammonium molybdate tetrahydrate was selected as a precursor of its low melting point (90ºC) and non-volatile nature. The precursors were dissolved in water to obtain a homogenous solution. The addition of dimethylformamide to the solution was to obtain a self-sustainable process. Two solutions were prepared with different concentration of solute, 0.68M and .05M solutions of ammonium molybdate tetrahydrate (Sigma-Aldrich 277908) were prepared in a mixture of distilled water and dimethylformamide in a ratio of 5:1 respectively. The solutions were vigorously stirred to obtain a homogenous mixture. A muddy solution was obtained for 0.68M concentration solution. In case of 0.05M solution, a clear solution was obtained, upon aging a top layer was noticed equivalent to amount of DMF in the solution. The top layer was used for FSP. The solutions were filled in a syringe and fed into the FSP system at a rate of 5ml/min. The flame comprised of 1.5 slm (standard liters per minute) methane and 3.0 slm oxygen gas. A 5slm oxygen gas flow was used as dispersion gas. The particles obtained after FSP process (as synthesized particles) were black in color, upon thermal treatment at 500^0C for 5 hours the color of the particles changed to white (calcined).

The powders were characterized using Scanning Electron Microscopy (SEM, LEO 1550), Transmission Electron Microscopy (TEM, JEOL 1400) and selected area electron diffraction was carried out on both as synthesized and calcined samples. Thermogravimetric analysis (TGA, Perkin Elmer Diamond) was conducted on the as synthesized samples. The particles, both as synthesized and calcined, were also characterized using XRD (Rigaku Miniflex II) and FTIR (Thermo Scientific Nicolet 6700).

For sensing experiments, sensors were prepared by drop coating a slurry of as synthesized particles (.68M) in ethanol, on sensor substrates. The sensors were then thermally treated at 500^0C for 5h. Sensing data was collected using a gas flow bench and multimeter. A stable baseline was obtained for the sensors in extra dry air; 485^0C was used as the operating temperature. Sensing data was collected for ammonia in the concentration of 4, 2.5,1 and 0.5ppm.

3.3 Results

3.3.1 X-Ray Diffraction

XRD data for powders before and after thermal treatment was obtained (fig. 3.1a). The XRD pattern obtained for as synthesized powders (both 0.68M and 0.05M) coincides with JCPDS file 80-0757, which is for triclinic ammonium molybdenum oxide $(NH_4)_2(Mo_4O_{13})$. In case of as-synthesized particles from .05M solution, amorphous particles were also noticed. The formation of compound can be attributed to the flame degradation of precursor, ammonium molybdate tetrahydrate, and entrapment of ammonia and water vapors inside the powders during particle formation. In case of XRD for powders upon calcination the peaks observed coincide with JCPDS file 05-508, which is for α-MoO_3.

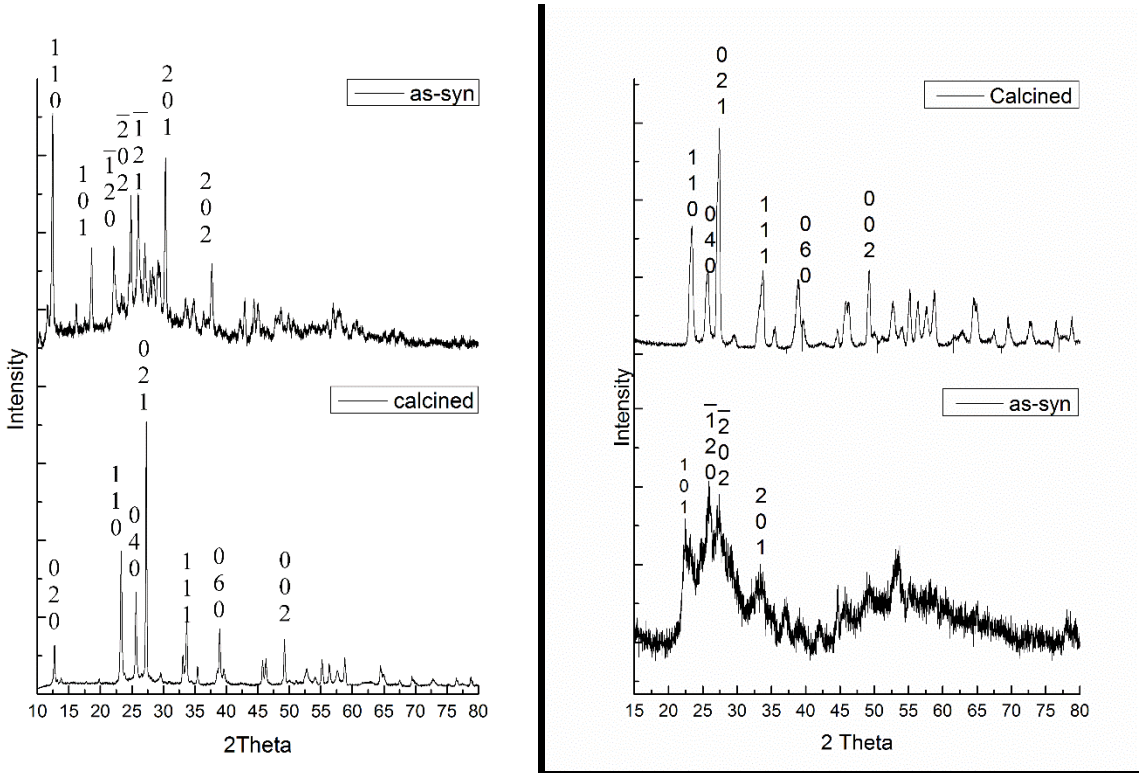

Figure 3-1: XRD spectra (a) as-synthesized and calcined .68M FSP particles (b) as-synthesized and calcined .05M FSP particles

3.3.2 Fourier Transform Infrared Spectroscopy

The FTIR analysis of the powders is shown in fig. 3.2. In case of the FTIR spectrum for as synthesized powders, peaks are noticed at 840,850, 980, 1400, 1640 and 3140 cm^{-1}. The peaks at 3140 and 1640 cm^{-1} can be attributed to water as per NIST database[17], the peaks at 840 and 980 cm^{-1} relates to N-H bonds and inclusion of NH_3 in the sample[17]. Only one peak, found at 850

cm^{-1} relates to the Mo-O-Mo[18]. For powders received upon thermal treatment, peaks were noticed at 818, 850 and 999 cm^{-1}. The strong peak at 850 and the weak peak at 818 cm^{-1} are a result of Mo-O-Mo bond, with the weak peak a resultant of asymmetric molybdenum stretching[18]. The strong peak at 999 cm^{-1} is a result of Mo=O[18, 19]; which indicates a layered structure. No peaks were obtained for water, indicating the water molecules included in the precursor were decomposed during processing.

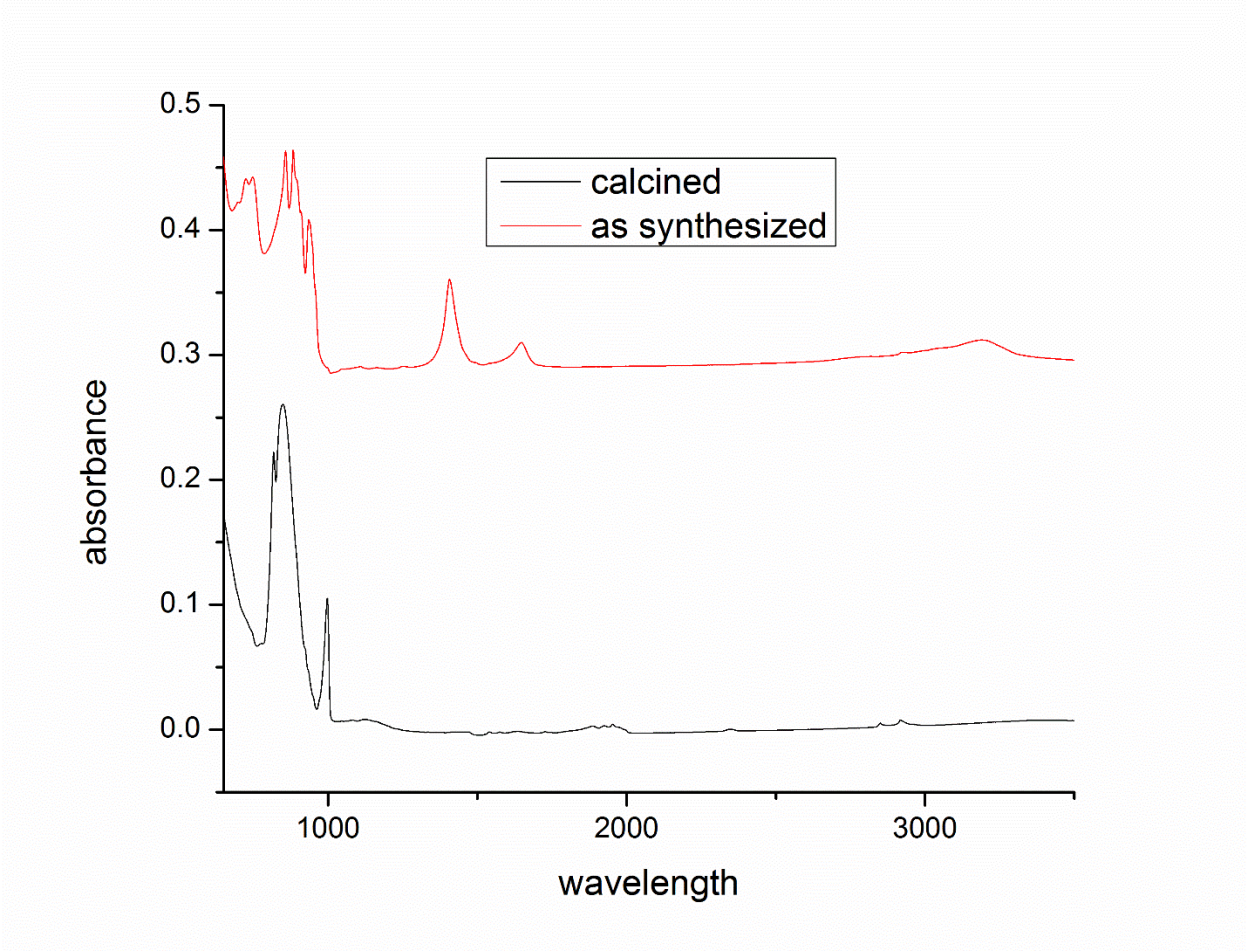

Figure 3-2: FTIR spectra for assynthesized and calcined powders

3.3.3 Thermogravimetric analysis

Thermogravimetric analysis was performed on the as synthesized powders from room temperature to 580ºC under oxygen atmosphere. Fig. 3.3 shows the effect of temperature on the powders. A sharp drop in the weight is noticed at 325^0C indicating the decomposition of ammonium salt and formation of α-MoO_3. The decomposition temperature for $(NH_4)_2(Mo_4O_{13})$ was found to be in accordance with the literature[20], where an endothermic reaction was reported

at the 317^0C; NH_3 & H_2O were the decomposition products and α-MoO_3 was reported as the final product. No change was noticed upon further increasing the temperature to 550^0C or during the cooling process indicating formation of a thermally stable phase.

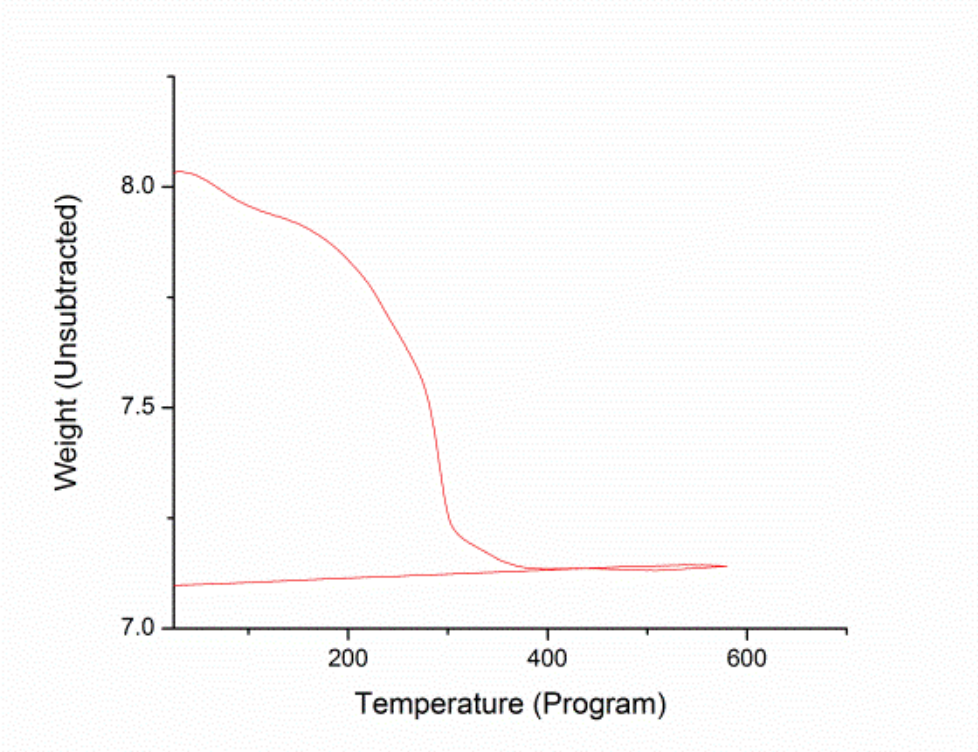

Figure 3-3: TGA analysis of as synthesized particles

3.3.4 Scanning Electron Microscopy

Figure 3.4 shows the scanning electron micrographs obtained for .68M as-synthesized (3.4 a, b), .05M as-synthesized (3.4 c,d), .68M calcined (3.4 e,f) and .05M calcined (3.4 g,h) powders. For as-synthesized 0.068M particles, the morphology was found to be nanorods (20-40nm diameter covering spheres (~1µm diameter)). In case of as-synthesized powders from 0.05M solution, the particles were spheres (1-4 µm diameter) covered by smaller sized particles (10-50 nm). High resolution SEM revealed the spheres to be agglomerates of small particles as can be seen in fig. 3.4d. For the calcined 0.068M powders, the morphology observed was nanosheets with thicknesses in the range of 20-40nm, width in the range of 700-800nm and length in the range of 1-1.5µm. No micron sized spheres where found, indicating a complete transformation of spheres from as- synthesized sample into nanosheets. In case of calcined 0.05M particles, few nanosheets

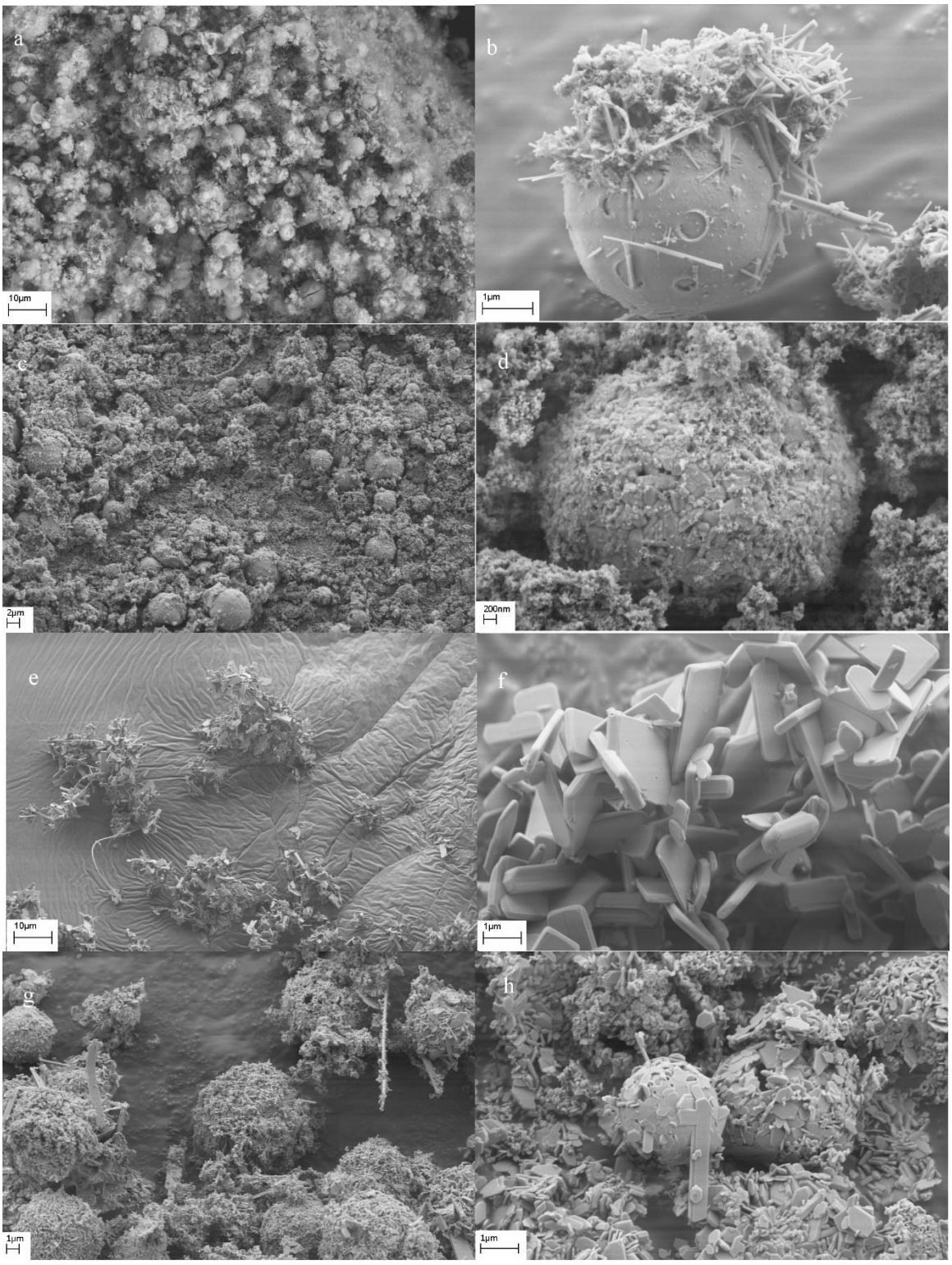

Figure 3-4: Scanning Electron micrographs for (a,b) 0.68M as-synthesized, (c,d) 0.05M as-synthesized, (e,f) 0.68M calcined, and (g,h) 0.05M calcined powders

(Width 500-600 nm, length 1-1.5 µm and thickness 20-40 nm) were noticed. However, majority of the particles were found to be in form of nanoplates with a size range of (80-120 nm). Few micron sized spheres were also noticed, these spheres were found to be agglomerates of nanoplates.

3.3.5 Transmission Electron microscopy

Figure 3.5 shows the transmission electron micrographs and selected area electron diffraction patterns for as-synthesized (0.68M (a,e) & 0.05M (b,f)) and calcined (0.68M (c,g) & 0.05M (d,h)) particles. The micron sized particles weren't seen in the TEM micrographs. The morphology of particles is illustrated in Table 3.1.For the as-synthesized 0.68M particles, nanorods were observed (Fig. 3.5a). The nanorods found on spherical particles of as-synthesized material were characterized using TEM and SAED (Fig. 3.5e). The nanorods were found to be amorphous, SAED pattern picked up signals from lowly crystalline particles in the background. However, no evidence was found for the existence of α-MoO_3 in as-synthesized samples.

For the 0.05M as-synthesized particles, small particles in the range of 10-20nm were noticed. A large agglomeration of particles, comprising of 40-50nm sized nanoparticles was also noticed. The SAED pattern revealed the particles to be amorphous. In case of calcined 0.05M particles (fig. 3.5 d), mixed structures in the form of nanoplates (50-100nm) and nanosheets (150nm width) were observed. The rings from corresponding SAED pattern (fig. 3.5h) matched with JCPDS 05-508 for α-MoO_3 (040, 111 and 210 planes).TEM on calcined 0.68M particles revealed thick structures in form of nanosheets with 600-700nm width, as was observed by SEM. The rings from corresponding SAED pattern (fig. 3.5g) matched with JCPDS 05-508 for α-MoO_3 (110, 111 and 211 planes). Thus, confirming the XRD analysis.

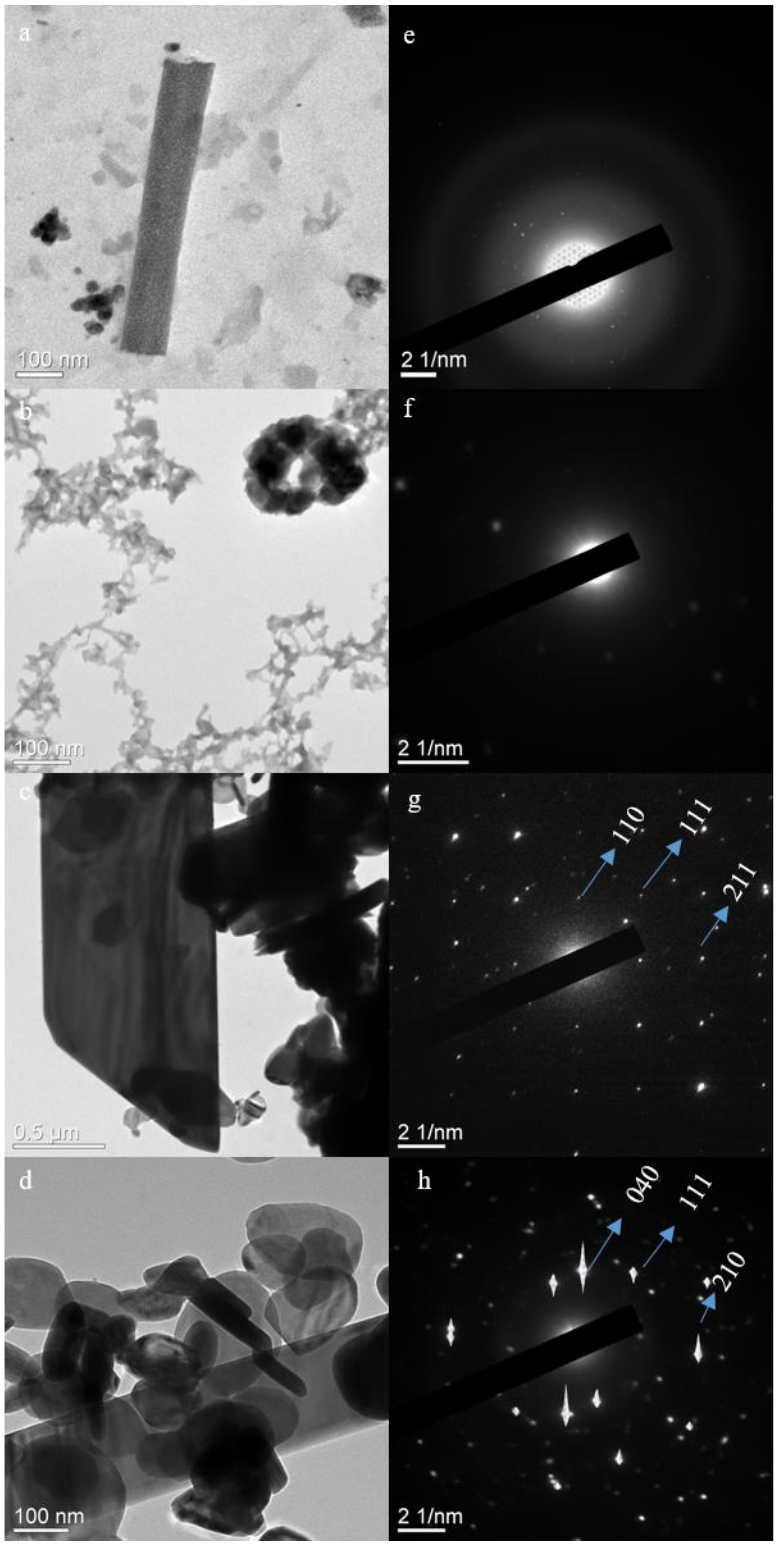

Figure 3-5: TEM images and corresponding SAED patterns for (a,e) 0.68M as-synthesized (b,f) 0.05M as-synthesized (c,g) 0.68M calcined and (d,h) 0.05M calcined particles

Table 3-1: morphology and particle size for fsp powders

Sample	Morphology	Particle Size
0.68M as-synthesized	spheres	~1 µm diameter
	Nanorods	20-40nm
0.05M as-synthesized	Spheres	1-4 µm diameter
	Nanoparticles	10-50nm
0.68M calcined	Nanosheets	20-40nm thickness, 700-800nm width & 1-1.5µm length.
0.05M calcined	Nanoplates	50-100nm
	Nanosheets	150nm width,

3.3.6 Ammonia Sensing

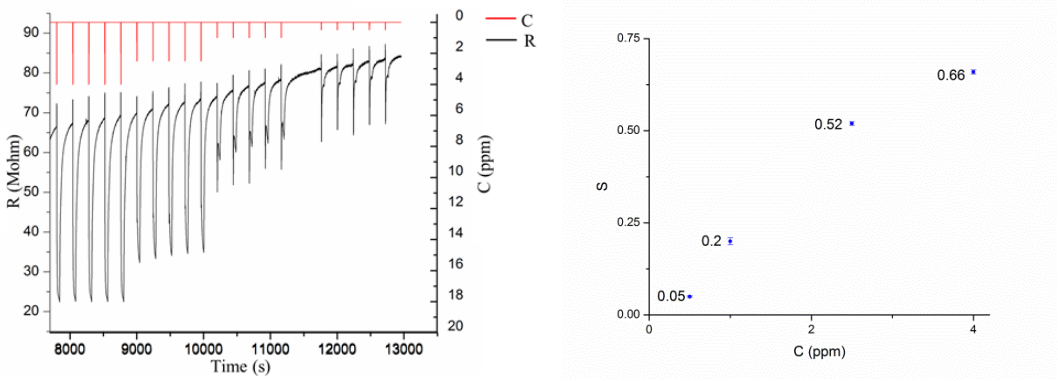

Figure 3-6: (a) Sensing data for ammonia at 485^{0}C (b) Sensitivity plot for ammonia

Nanosheets obtained from calcined 0.68M particles were tested for ammonia sensor operated at 485^{0}C in extra dry air and ammonia in the concentration (denoted by C on graphs) of 4ppm, 2.5ppm, 1ppm, and 0.5ppm. The sensors showed fast response time of 40 seconds. The sensing data is plotted against time, as can be seen in figure 3.6a; R (y1 axis) vs Time represents

the change in resistance when a signal of ammonia was introduced, C (y2 axis) vs Time represents the times when a 3 second pulse of ammonia was introduced. The sensors were found to show high sensitivity, the sensitivity of the sensors at different concentrations of ammonia is shown in figure 3.6b.

3.4 Discussion

The particle phase and morphologies were greatly affected by the concentration of solute and percentage of organic solvent in the precursor. Large particle sizes were observed for solution with higher concentration of solute and aqueous solution. For 0.68M solution the particles formed were micron sized and hollow, with a shell structure, as noticed via SEM. The formation of hollow micron particles were due to an inhomogeneous aqueous solution. The temperature of operation was significantly lowered due to presence of water in the solution, the lower temperatures prevented complete vaporization of particles and led to the formation of an intermediate ammonium molybdenum oxide phase. The particles synthesized using a 0.05M solution also showed inclusion of some shell like hollow particles, based on the results from 0.68M solution it can be said that these particles were made of ammonium molybdenum oxide. Large amount of nano-sized particles were noticed via SEM analysis. These particles were amorphous in nature as confirmed by TEM. Since there was a higher amount of organic solvent in the 0.05M precursor solution, nano-sized particles were formed. The formation of these nano-sized particles can be attributed to the organic additive decomposition during sintering process. The process map for formation of particles through FSP is shown in fig. 3.7.

Upon heat treatment at 500°C, as-synthesized powders from both 0.68M and 0.05M solutions changed into α-MoO_3. The phase was verified by XRD and SAED studies. The morphology of the calcined 0.68M particles were in the form of nanosheets. Such morphology was reported earlier for flame synthesized MoO_3 in doped form[15] and by our group for MoO_3 obtained after thermal degradation of electrospun mats[2] . The formation of the nanosheets is due to the low energy configuration for α-MoO_3 particles. The thermodynamically stable form consists of 2 similar chains of MoO_6 octahedra aligned in *ab* configuration[21]. Similar trend was observed upon calcination of as-synthesized particles from 0.05M solution. However, three different morphologies in the form of nanosheets and nanoplates were observed. The formation of nanosheets was a result of oxidation and rearrangement of micron sized ammonium molybdenum

oxide particles, as was the case for particles obtained from 0.68M solution. The formation of nanoplates can be attributed to the crystallization of nano-sized particles in the as-synthesized powders.

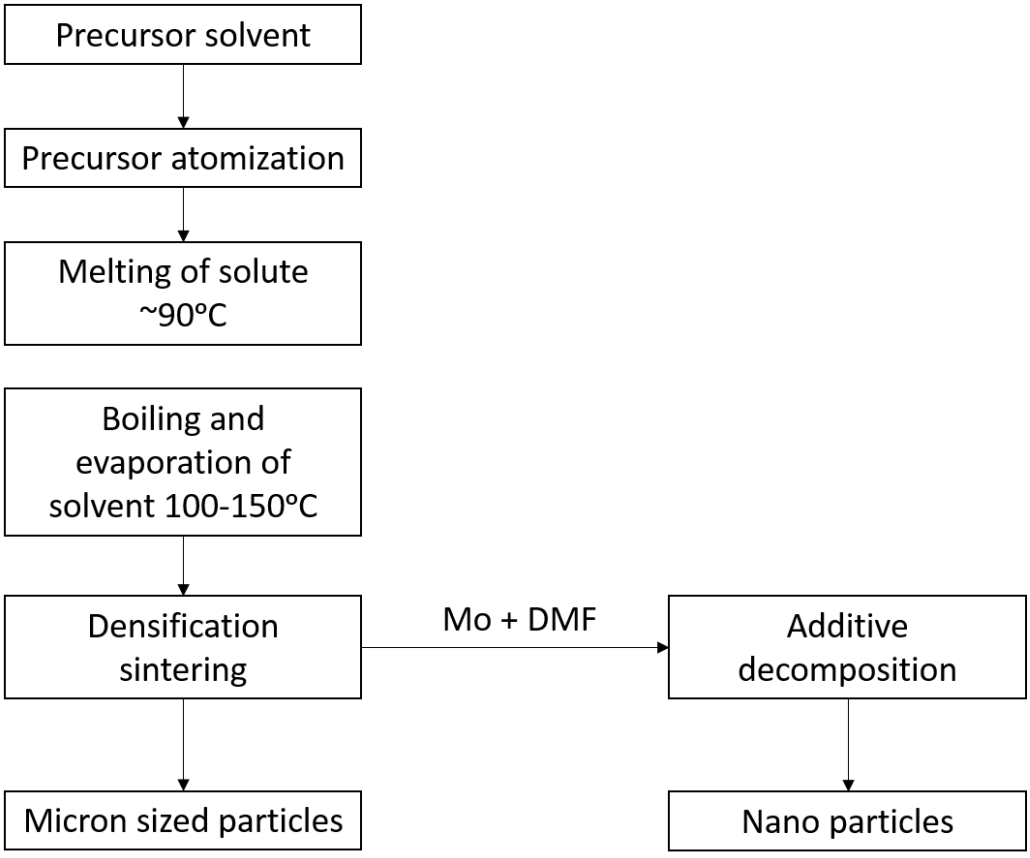

Figure 3-7: Process map for fsp of Mo-precursors

For the sensing experiments, the sensors showed a fast response to ammonia, with a significant lowering of the resistance of the material (high sensitivity), even at low gas concentrations (low detection limit). Most of the earlier reported MoO_3 based ammonia sensors have been shown to detect 10ppm or higher concentrations of ammonia. Gouma et al.[14] have been able to detect concentrations of ammonia down to 50ppb using spin coated MoO_3 synthesized through sol-gel process. The current flame-synthesized sensor wasn't tested for such low concentrations, however, when the two sensors are compared for their sensitivity for 1ppm of ammonia; the flame synthesized sensors show a slightly better sensitivity (0.2) compared to the spin-coated one (.14). The sol-gel derived sensor showed a sensitivity of 0.01 at 50ppb concentrations; the FSP-processed sensor by extrapolation of the sensitivity graph is expected to

reach 0.01. The comparable performance of the FSP derived sensor to sol gel may open the path for the scalable synthesis of ammonia sensors for use in fields like breath-based diagnostics [14]. In its current form, the flame synthesized sensors show a sensitivity of .005 at 500ppb range and can find applications in automotive industry to monitor emissions from the selective catalytic system in the exhaust of automobiles[22, 23].

3.5 Conclusion

Our study successfully demonstrates the synthesis of pure un-doped α-MoO_3 through flame spray pyrolysis process. The size and morphology of α-MoO3 can be controlled through the concentration of solute and organic solvent in the precursor solution. The sensors obtained show fast response and recovery times, good sensing resolution and high sensitivity at low concentrations of ammonia. Moreover the sensing results were found comparable to sol gel derived sensor developed for breath diagnostics. Hence, the synthesis method opens the pathway for commercial synthesis of α-MoO_3 sensors for breath diagnostics.

References

1. Sawicka, K.M., A.K. Prasad, and P.I. Gouma, *Metal Oxide Nanowires for Use in Chemical Sensing Applications.* Sensor Letters, 2005. **3**(1-1): p. 31-35.
2. Gouma, P., K. Kalyanasundaram, and A. Bishop, *Electrospun single-crystal MoO3 nanowires for biochemistry sensing probes.* Journal of Materials Research, 2006. **21**(11): p. 23.
3. Dewangan, K., et al., *Synthesis and characterization of single-crystalline alpha-MoO3 nanofibers for enhanced Li-ion intercalation applications.* Crystengcomm, 2011. **13**(3): p. 927-933.
4. Iriyama, Y., et al., *Transmission electron microscopy (TEM) analysis of two-phase reaction in electrochemical lithium insertion within alpha-MoO3.* Solid State Ionics, 2000. **135**(1-4): p. 95-100.
5. Zhou, L., et al., *alpha-MoO3 Nanobelts: A High Performance Cathode Material for Lithium Ion Batteries.* Journal of Physical Chemistry C, 2010. **114**(49): p. 21868-21872.
6. Brezesinski, T., et al., *Ordered mesoporous alpha-MoO3 with iso-oriented nanocrystalline walls for thin-film pseudocapacitors.* Nature Materials, 2010. **9**(2): p. 146-151.
7. Liang, R., H. Cao, and D. Qian, *MoO3 nanowires as electrochemical pseudocapacitor materials.* Chemical Communications, 2011. **47**(37): p. 10305-10307.

8. Murugan, A.V., et al., *Highly efficient organic-inorganic poly(3,4-ethylenedioxythiophene)-molybdenum trioxide nanocomposite electrodes for electrochemical supercapacitor*. Journal of Applied Physics, 2006. **100**(7).
9. Sha, X., et al., *Hydrogen Absorption and Diffusion in Bulk alpha-MoO3*. Journal of Physical Chemistry C, 2009. **113**(26): p. 11399-11407.
10. Tang, W., et al., *An aqueous rechargeable lithium battery of excellent rate capability based on a nanocomposite of MoO3 coated with PPy and LiMn2O4*. Energy & Environmental Science, 2012. **5**(5): p. 6909-6913.
11. Liu, Y., et al., *A nanocomposite of MoO3 coated with PPy as an anode material for aqueous sodium rechargeable batteries with excellent electrochemical performance*. Electrochimica Acta, 2014. **116**: p. 512-517.
12. Rao, M.C., et al., *Structural Stoichiometry and Phase Transitions of MoO3 Thin Films for Solid State Microbatteries*. Research Journal of Recent Sciences, 2013. **2**(4): p. 67-73.
13. Prasad, A.K., D. Kubinski, and P.I. Gouma, *Comparison of Sol-Gel and RF Sputtered MoO3 Thin Film Gas Sensors for Selective Ammonia Detection*. Sensors and Actuators B, 2003. **9**: p. 25-30.
14. Gouma, P., et al., *Nanosensor and Breath Analyzer for Ammonia Detection in Exhaled Human Breath*. IEEE Sensors Journal, 2010. **10**(1): p. 49-53.
15. Park, G.D., S.H. Choi, and Y.C. Kang, *Electrochemical properties of ultrafine TiO2-doped MoO3 nanoplates prepared by one-pot flame spray pyrolysis*. RSC Advances, 2014. **4**(33): p. 17382-17386.
16. Zhang, G. and M. Liu, *Effect of particle size and dopant on properties of SnO2-based gas sensors*. sensors and Actuators B: Chemical, 2000. **69**(1-2): p. 144-152.
17. Linstrom, P.J. and W.G. Mallard, *NIST Chemistry WebBook*, in *NIST Standard Reference Database Number 69,*. National Institute of Standards and Technology, Gaithersburg MD.
18. Sharma, R.K. and G.B. Reddy, *Synthesis and characterization of α-MoO3 microspheres packed with nanoflakes*. Journal of Physics D: Applied Physics, 2014. **47**(6).
19. Reddy , C.V.S., et al., *An electrochemical investigation on (MoO3+PVP+PVA) nanobelts for lithium batteries*. Journal of Solid State Electrochemistry, 2007. **11**.
20. Kovács, T.N., et al., *Thermal decomposition of ammonium molybdates*. Journal of Thermal Analysis and Calorimetry, 2016. **124**(2): p. 1013-1021.

21. Oswald, H.R., J.R. Gunter, and E. Dubler, *Topotactic decomposition and crystal structure of white molybdenum trioxide-monohydrate: Prediction of structure by topotaxy.* Journal of Solid State Chemistry, 1975. **13**(4): p. 330-338.
22. Prasad, A.K. and P.I. Gouma, *MoO3 and WO3 based thin film conductimetric sensors for automotive applications.* Journal of Materials Science, 2003. **38**(21): p. 4347-4352.
23. P.I. Gouma, M.S., and S. Simon, *An Overview of the translation of selective semiconducting gas sensors from first results to automotive exhaust gas monitors to a platform for breath-based diagnostics.* Translational Materials Research, 2015. **2**(4).

Chapter 4: Effect of precursor solution on flame spray synthesis of ε-WO_3 polymorphs

4.1 Introduction

WO_3 is a well-studied material due to its variety of applications and polymorphic states. In bulk, it exhibits a monoclinic ε-phase between the temperature ranges of -273°C to -40°C; a triclinic δ-phase is found between -40°C to 17°C. The stable phase for WO_3 at room temperature is the monoclinic γ-phase that exists between the temperature ranges of 17-330°C. Over the temperature range of 330ºC WO_3 exhibits two more crystalline states which are an orthorhombic β-phase (330-740°C) and a tetragonal α-phase (740-900°C)[1]. Two metastable phases also exist for WO_3 which are a hexagonal phase[2] and a cubic phase[3].

Compared with the other five phases of tungsten trioxide, ε – phase has unique physical properties such as its ferroelectric nature[1], anisotropic electrical transport properties[4], and has an dipole moment [5]. These unique physical properties are derived from its structure.

The ε phase of WO3 has a quite different structure from any other stable phase, which is exactly the truth. Like other stable phases, ε-WO3 can also be treated as the distortion of an ideal ReO3-like structure. However, different from other phases, such distortion does not occur only between adjacent [WO6] units, but also inside every unit. For ε-phase the shifts in the negative z direction are larger than those in the positive z direction[4, 5]. Because of the inequality of shifts in the z direction, a net spontaneous polarization develops. This is the origin of the ferroelectricity in the ε phase. The ferroelectric property and dipole moment exhibited by the ε-WO_3 enable them to act as a selective gas sensor for acetone detection[6].

Various techniques have been used for the synthesis of ε-WO_3. The techniques used are pulsed laser deposition[7], pulsed spray pyrolysis[8], facile solvothermal method[9], Reactive magnetron sputtering[10] and flame spray pyrolysis[6, 11]. Among the various processes used, FSP is the most attractive process for synthesis of ε-WO_3 due to its self-sustaining and high temperature flame, use of less volatile precursors, large temperature gradients, and scalability.

The current literature on ε–WO_3, with high phase content and thermal stability, require dopants for stabilization of the polymorph, the addition of dopants might significantly hamper the properties of the polymorph. FSP has been used for synthesis of ε–WO_3 in pure form, however, the resulting material had low % ε–WO_3 content and transformed into γ-WO_3 upon annealing. The transformation of gamma was associated with increase in particles size. In this study, we aim at

synthesizing ε-phase from fsp without doping by taking precursor dynamics and particle formation mechanism into account. A tungsten isopropoxide sol is used, which is a preferred compound for flame synthesis[12]. For comparison studies, 10% Cr-doped materials are also synthesized.

4.2 Experimental Methods

Two different precursor solutions were prepared for FSP synthesis of WO_3.

I. Tungsten Isopropoxide in Iso-propanol

To prepare the precursor solution, Tungsten isopropoxide (W-iso) was dissolve in 2-propanol in 0.38 M concentration in N2 filled glove box. Selection of Tungsten isopropoxide was due to its combustible nature (455ºC) which facilitates gas phase mechanism for FSP and leads to formation of nanoparticles. Iso-propanol was selected as a solvent to avoid reaction between the solute and solvent. The solution was stirred using an ultrasonicator and aged for 24h before being fed in the FSP.

II. Ammonium tungstate with 10% Chromium acetyl-acetonate in diethylene glycol monobutyl ether/ethanol

The recipe used here has been used earlier by our group[13]. Precursor solutions are prepared from ammonium tungstate hydrate (H26N6O41W12, Aldrich, purity >97%) diluted (0.4 mol/l of tungsten ions) in a 3:2 (volume ratio) mixture of diethylene glycol monbutyl ether (C8H18O3 Fluka, >98.5%) and ethanol (C2H6O, Fluka, >99.5%). Chromium (III) acetyl-acetonate ((C5H7O2)3Cr) is used for Cr doping. These materials are added into the precursor solution with 10%molar ratios to ammonium tungstate hydrate, but keep the total concentration of metal ions constant at 0.4 mol/l.

For FSP synthesis, the solutions were filled in a syringe and fed into the FSP system at a rate of 5ml/min. The flame comprised of 1.5 slm (standard liters per minute) methane and 3.0 slm oxygen gas. A 5slm oxygen gas flow was used as dispersion gas. The particles were calcined at 500ºC.

The as-synthesized Cr-doped powders were characterized using Scanning Electron Microscopy (SEM, LEO 1550) with EDS. Transmission Electron Microscopy (TEM, JEOL 1400)

and selected area electron diffraction was carried out on both as synthesized and calcined samples. FTIR and DSC was conducted on the as synthesized samples. The particles, both as synthesized and calcined, were also characterized using XRD (Rigaku Miniflex II) and UV-Vis (Lambda 950).

4.3 Results

4.3.1 X-Ray Diffraction

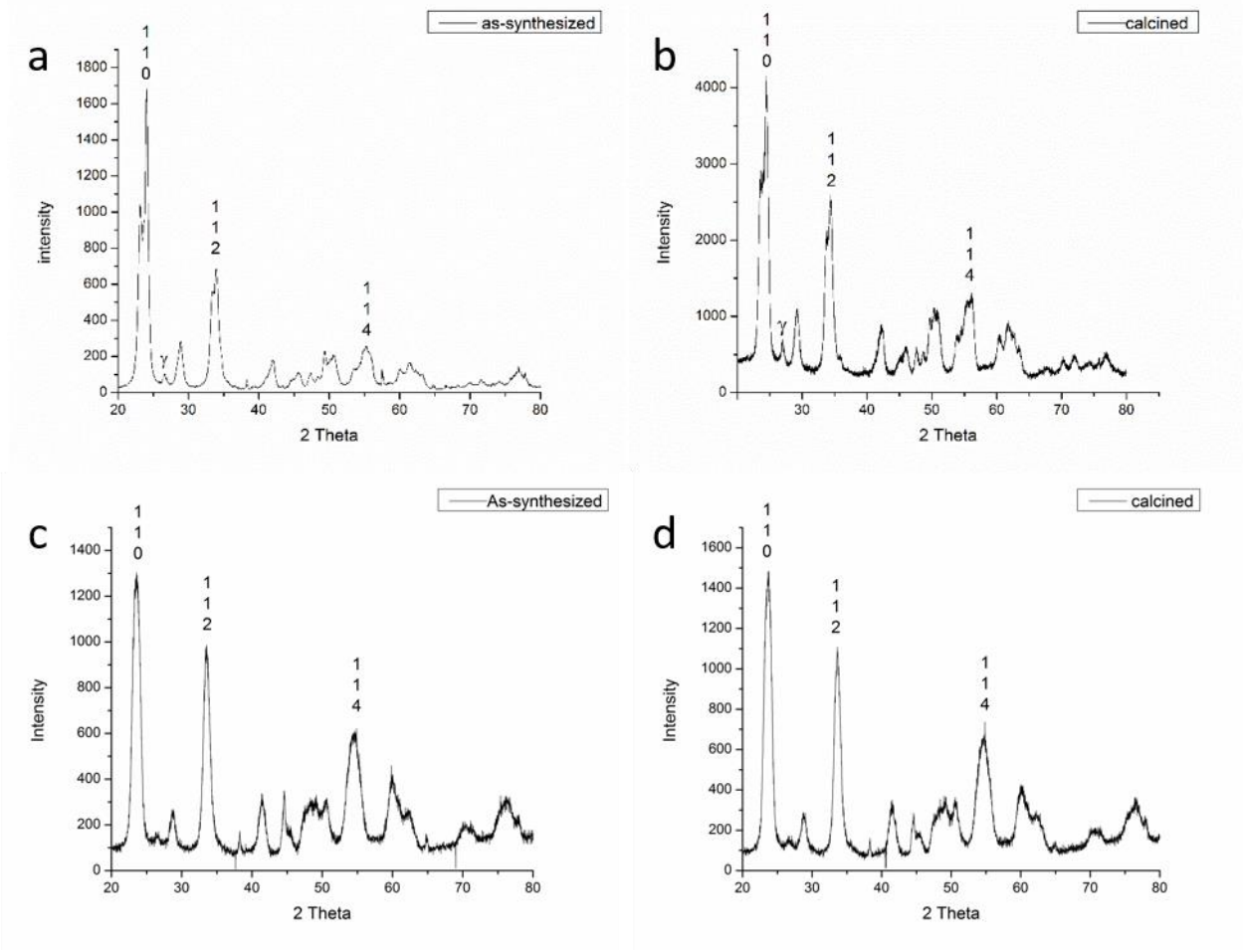

Figure 4-1: X-ray diffraction pattern for (a) As-synthesized pure WO_3 (b) calcined pure WO_3 (c) As-synthesized Cr-doped WO_3 (d) calcined Cr-doped WO_3

XRD on the powders resulted in a mixed γ-WO_3 (JCPDS 83-950, monoclinic WO_3) and ε-WO_3 phases (JCPDS 23-87-2386, monoclinic WO_3). The characteristic peaks for ε-WO_3 are labelled in Figure 4.1, the characteristic peak for γ-WO_3 is denoted with a γ and is for (120) plane. The percentages of each phase was calculated using Reference Intensity Ratio method (RIR).

Scherrer's formula was used to calculate the crystalline sizes for each phase. Table 4.1 lists the percentage and crystalline sizes of γ-WO_3 and ε-WO_3 in each sample.

Table 4-1**:** Phase content and size of WO_3 nanopowders based on the XRD data

Sample	Phase %		Crystalline size (nm)	
	γ	ε	γ	ε
Pure WO_3 assynthesized	55	45	22	11.5
Pure WO_3 calcined	58	42	31	14
WO_3 Cr-doped assynthesized	61	39	34	13
WO_3 Cr-doped calcined	61	39	40	14

4.3.2 Scanning Electron Microscopy

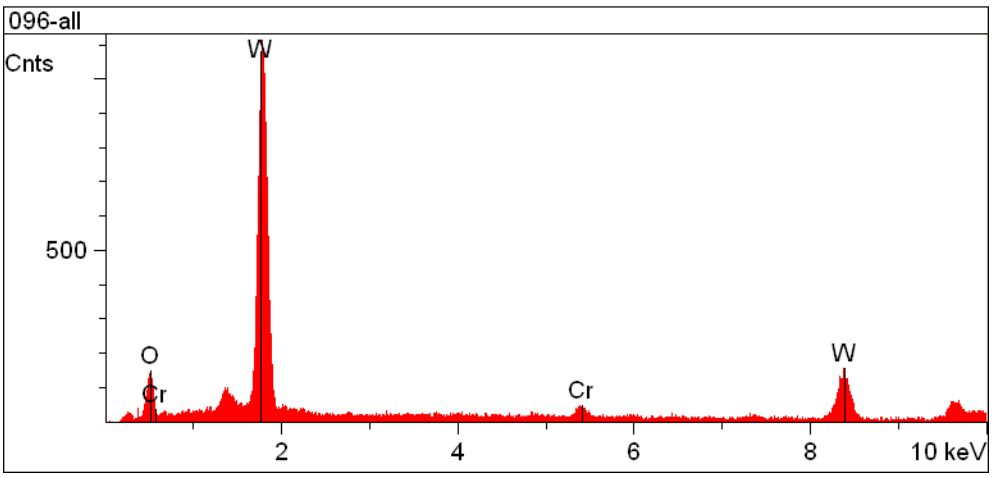

Figure 4-2: (a) Scanning Electron Micrograph for Cr-doped WO_3 (b) EDS for Cr-doped WO_3

Due to small size of the particles, SEM imaging did not yield any information on the morphology. Figure 4.2(a) shows the Cr-doped particles. EDS was conducted on Cr-doped WO_3 to confirm inclusion of Cr in the FSP synthesized powders.

4.3.3 Transmission Electron Microscopy

Figure 4.3 shows the transmission electron micrographs for as-synthesized (pure (a,b) and Cr-doped(c,d)) and calcined (pure (e,f) and Cr-doped(g,h)). All the particles were in form of nanospheres, however, two different size distributions were noticed. Table 4.2 lists the size distribution of the small and large particles.

Table 4-2: Particle sizes of WO_3 Nanopowders based on TEM images

Sample	Diameter for small spheres	Diameter for large spheres
WO_3 isopropoxide assynthesized	10-20 nm	45nm
WO_3 Cr-doped assynthesized	10-20 nm	35nm
WO_3 isopropoxide calcined	10-25 nm	45nm
WO_3 Cr-doped calcined	10-20nm	35nm

SAED pattern for all the samples matched the rings with JCPDS 87-2386 corresponding to the ε-WO_3 phase (110, $\bar{1}12$ and 114). A faint ring was noticed in all but calcined Cr-doped sample. The ring matched with JCPDS 83-950 and corresponds to γ-WO_3 ($\bar{1}12$ plane).

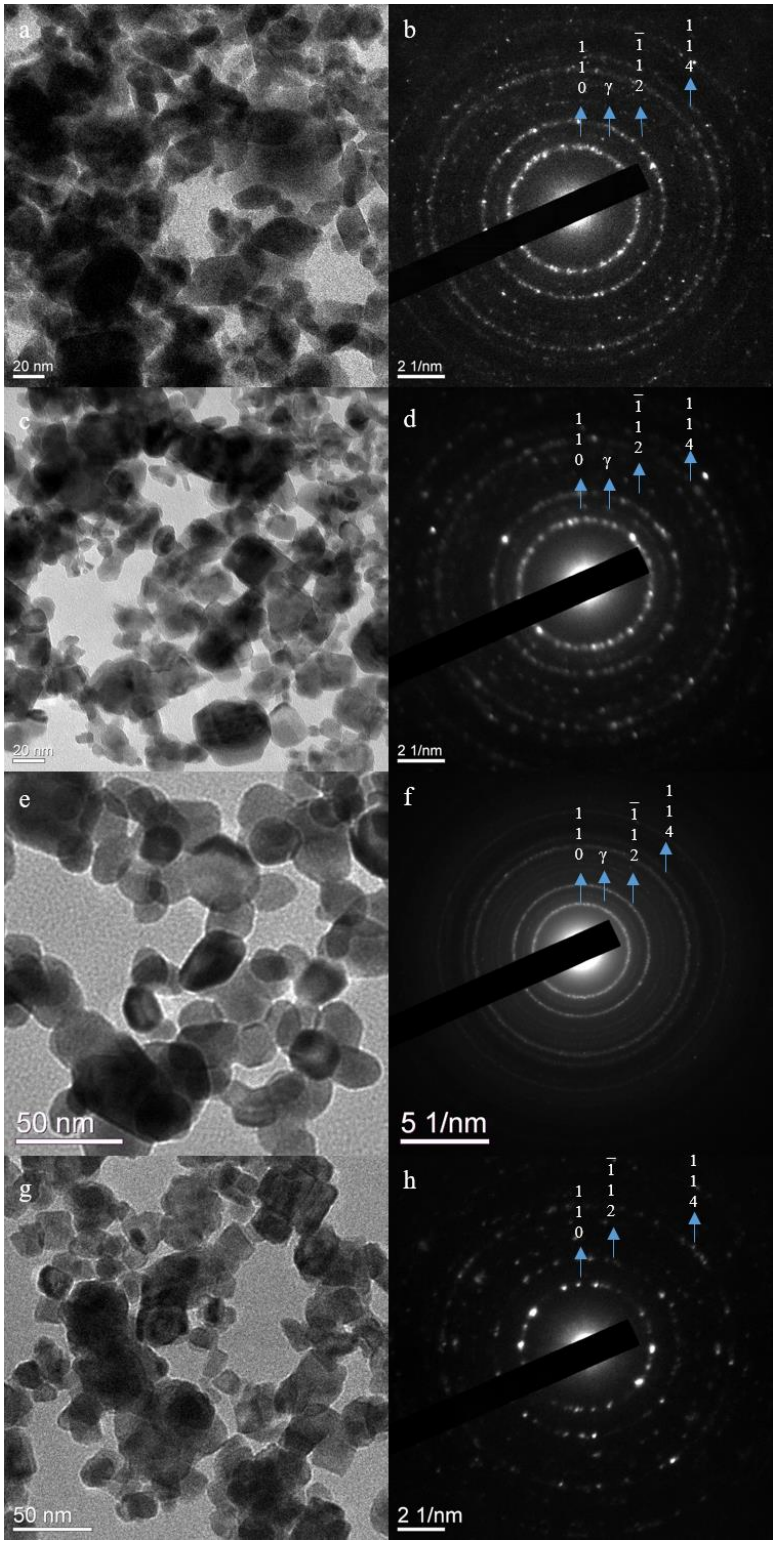

Figure 4-3: TEM images and corresponding SAED patterns for (a,e) pure WO_3 as-synthesized (b,f) Cr-doped WO_3 as-synthesized (c,g) pure WO_3 calcined and (d,h) Cr-doped WO_3 calcined particles

4.3.4 Fourier Transform Infrared Spectroscopy

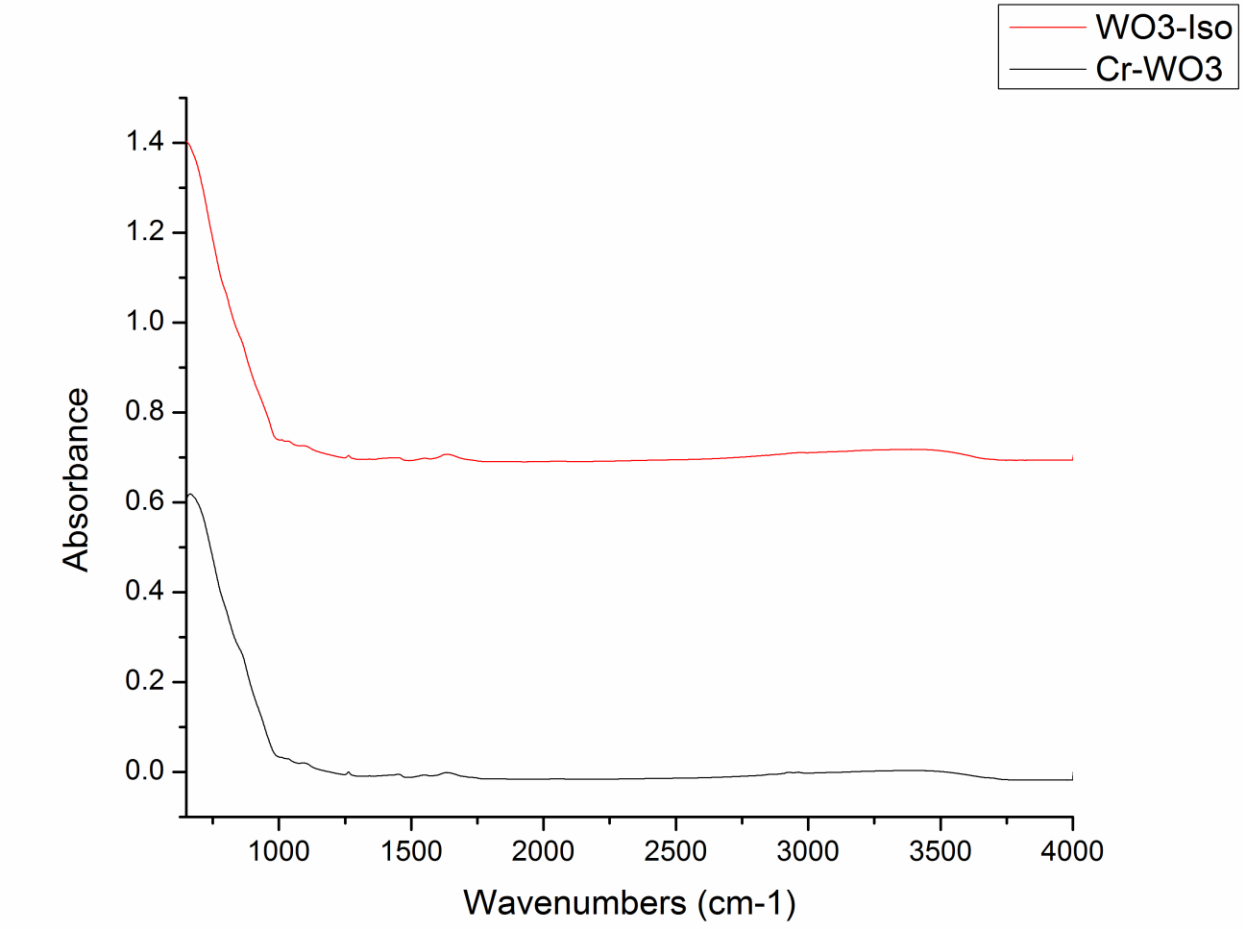

Figure 4-4: FTIR characterization of as-synthesized nanopowders

Depending on the bonds present, Tungsten oxide compounds emit FTIR signal in the 780-900 cm^{-1}. The FTIR analysis carried out on the pure and Cr-doped particles resulted in overlapping of peaks in the 780-900 cm^{-1} region[14]. Thus no useful structural information was obtained for the particles from FTIR characterization. No evidence of entrapped carbon was found in the

samples. Both the samples showed peaks for metal hydratess in 3400-3500 cm^{-1} region, which are a common by-products during the synthesis of WO_3[13].

4.3.5 Differential Scanning Calorimetry

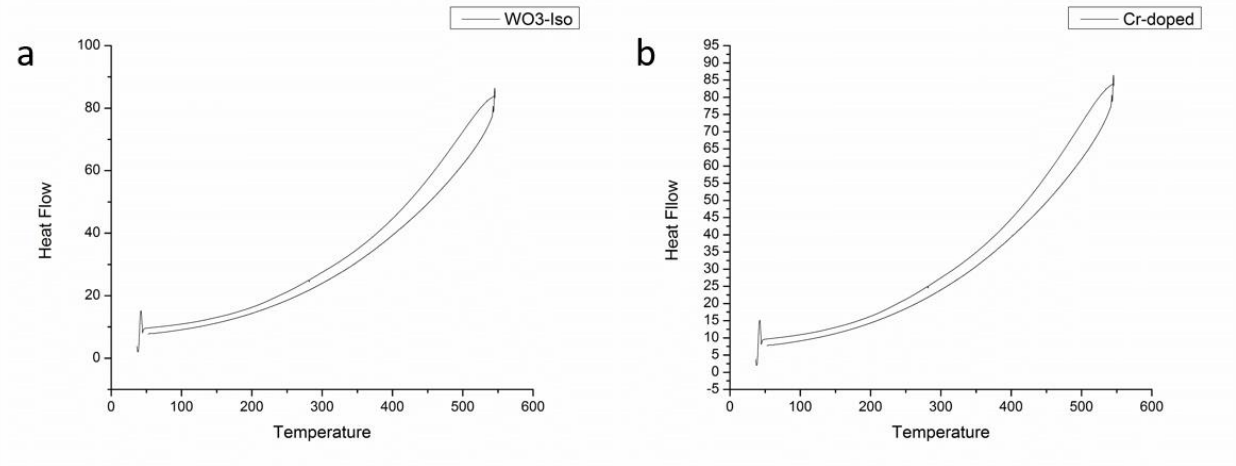

Figure 4-5: DSC (a) pure WO_3 (b) Cr-doped WO_3

DSC was carried out on the as-synthesized samples in the 50-550 region. No phase transformation was noticed in the samples as was confirmed through XRD and SAED. Both the samples were held at 550°C for 10mins. The absence of phase transformation at high temperature indicates thermal stability and opens up the potential application in the field of acetone breathalyzer.

4.3.6 UV-Vis spectroscopy

The UV-Visible spectroscopy carried out to investigate the adsorption properties of pure and Cr-doped WO_3 powders. The Cr-doped powders didn't show a spike in absorbance in the UV-Vis region. The addition of Cr in the powders results in a shift into IR region as has been reported earlier [15]. The pure WO_3 samples showed a strong cutoff at 455nm wavelength. The bandgap energy was calculated using the formula (E) = h*C/λ. Where h:Planck constant = 6.63 x 10-34 J s, C: speed of light = 3.0 x 10^8m/s, λ: cutoff wavelength= 455 x 10^{-9}m. The equation results the

band gap energy in joules and is divided by 1.6×10^{-19} to convert to eV ($1eV = 1.6 \times 10^{-19}$ joules). The calculated bandgap enegy was 2.73eV, which is within the range of reported bandgaps (2.4-2.8eV) for WO_3 compounds[16].

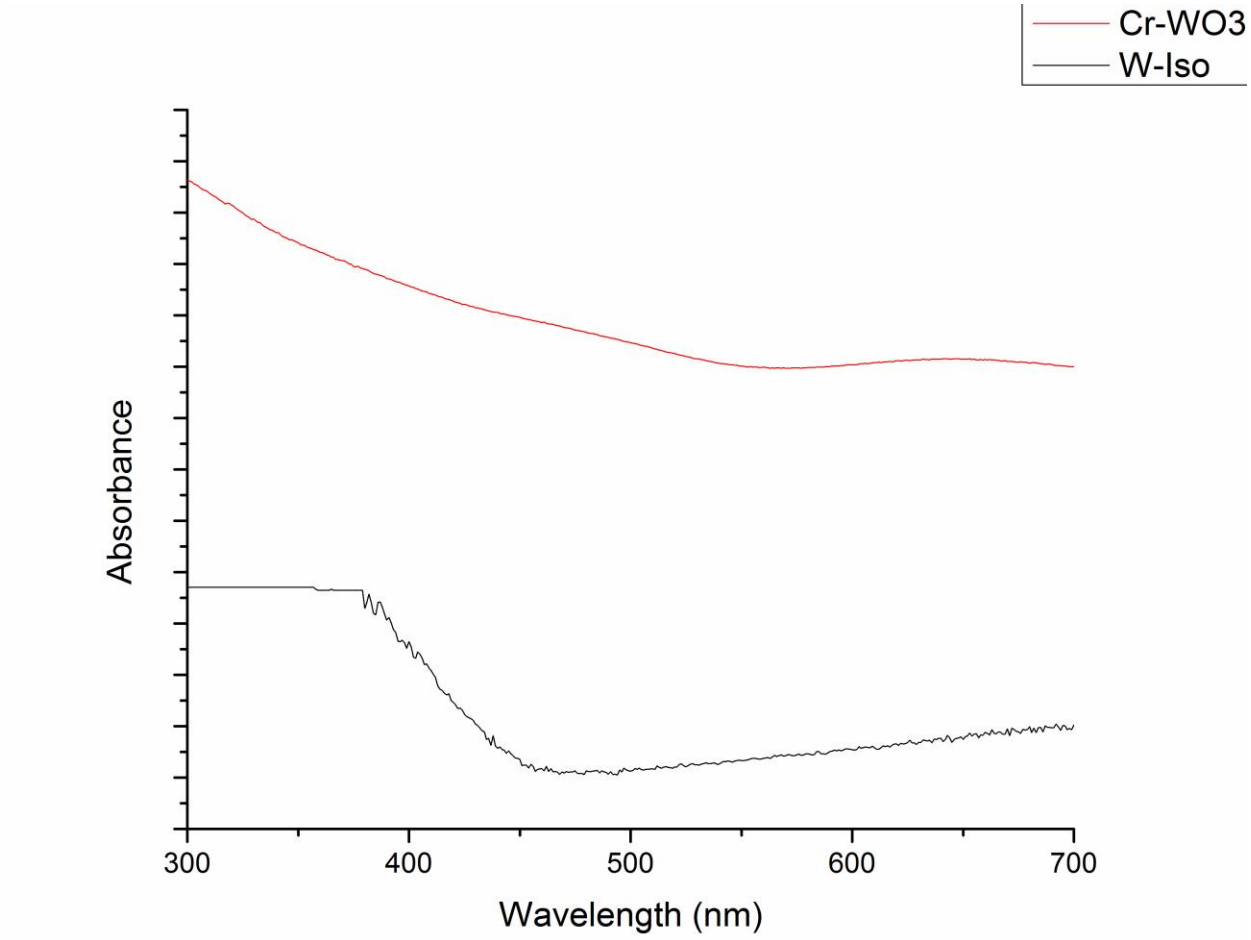

Figure 4-6: UV-Vis spectra for pure and Cr-doped WO_3 particles.

4.4 Discussion

Earlier studies have reported the particle size to play an important role in formation of ε-WO_3 polymorphs[6]. Similar trend was observed for the particles here as per the crystalline sizes calculated from XRD patterns for ε-WO_3 in as-synthesized samples (pure WO_3 11.55nm and Cr-doped 14 nm) and γ-WO_3 (pure WO_3 21.79 nm and Cr-doped 30.88 nm). Analysis of TEM micrographs also gave 2 size distributions. Based on the literature and crystalline sizes, it is safe to assume that the smaller particles in the size range of 10-20nm were of ε-WO_3. The particles for γ -WO_3 40-50nm in size for pure and 30-40nm in size for Cr-doped WO_3.

To understand the formation of ε-WO_3, it is important to understand the formation dynamics of particles through FSP. The size of particles formed in FSP depend on ODOP (one droplet to one particle),ODMP (one droplet to multiple particles) or gas phase transition[17]. For homogenous solutions, ODOP results in formation of uniform particle sizes in submicron or micron range, while ODMP and gas phase result in nanosized particles. Due to combustible nature of tungsten-isopropoxide, gas phase mechanism is preferred by fsp. Both the processes follow gas phase mechanism as the precursors easily transform into vapor phase at higher temperatures (500-600ºC). Tungsten isopropoxide is combustible at 500ºC, the combustion gives rise to an exothermic reaction and leads to formation of tungsten vapors and decomposed organic precursors. The vapors are readily oxidized into WO_3 vapors, which then undergo nucleation and agglomeration. The Cr-doped powders are vaporized into W vapors at ~600ºC, the decomposition of the precursor is an endothermic reaction, and follow the same route as W vapors generated from tungsten isopropoxide solution. Figure 4.7 shows the process map for formation of WO_3 powders through FSP.

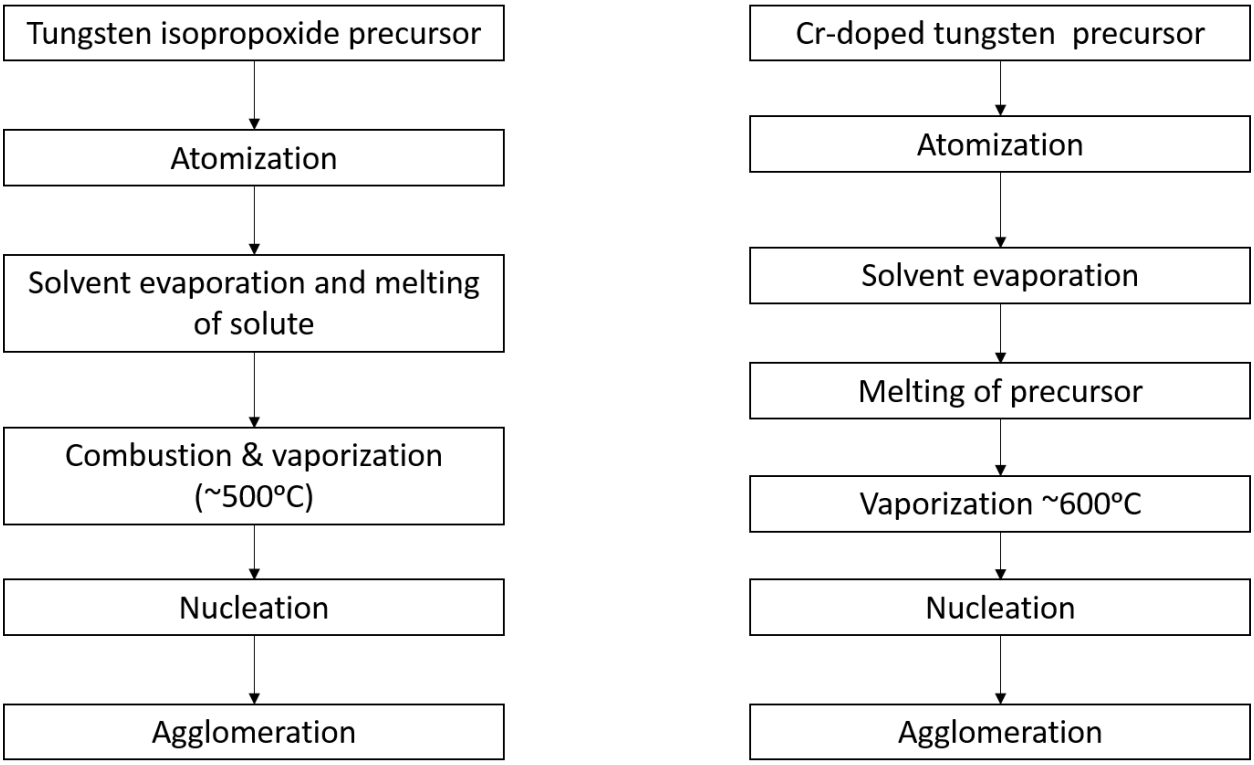

Figure 4-7: process map for formation of WO_3 particles through fsp

The final size of the crystallites depend on the residence time and operating parameters, these are precursor composition, fuel and oxidant flow rate and size of droplet and flame[18]. A direct relation between oxidant flow-rate was noticed for Cr-doped particles. The particles reported here were slightly smaller compared to the particles reported in the literature[13]. The formation of ε-WO_3 particles can further be explained. The precursor solutions upon entering the flame lead to atomization and oxidation of W atoms. The existence of large temperature gradient prefers the formation of ε-WO_3 particles. The particles undergo nucleation, coagulation & agglomeration. The particle size depends on the residence time, which relates to the time the particles spend in the chamber upon atomization. A shorter residence time gives rise to small particle sizes and thus a stabilized ε-WO_3 is received. The formation of γ phase occurs once the critical crystallite size for the particles is crossed, this critical size can be calculated using a heuristic model[19].

Flame spray synthesis was used to produce WO_3 compounds using WCl_6 in tetrahydrofuran[20]. The particle sizes were in the range of 7-10nm. However, particles synthesized here were γ-WO_3. Formation of γ-WO_3 even with a small particle size can be related to the residence time and ODMP. The reaction between WCl_6 and tetrahydrofuran (thf) leads to formation of $WOCl_4$(thf) and dichloromethane[21]. The attachment of organic ligand enables the precursor to undergo ODMP and form small particle sizes. However, the low boiling point of dichloromethane (39.6°C) leads to higher residence time and transformation of the particles into γ-phase. In this study the relative high boiling points of iso-propanol (82.6°C) and ethanol (78.37°C) ensure less residence time and hence result in formation of ε-WO_3 particles.

The percentage of ε phase was slightly higher in pure WO_3 compared to Cr-doped WO_3. The concentration of metal ions in the isopropoxide solution was slightly lower compared to Cr-doped solution. However, the precursor salt also played an important role in formation of higher ε phase content. The exothermic reaction from the combustion of tungsten isopropoxide gives rise to a higher temperature gradient compared to the endothermic decomposition of ammonium salt. The high temperature gradient favors the formation of ε-phase by delaying the nucleation and yielding lower residence time.

Heat treatment of the synthesized particles led to grain coarsening and a slight increase in crystallite size. The pure WO_3 powders saw a drop in % ε-WO_3 content. Once the crystallites for ε-phase cross the critical size barrier, a transformation into γ phase occurred. No drop was noticed in case of Cr-doped powders, as chromium controls the particle size thereby favoring the ε-phase.

4.5 Conclusion

Flame spray pyrolysis allowed us to synthesize ε-WO3 nanopowders with a controlled phase distribution. Use of tungsten isopropoxide precursor resulted with greater % ε-WO_3 content compared to the Cr-doped WO_3 nanopowders. The pure WO_3 particles showed a greater phase stability upon calcination compared to those reported in the literature. The results discussed here provides the possibility that the material obtained may be used to develop the next generation of hand-held breathalyzer for breath acetone monitoring. With a band gap energy of 2.73eV, the pure WO_3 compounds can also be applied as visible light photocatalysts.

References

1. Sawada, S., *Microscopic and X-Ray Studies on Tungsten Oxide (WO3).* Journal of the Physical Society of Japan, 1956. **11**(12): p. 1246-1252.

2. Gouma, P.I. and K. Kalyanasundaram, *Novel synthesis of hexagonal WO3 nanostructures.* Journal of Materials Science, 2015. **50**(9): p. 3517-3522.

3. Detraux, F., P. Ghosez, and X. Gonze, *Anomalously large Born effective charges in cubic WO_3.* PHYSICAL REVIEW B, 1997. **56**(3).

4. Woodward, P.M., A.W. Sleight, and T. Vogt, *Ferroelectric Tungsten Trioxide.* Journal of Solid State Chemistry, 1997. **131**(1): p. 9-17.

5. Ekhard, K.H.S., et al., *Crystal structure and paramagnetic behaviour of epsilon WO_{3-x}.* Journal of Physics: Condensed Matter, 1997. **9**(31).

6. Wang, L., et al., *Ferroelectric WO3 Nanoparticles for Acetone Selective Detection.* Chemistry of Materials, 2008. **20**(15): p. 4794-4796.

7. Lappalainen, J., et al., *PLD-grown WO3 nanostructures with epsilon-phase for gas sensor applications*, in *Eurosensors Xxiv Conference*, B. Jakoby and M.J. Vellekoop, Editors. 2010. p. 343-346.

8. Bathe, S.R. and P.S. Patil, *Titanium doping effects in electrochromic pulsed spray pyrolysed WO3 thin films.* Solid State Ionics, 2008. **179**(9-10): p. 314-323.

9. Yan, A., et al., *Synthesis, formation mechanism and illuminated sensing properties of 3D WO3 nanowall.* Journal of Alloys and Compounds, 2010. **495**: p. 88-92.

10. Patil, P.S., *Versatility of chemical spray pyrolysis technique.* Materials Chemistry and Physics, 1999. **59**(3): p. 185-198.

11. Righettoni, M., A. Tricoli, and S.E. Pratsinis, *Thermally Stable, Silica-Doped epsilon-WO3 for Sensing of Acetone in the Human Breath.* Chemistry of Materials, 2010. **22**(10): p. 3152-3157.

12. Teoh, W.Y., R. Amal, and L. Mädler, *Flame spray pyrolysis: An enabling technology for nanoparticles design and fabrication.* Nanoscale, 2010. **2**: p. 1324-1347.

13. Wang, L., *Tailored synthesis and characterization of selective metabolite-detecting nanoprobes for handheld breath analysis*, in *Materials Science & Engineering*. 2008, Stony Brook University: Proquest LLC.

14. Socrates, G., *Infrared and Raman Characteristic Group Frequencies: Tables and Charts*. #rd ed. 2004: Wiley.

15. Richter, H., et al., *Absorption properties of synthetic Cr-doped spinels in the UV, visible and infrared range and their astronomical implications.* Mineralogy and Petrology, 2005. **85**(1): p. 53-65.

16. Lai, C.W., *WO3 Nanoplates Film: Formation and Photocatalytic Oxidation Studies.* Journal of Nanomaterials, 2015. **2015**: p. 7.

17. Purwanto, A., W.-N. Wang, and K. Okuyama, *Flame Spray Pyrolysis*, in *Handbook of Atomization and Sprays: Theory and Applications*, N. Ashgriz, Editor. 2011, Springer US: Boston, MA. p. 869-879.

18. Strobel, R. and S.E. Pratsinis, *Flame aerosol synthesis of smart nanostructured materials.* Journal of Materials Chemistry, 2007. **17**(45): p. 4743-4756.

19. Sood, S., *Polymorphism control in nanostructured metal oxides*, in *materials science and engineering*. 2014, stony brook university: Proqueest llc.

20. Pokhrel, S., et al., *Growth of Ultrafine Single Crystalline WO3 Nanoparticles Using Flame Spray Pyrolysis.* Crystal Growth & Design, 2010. **10**(2): p. 632-639.

21. Bianchi, S., et al., *The reactivity of tungsten hexachloride with tetrahydrofuran and 2-methoxyethanol.* Polyhedron, 2016. **117**: p. 769-776.

Chapter 5: Flame spray synthesis of $VOPO_4$ Polymorphs

5.1 Introduction

Vanadium phosphates ($VOPO_4$) have gained some noted interest from researchers as functional oxide materials due to their outstanding catalytic and electronic properties. Among their various applications, they have been studied as catalysts for hydrocarbons[1-4], where the +5 valence state of Vanadium is important in extraction of hydrogen atom from alkanes[5]. Apart from their applications in catalysis, Vanadium Phosphates also find applications as electrode materials in Lithium-ion batteries [6-8] and Sodium-ion batteries [9, 10], pseudocapacitors [11, 12] and sensors [13, 14]. The variety of applications of $VOPO_4$ can be related to the various polymorphs exhibited by the compound.

There are seven reported polymorphs for $VOPO_4$. Among these polymorphs, four exhibit tetragonal structure (α_1, α_2, δ and ω), two exhibit orthorhombic structure (β and γ) and one monoclinic structure (ε) [15]. Among these polymorphs, β-$VOPO_4$ has the lowest energy configuration. However, these polymorphs have been synthesized using various routes, although, due to close relation in the structures of all the polymorphs and their low energy difference, obtaining a single phase is almost impossible[15]. The various techniques applied for synthesis of $VOPO_4$ compounds are solvothermal synthesis [16, 17] solid state interactions [18, 19], and electrochemical synthesis[20]. However, all these methods result either in big particle size and aren't commercially feasible due to their lengthy processing times.

In this chapter, we investigate the FSP-based synthesis of $VOPO_4$ powders. The methodology used to produce particles at a laboratory based FSP setup, can be transferred to a foundry for the bulk synthesis of the material. Aeroxide P25 Titania, from Evonik industries, provides evidence for the scalable oxide synthesis via flame aerosol technique. Apart from the commercial aspect, the advantage of flame spray synthesis lies in ease of fabrication, elimination for the use of expensive raw materials, uniform size distribution and high purity of product. Flame synthesized particles have small particle sizes and high surface area: volume ratios, which is desirable for catalysis and electrochemical equations.

For this study, aqueous solutions are used with two different organic components as precursors for FSP process. Ammonium vandate and ammonium dihydrogen phosphate were chosen as the precursor solutes due to close proximity of their melting temperatures. The solutes were dissolved in water to obtain homogenous mixture. Addition of sucrose/DMF is to generate a

self-sustainable process. The obtained powders are then characterized using XRD, TGA-DTA, SEM, TEM with SAED, and FTIR for their crystallographic phases, morphologies, chemical compositions and thermal stability.

5.2 Experimental methods

5.2.1 FSP $VOPO_4$ using aqueous solution with sucrose

Precursor solution was prepared using ammonium vandate (1.17g) and ammonium dihydrogen phosphate (1.15g). The salts were mixed in 100 ml deionized water bringing the concentration of the solution to 0.1M. 1.5g of sucrose was added to the solution as an organic component. The addition of organic component was to produce a self-sustaining flame during the FSP process. The solution was stirred at 600 RPM and maintained at 60ºC using a heated magnetic stirrer until a homogenous mixture was obtained. The solution was aged for a day and then fed into the FSP system (Tethis NPS 10). For fsp process, the flame was generated using methane and oxygen; 1.5slm methane and 3.0slm oxygen was used; 5slm oxygen was used as dispersion gas, the solution feed rate was 5ml. The particles were collected on a glass fiber filter. The powders were calcined at 500 ºC for 8 hours.

5.2.2 FSP $VOPO_4$ using aqueous solution with DMF

Precursor solution was prepared using ammonium vandate (1.17g) and ammonium dihydrogen phosphate (1.15g). The salts were mixed in 80 ml deionized water bringing the concentration of the solution to 0.1M. The solution was stirred at 600 RPM and maintained at 60ºC using a heated magnetic stirrer until a homogenous mixture was obtained. The solution was then aged for a day. Upon aging, 20ml DMF was added to the solution and it was then fed into the FSP system (Tethis NPS 10). For fsp process, the flame was generated using methane and oxygen; 1.5slm methane and 3.0slm oxygen was used; 5slm oxygen was used as dispersion gas, the solution feed rate was 5ml. The particles were collected on a glass fiber filter. The powders were calcined at 500 ºC for 8 hours.

5.2.3 Material Characterization

The powders were characterized using Scanning Electron Microscopy (SEM, LEO 1550), Transmission Electron Microscopy (TEM, JEOL 1400) and selected area electron diffraction was carried out on both as synthesized and calcined samples. Thermogravimetric analysis (TGA, Perkin Elmer Diamond) was conducted on the as-synthesized samples. The particles, both as-

synthesized and calcined, were also characterized using XRD (Rigaku Miniflex II) and FTIR (Thermo Scientific Nicolet 6700).

5.3 Results

5.3.1 X-Ray Characterization

Figure 6.1 shows the XRD characterization of FSP synthesized powders. The as-synthesized particles were highly amorphous in nature. Although some crystallinity was obtained. The powders synthesized using a sucrose based solution, matched with JCPDS 36-0054 for Ammonium Vanadyl Hydrogen phosphate hydrate ($NH_4VOVO_2(HPO_4)_2.1.5H_2O$) and are denoted by a letter A in figure 5.1a . Figure 5.1a also shows the pattern for powders synthesized using a DMF based solution. The pattern showed a mixed system and matched with JCPDS 36-0054 for Ammonium Vanadyl Hydrogen phosphate hydrate(denoted by A) and JCPDS 34-1247 for tetragonal $VOPO_4$ system(L→R denoted by α, 200 and 301 planes). The tetragonal $VOPO_4$ system was identified to be α_{II}-$VOPO_4$ based on the lattice parameters[21].

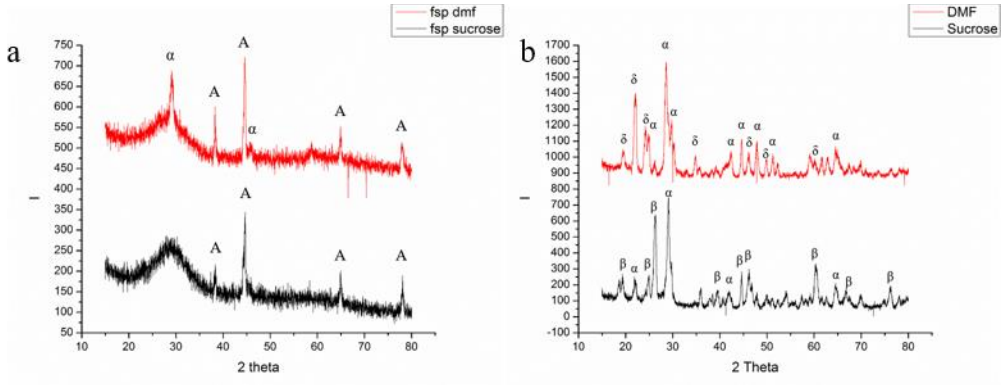

Figure 5-1: Results of XRD analysis of (a) as-synthesized and (b) calcined powders (A: Ammonium Vanadyl Hydrogen phosphate hydrate ($NH_4VOVO_2(HPO_4)_2.1.5H_2O$), α: α-$VOPO_4$, β: β- $VOPO_4$, δ: δ- $VOPO_4$)

Figure 5.1b shows the XRD characterization of calcined FSP synthesized powders. Both the powders resulted in mixed phases. In case calcined powders for sucrose based solutions, the peaks from XRD pattern were found to be orthorhombic β-$VOPO_4$ (JCPDS 71-0859) and tetragonal α_{II}-$VOPO_4$ (JCPDS 34-1247). The peaks for β-$VOPO_4$ are denoted by β (L→R: 011,

002, 201, 221, 031, 400, and 040 planes) and the peaks for peaks for α_{II}-$VOPO_4$ are denoted by α (L→R: 101, 200, 220, and 132 planes). For calcined powders for DMF based solutions, the peaks from XRD pattern were found to be tetragonal δ-$VOPO_4$ (JCPDS 47-0951) and tetragonal α_{II}-$VOPO_4$ (JCPDS 34-1247). The peaks for δ-$VOPO_4$ are denoted by δ (L→R: 002, 111, 012, 022, 031, 214, and 106 planes) and the peaks for peaks for α_{II}-$VOPO_4$ are denoted by α (L→R: 101, 111, 200, 220, 112, 301, 311, and 420 planes).

The relative phase content was calculated using peak intensity ratios for all the samples. Quantitative analysis for crystallite size determination was conducted using Scherrer's formula. Table 5.1 lists the phase content and their crystallite sizes.

Table 5-1 Phase content and crystallite sizes for FSP $VOPO_4$

Sample	Polymorph	% phase	Crystallite size (nm)
Suc- assynthesized	$NH_4VOVO_2(HPO_4)_2.1.5H_2O$	100	149.8
DMF-assynthesized	$NH_4VOVO_2(HPO_4)_2.1.5H_2O$	52.4	32.6
	α_{II}-$VOPO_4$	47.6	19.9
Suc- calcined	β-$VOPO_4$	45.7	26.3
	α_{II}-$VOPO_4$	54.3	24.6
DMF- calcined	δ-$VOPO_4$	42.43	24.3
	α_{II}-$VOPO_4$	57.57	21.7

5.3.2 Thermal Analysis

TGA-DTA was conducted on as-synthesized samples in the range of RT-550°C under oxygen atmosphere. Figure 5.2 shows the plot for (a) powders synthesized using sucrose based solution and (b) powders synthesized using DMF based solution.

Powders synthesized using sucrose based solution show a drop in weight with increase in temperature. The weight loss can be associated with the release of ammonia and water by

decomposition of $NH_4VOVO_2(HPO_4)_2.1.5H_2O$ and formation of $VOPO_4$ structures. The DTA signals show two exothermic changes at 260°C and 540°C, these changes can be associated with formation of β-$VOPO_4$ and α_{II}-$VOPO_4$.

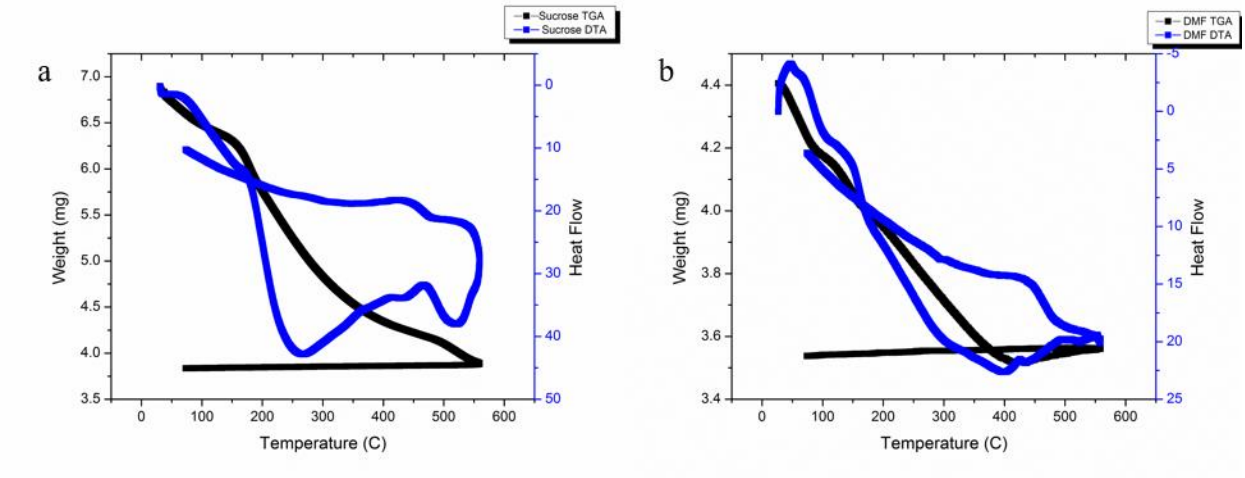

Figure 5-2: TGA-DTA analysis for (a) FSP powders with sucrose (b) FSP powders with DMF

Powders synthesized using DMF based solution show a drop in weight with increase in temperature. Similar to the sucrose based solutions, the weight loss can be associated with the release of ammonia and water by decomposition of $NH_4VOVO_2(HPO_4)_2.1.5H_2O$ and formation of $VOPO_4$ structures. The weight drop stops at 420°C and a slight spike in weight is noticed between 420-550°C regions. The DTA signals shows an exothermic change 420°C. Since the as-synthesized particles were a mixture of Vanadyl Hydrogen phosphate hydrate & α_{II}-$VOPO_4$, which resulted in formation α_{II}-$VOPO_4$ and δ-$VOPO_4$. The exothermic reaction at 420°C can be associated to the formation of δ-$VOPO_4$.

5.3.3 Fourier Transform Infrared Spectroscopy

FTIR was conducted on all the samples in the range of 500-4000 cm^{-1} region. The signal received below 500 had too much noise. Figure 6.3 shows the FTIR spectra for (a) powders obtained sucrose based solution (as-synthesized and calcined) and (b) powders obtained DMF based solution (as-synthesized and calcined).

For the as-synthesized particles from sucrose based solution, the peaks were obtained at 569, 1040, 1424, 1654 and a broad peak in 3200 cm^{-1} region. The peak at 1424 cm^{-1} and the broad peak at 3200 cm^{-1} correspond to N-H bending vibrations[22]. The peak at 1654 cm^{-1} indicated inclusion of water. The strong peak at 1040 cm^{-1} belongs to P-O[23] vibrations and the peak at 569

cm^{-1} can be associated to V-O-V rotational vibrations[24]. Upon calcination the FTIR spectra for the calcined powders revealed peaks at 559, 673, 903, 949, shoulder at 1080, 1614 and a broad peak at 3344 cm-1. The broad peak at 3344 cm^{-1} and the peak at 1614 cm^{-1} correspond to N-H bending vibrations[22] and signify presence of undecomposed ammonia. The V-O-V rotational vibrations observed 559 cm^{-1} is observed at 569 cm^{-1} in the calcined sample. Similarly, the peak for P-O vibrations observed at 1040 cm^{-1} is observed at 1080 cm^{-1}. New peaks were observed at 673, 903 and 949cm^{-1}. The peak at 673 can be associated with metaphosphate[22]. The peaks in 903 and 949 cm^{-1} region belong to the V=O vibrations[25]. The different peak position signify a shift in the V=O bonds, the shift can be associated with the presence of two phases.

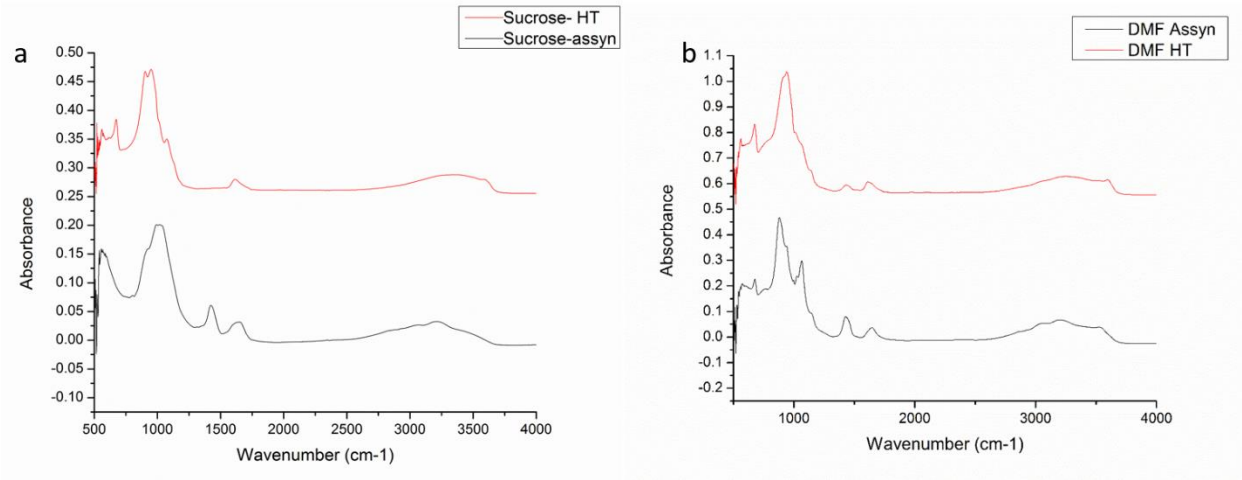

Figure 5-3: FTIR images for (a) as-synthesized and calcined FSP DMF powders (b) as synthesized and calcined FSP sucrose powders

For the as-synthesized particles from DMF based solution, the peaks were obtained at 566, 676, 879, 941 1064, 1426, 1644 and a broad peak in 3200 cm^{-1} region. The peak at 1426 cm^{-1} and the broad peak at 3200 cm^{-1} correspond to N-H bending vibrations as was the as-synthesized particles from sucrose solution. Similarly the peak at 1644 cm^{-1} indicated inclusion of water. The peak at 1040 cm^{-1} belongs to P-O vibrations, the peak at 941 belongs to V=O vibrations and the peak at 566 cm^{-1} can be associated to V-O-V rotational vibrations. The peak observed at 873 cm^{-1} correspond to orthovandates[22]. Upon calcination the FTIR spectra for the calcined powders revealed peaks at 560, 674, 939, shoulder at 1020, 1428, 1612 and a broad peak at 3254 cm-1. The broad peak at 3254 cm^{-1} and the peak at 1612 cm^{-1} correspond to N-H bending vibrations[22] and signify slight presence of undecomposed ammonia. The V-O-V rotational vibrations observed at 566 cm^{-1} is observed at 560 cm^{-1} in the calcined sample. Similarly, the peak for P-O vibrations

observed at 1040 cm^{-1} is observed at 1020 cm^{-1}, the peak for V=O vibrations observed at 941 cm^{-1} shifts to 939 cm^{-1}, the metaphosphate peak shifts from 676 cm^{-1} to 674 cm^{-1}. A slight shift in peak positions and absence of new peaks indicate that no major change occurred in the structure upon heat treatment.

5.3.4 Scanning Electron Microscopy

I. As-synthesized Samples

The as-synthesized particles were characterized by SEM and the particle morphology was analyzed. Figure 6.4 show the SEM images for as-synthesized particles. For the particles synthesized using sucrose based precursor (figure 6.4 a, b, and c), the particle morphology was in the form of sphere. Two different sizes were obtained, the large spheres were hollow and in the size range of 2-10μm. From high resolution imaging (figure 6.4c). The thickness of these was found to be in the range of 100-150nm. The smaller spheres were solid and in the size range of 200-300nm. For the particles synthesized using DMF based precursor (figure 6.4 d,e, and f), the particles were found to be spheres. Similar to the as-synthesized particles from sucrose based solutions, two different size range were noticed. The large spheres were found to be 2-5 μm with a thickness of 50-80nm. Smaller sized particles were obtained in the range of 50-200nm.

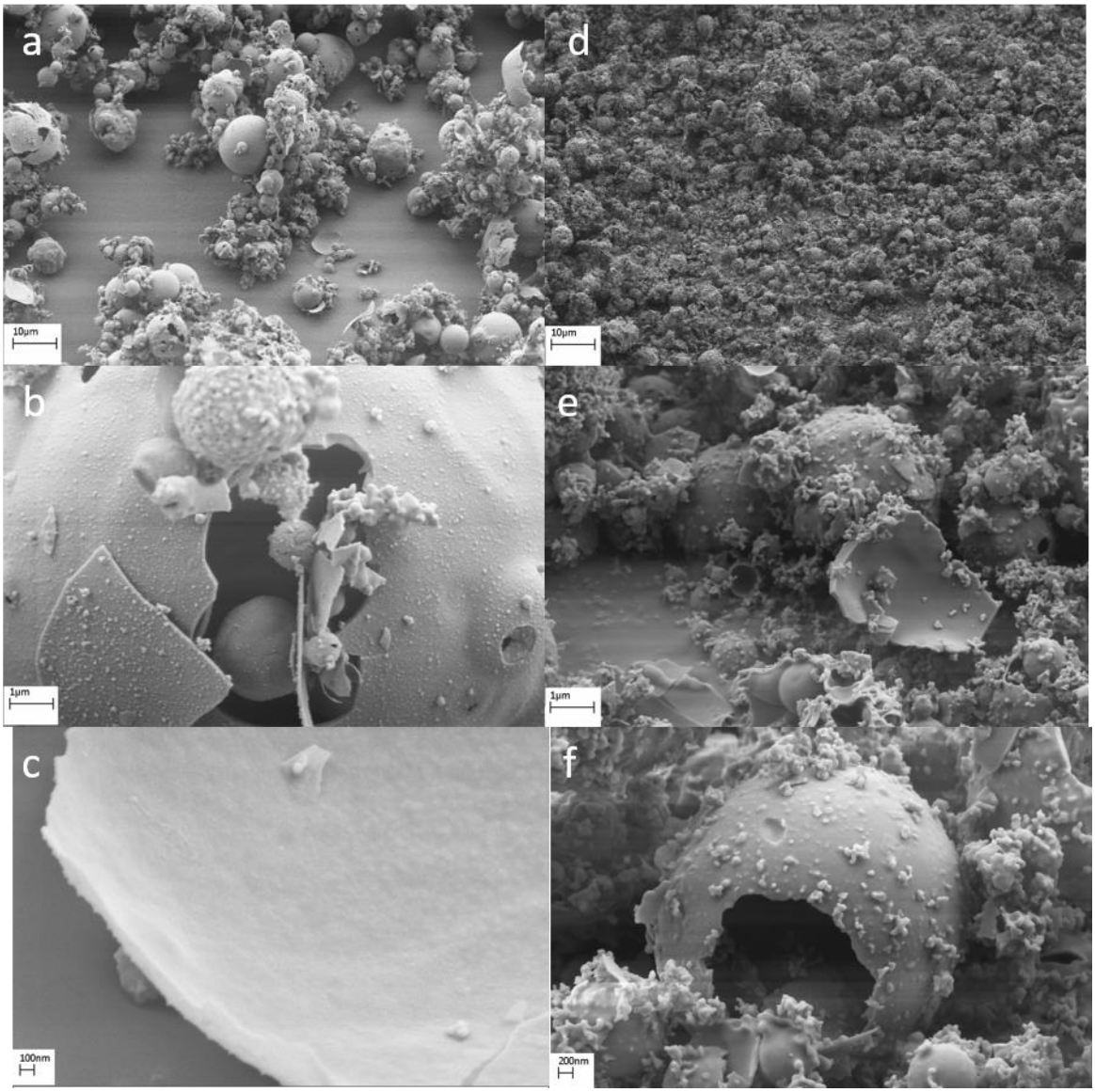

Figure 5-4: Scanning electron microscopy images for as-synthesized particles from (a,b,c) sucrose based solutions (d,e,f,) DMF based solutions

II. Calcined Samples

The calcined particles were characterized by SEM and the effect of heat-treatment on particle morphology was analyzed. Figure 5.5 show the SEM images for calcined particles. The particle morphology obtained for calcined particles from sucrose solution (fig.5.5 a,b,c) was similar to that of as-synthesized samples. The surface of hollow particles was analyzed using a higher resolution and revealed formation of smaller grains on the surface as opposed to an eggshell type of structure

for as-synthesized particles. High resolution imaging (fig. 5.5c) revealed the grain sizes to be in order of 80-150nm. The particle morphology obtained for calcined particles from DMF solution (fig.5.5 d,e,f) was similar to that of as-synthesized samples. However, the grains observed on the surface were found to represent a lamellar structure (fig. 5.5f).

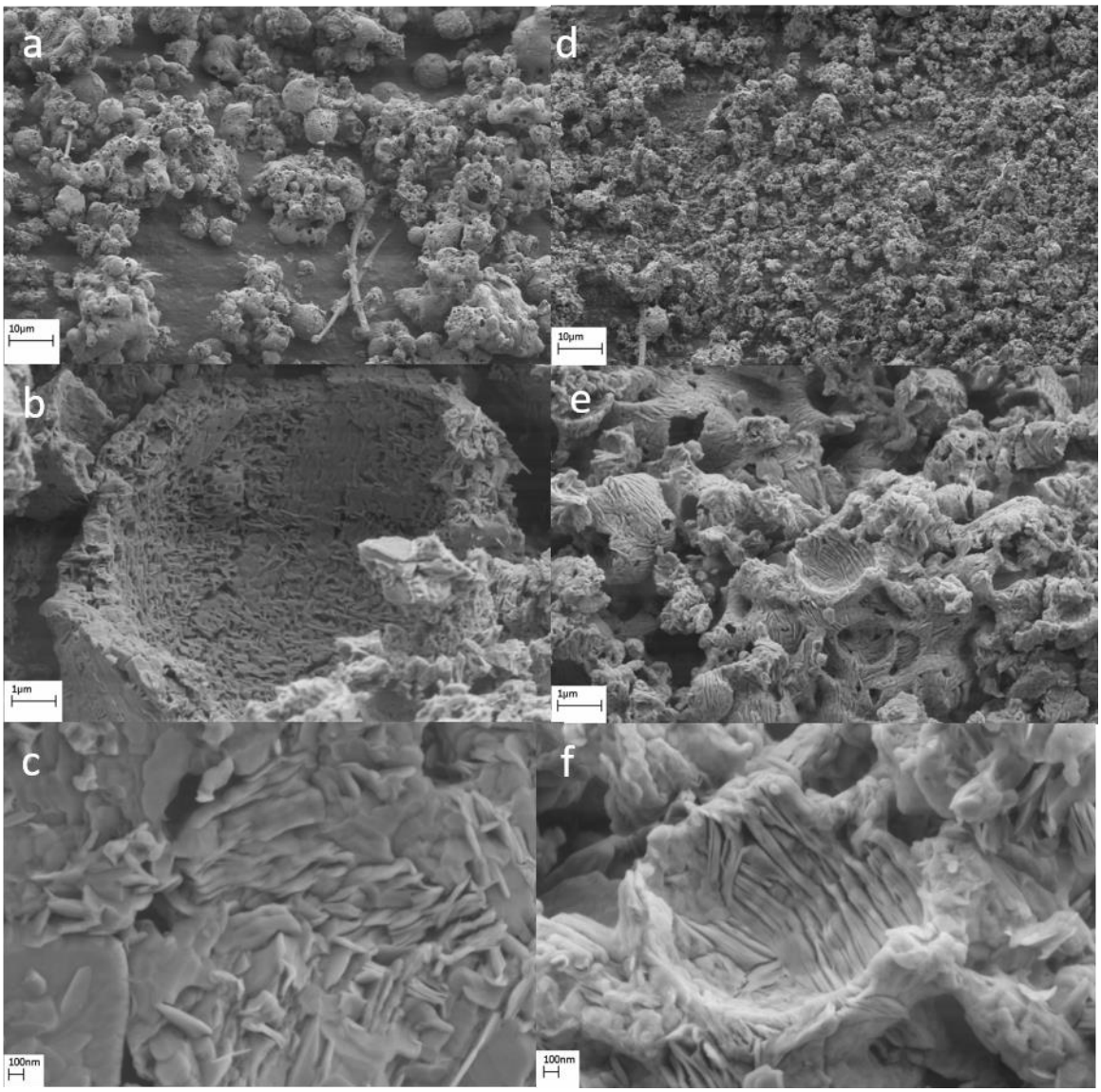

Figure 5-5: Scanning electron microscopy images for calcined particles from (a,b,c) sucrose based solutions (d,e,f,) DMF based solutions

5.3.5 Transmission electron microscopy

I. As-synthesized particles

Transmission electron microscopy with selected area electron diffraction was conducted on all samples. The TEM imaging of as-synthesized particles from sucrose based solution showed thick spherical particles (fig. 5.6 a,b). The particles over the size of 1µm were hollow. SAED pattern didn't result in any rings (fig. 5.6c), indicating the particles were amorphous. In case of as-synthesized particles from DMF based solution solid spheres in the range of 100-200nm were noticed. No micron sized particles were noticed, however, thin walled shell structures were observed; indicating disintegration of hollow spheres that were noticed in SEM. SAED pattern on solid spheres resulted in rings that matched with JCPDS 34-1247 α_{II}-$VOPO_4$ (fig. 5.6f; 111 and 220 planes).

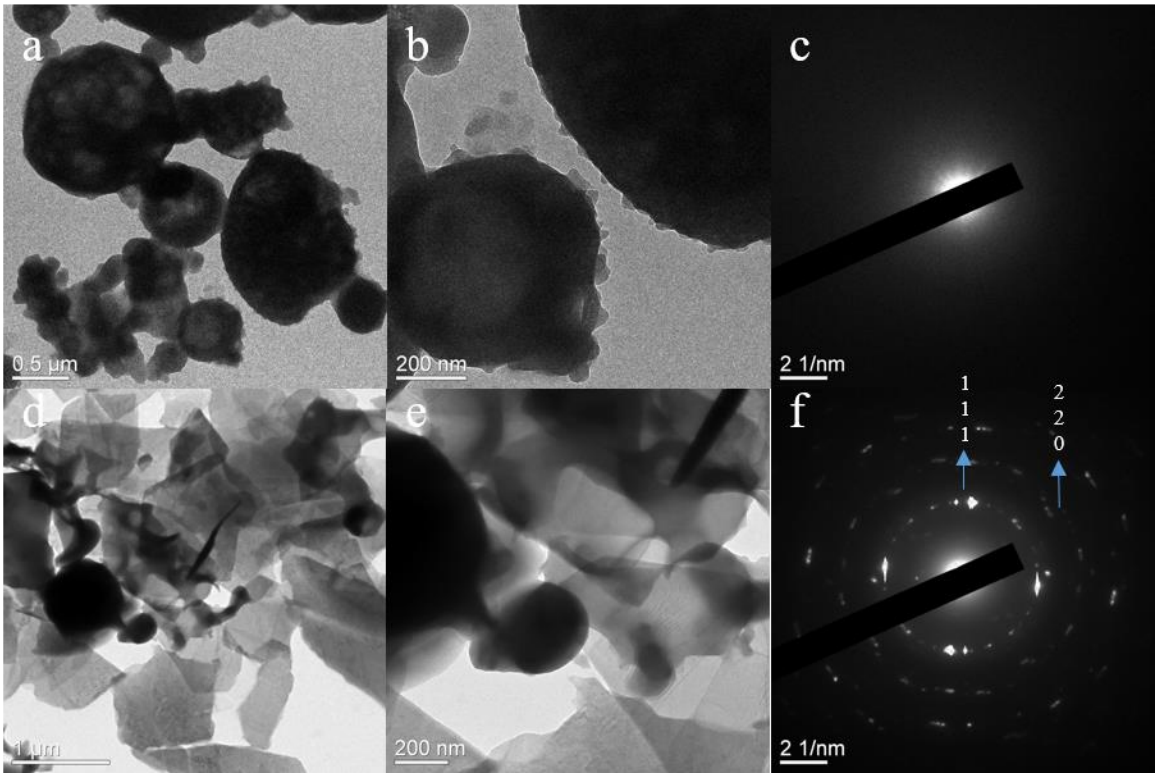

Figure 5-6: TEM images and corresponding SAED pattern for as-synthesized particles from (a,b,c) sucrose based solutions (d,e,f,) DMF based solutions

II. Calcined particles

The TEM imaging of calcined from sucrose based solution showed thin spherical disk like particles (fig. 5.7 a,b). The particle sizes for these disks ranged in the range of 40-300nm. SAED pattern on the disks resulted in rings that matched with JCPDS 34-1247 α_{II}-$VOPO_4$ (fig. 5.7c; 200

and 112 planes). No rings were found representing β-$VOPO_4$, however, the imaging showed growth of lathes on the edges of the disks which might be associated to β-$VOPO_4$. In case of calcined particles from DMF based solution the morphology was in form of rectangular nanosheets. The size of these sheets were in the range of 50-500nm in length. The particle sizes for these disks ranged in the range of 40-300nm. SAED pattern on the disks resulted in rings that matched with JCPDS 34-1247 α_{II}-$VOPO_4$ (fig. 5.7f; 200 and 112 planes).

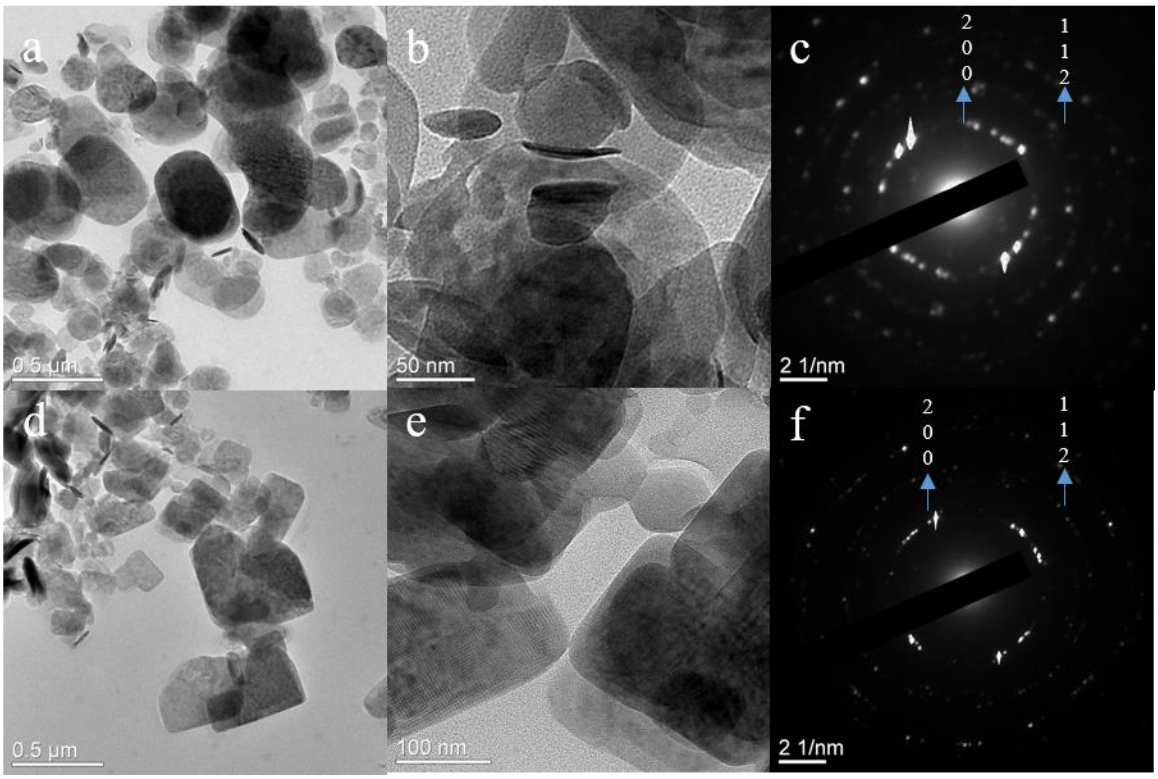

Figure 5-7: TEM images and corresponding SAED pattern for calcined particles from (a,b,c) sucrose based solutions (d,e,f,) DMF based solutions

5.4 Discussion

The resultant powders from flame spray pyrolysis resulted contained a large amount of $NH_4VOVO_2(HPO_4)_2.1.5H_2O$. The formation the compound can be attributed to the reaction between ammonium vandate and ammonium dihydrogen phosphate in aqueous medium. The particles formed from sucrose based solutions were in micron range and hollow, the formation of such particles these large particles were a result of precursors with low enthalpies coupled with high melting/decomposition points[26]. Moreover, due to the usage of an aqueous solution, the

temperature of the flame is significantly reduced for complete decomposition of particles. The addition of sucrose although helped as few submicron sized particles were noticed, which is the size range for aqueous based precursors[27]. The particle size were further reduced with the addition of DMF. The addition of DMF possibly resulted in formation two systems during atomization of precursors, one in aqueous medium and the other in organic medium. The formation secondary organic system led to temperature gradient high enough for the formation of α_{II}-$VOPO_4$. The process map for the formation of powders via fsp is shown in fig. 5.8.

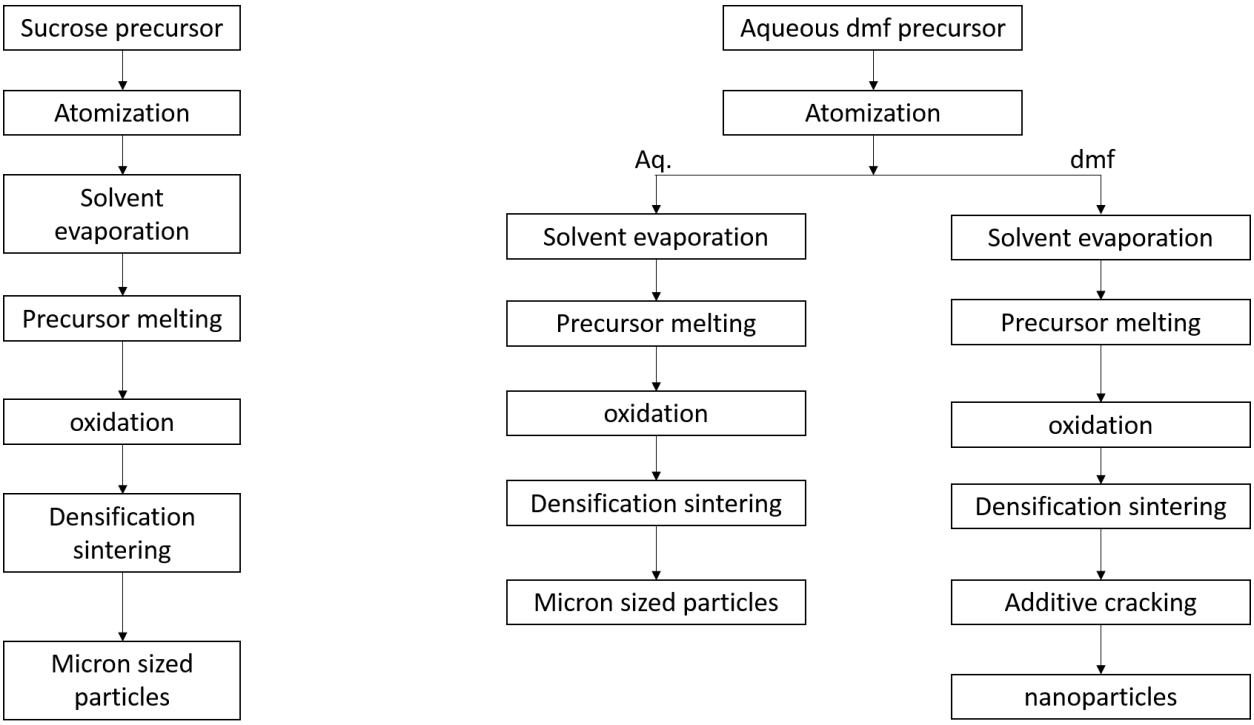

Figure 5-8: Process map for fsp synthesis of powders

Upon calcination of as-synthesized products, the resultant powders were a mixture of α_{II}-$VOPO_4$ & β-$VOPO_4$ and α_{II}-$VOPO_4$ and δ-VOPO4. According to DFT calculations, the β-$VOPO_4$ is the most stable configuration for $VOPO_4$[21, 28]. However, according to DFT calculations, there is only a small difference in energy between $VOPO_4$. Which suggest that temperature has little effect on phase transformation of $VOPO_4$ polymorphs. Although it has been reported that a slight change in synthesis conditions[29]. The primary difference in $VOPO_4$ structures occur in the form of V-O bond length, which in turn lead to different crystal structures and polymorphs.

The mixed polymorphs obtained here can be associated with the precursor, where, the formation of $NH_4VOVO_2(HPO_4)_2.1.5H_2O$ leads to multiple polymorphs. The precursor salt contains two valence states for VO in the form of $V(IV)O^{2-}$ and $V(V)O_2^-$. The Vanadium oxide with +5 valence state exhibits an orthovandate structure. Based on the results obtained, the orthovandate structure exhibits similar V-O bond length to α_{II}-$VOPO_4$. Hence, formation of α_{II}-$VOPO_4$ was observed in all the samples. The formation of β and δ polymorphs, are a result of the transformation of the +4 valence state VO^{2-} into a +5 valence state in an oxidative atmosphere. The oxidation leads to formation of V-O bond the length of which determines the formation of either β or δ polymorphs. The oxidation was noticed during the TGA analysis of particles synthesized with DMF precursor, where a slight increase in weight was observed at 420°C.

In case of powders synthesized using sucrose solution, the VO^{2-} transforms into the most stable state and thereby leads to the formation of β-$VOPO_4$. The synthesis of the δ polymorph has been reported earlier from the thermal oxidation of a +4 valency Vanadium hydrogen phosphate compound[30]. The compound was held at 400°C for 7 days for successful transformation into δ polymorphs. In this study, the lower particle size led to faster transformations.

5.5 Conclusion

We have successfully demonstrated the formation of $VOPO_4$ polymorphs with FSP process. The precursor used favors the formation of α_{II}-$VOPO_4$. Secondary phases are formed due to oxidation of lower valence state vanadium compound in the precursor. Particle size plays an important role in forming a polymorph upon oxidation of lower valence state compound. Smaller particle size favor formation of δ polymorph, whereas, large particle sizes tend to form β polymorph. Based on these results, other precursor compounds can be investigated towards formation of other polymorphs for $VOPO_4$.

References

1. S. Albonetti, F. Cavani, F. Trifiro, P. Venturoli, G. Calestani, M. L. Granados and J. L. G. Fierro, "A comparison of the reactivity of "nonequilibrated" and "equilibrated" V-P-O catalysts: Structural evolution, surface characterization, and reactivity in the selective oxidation of n-butane and n-pentane," *Journal of Catalysis*, vol. 160, no. 1, pp. 52-64, 1996.

2. M. Conte, G. Budroni, J. K. Bartley, S. H. Taylor, A. F. Carley, A. Schmidt, D. M. Murphy, F. Girgsdies, T. Ressler, R. Schlogl and G. J. Hutchings, "Chemically induced fast solid-state

transitions of omega-VOPO4 in vanadium phosphate catalysts," *Science*, vol. 313, no. 5791, pp. 1270-1273, 2006.

3. G. W. Coulston, S. R. Bare, H. Kung, K. Birkeland, G. K. Bethke, R. Harlow, N. Herron and P. L. Lee, "The kinetic significance of V5+ in n-butane oxidation catalyzed by vanadium phosphates," *Science*, vol. 275, no. 5297, pp. 191-193, 1997.

4. V. V. Guliants, J. B. Benziger, S. Sundaresan, I. E. Wachs, J. M. Jehng and J. E. Roberts, "The effect of the phase composition of model VPO catalysts for partial oxidation of n-butane," *Catalysis Today*, vol. 28, no. 4, pp. 275-295, 1996.

5. G. J. Hutchings, C. J. Kiely, M. T. Sananes-Schulz, A. Burrows and J. C. Volta, "Comments on the nature of the active site of vanadium phosphate catalysts for butane oxidation," *Catalysis Today*, vol. 40, no. 2-3, pp. 273-286, 1998.

6. M. S. Whittingham, Y. N. Song, S. Lutta, P. Y. Zavalij and N. A. Chernova, "Some transition metal (oxy)phosphates and vanadium oxides for lithium batteries," *Journal of Materials Chemistry*, vol. 15, no. 33, pp. 3362-3379, 2005.

7. J. Gaubicher, T. Le Mercier, Y. Chabre, J. Angenault and M. Quarton, "Li/beta-VOPO4: A new 4 V system for lithium batteries," *Journal of the Electrochemical Society*, vol. 146, no. 12, pp. 4375-4379, 1999.

8. T. A. Kerr, J. Gaubicher and L. F. Nazar, "Highly reversible Li insertion at 4 V in epsilon-VOPO4/alpha-LiVOPO4 cathodes," *Electrochemical and Solid State Letters*, vol. 3, no. 10, pp. 460-462, 2000.

9. G. He, A. Huq, W. H. Kan and A. Manthiram, "beta-NaVOPO4 Obtained by a Low-Temperature Synthesis Process: A New 3.3 V Cathode for Sodium-Ion Batteries," *Chemistry of Materials*, vol. 28, no. 5, pp. 1503-1512, 2016.

10. G. He, W. H. Kan and A. Manthiram, "A 3.4 V Layered VOPO4 Cathode for Na-Ion Batteries," *Chemistry of Materials*, vol. 28, no. 2, pp. 682-688, 2016.

11. K. H. Lee, Y. W. Lee, S. W. Lee, J. S. Ha, S. S. Lee and J. G. Son, "Ice-templated Self-assembly of VOPO4-Graphene Nanocomposites for Vertically Porous 3D Supercapacitor Electrodes," *Scientific Reports*, vol. 5, 2015.

12. C. Z. Wu, X. L. Lu, L. L. Peng, K. Xu, X. Peng, J. L. Huang, G. H. Yu and Y. Xie, "Two-dimensional vanadyl phosphate ultrathin nanosheets for high energy density and flexible pseudocapacitors," *Nature Communications*, vol. 4, 2013.

13. A. Khan, A. A. P. Khan, M. M. Rahman and A. M. Asiri, "High performance polyaniline/vanadyl phosphate (PANI-VOPO4) nano composite sheets prepared by exfoliation/intercalation method for sensing applications," *European Polymer Journal*, vol. 75, pp. 388-398, 2016.
14. G. C. Li, Y. M. Li, Y. Li, H. R. Peng and K. Z. Chen, "Polyaniline Nanorings and Flat Hollow Capsules Synthesized by in Situ Sacrificial Oxidative Templates," *Macromolecules*, vol. 44, no. 23, pp. 9319-9323, 2011.
15. N. Dupre, G. Wallez, J. Gaubicher and M. Quarton, "Phase transition induced by lithium insertion in αI- and αII-VOPO4," *Journal of Solid State Chemistry*, vol. 177, pp. 2896-2902, 2004.
16. C. J. Allen, Q. Y. Jia, C. N. Chinnasamy, S. Mukerjee and K. M. Abraham, "Synthesis, Structure and Electrochemistry of Lithium Vanadium Phosphate Cathode Materials," *Journal of the Electrochemical Society*, vol. 158, no. 12, pp. A1250-A1259, 2011.
17. A. Rownaghi, Y. H. Taufiq-Yap and F. Rezaei, "Solvothermal synthesis of vanadium phosphate catalysts for n-butane oxidation," *Chemical Engineering Journal*, vol. 155, no. 1-2, pp. 514-522, 2009.
18. J. K. Bartley, C. J. Kiely, R. P. K. Wells and G. J. Hutchings, "Vanadium(V) phosphate prepared using solvent-free method," *Catalysis Letters*, vol. 72, no. 1-2, pp. 99-105, 2001.
19. V. Sydorchuk, S. Khalameida, V. Zazhigalov, J. Skubiszewska-Zieba and R. Leboda, "Solid-state interactions of vanadium and phosphorus oxides in the closed systems," *Journal of Thermal Analysis and Calorimetry*, vol. 100, no. 1, pp. 11-17, 2010.
20. Y. Song, P. Y. Zavalij and M. S. Whittingham, "ε-VOPO4: Electrochemical Synthesis and Enhanced Cathode Behavior," *Journal of electrochemical society*, vol. 152, no. 4, pp. A721-A728, 2005.
21. C. Ling, R. Zhang and F. Mizuno, "Phase stability and its impact on the electrochemical performance of VOPO4 and LiVOPO4," *Journal of Materials Chemistry A*, vol. 2, no. 31, pp. 12330-12339, 2014.
22. G. Socrates, *Infrared and Raman Characteristic Group Frequencies: Tables and Charts*, Wiley, #rd edition 2004.

23. X. Jiao, D. Chen, W. Pang, R. Xu and Y. Yue, "Solvothermal synthesis and characterization of silica-pillared titanium phosphate," *Journal of Materials Chemistry*, vol. 8, no. 12, pp. 2831-2834, 1998.

24. M. Xue, H. Chen, H. Zhang, A. Auroux and J. Shen, "Preparation and characterization of V-Ag-O catalysts for the selective oxidation of toluene," *Applied Catalysis A: General*, vol. 379, no. 1–2, pp. 7-14, 2010.

25. R. Anumula, M. Nookaraju, K. Selvaraj, I. A. K. Reddy and V. Narayanan, "A novel vanadium n-propylamino phosphate catalyst: synthesis, characterization and applications," *Materials Research*, vol. 16, pp. 181-189, 2013.

26. L. e. a. Madler, "Flame Spray Pyrolysis: An enabling technology for nanoparticles design and fabrication," *NANOSCALE*, pp. 1324-1347, 2010.

27. A. Purwanto, W.-N. Wang and K. Okuyama, "Flame Spray Pyrolysis," in *Handbook of Atomization and Sprays: Theory and Applications*, N. Ashgriz, Ed., pp. 869-879, Springer US, Boston, MA, 2011.

28. W. Sun and J. Du, "Structural stability, electronic and thermodynamic properties of VOPO4 polymorphs from DFT+U calculations," *Computational Materials Science*, vol. 126, pp. 326-335, 2017.

29. N. Dupré, G. Wallez, J. Gaubicher and M. Quarton, "Phase transition induced by lithium insertion in αI- and αII-VOPO4," *Journal of Solid State Chemistry*, vol. 177, no. 8, pp. 2896-2902, 2004.

30. F. Girgsdies, M. Schneider, A. Brückner, T. Ressler and R. Schlögl, "The crystal structure of δ-VOPO4 and its relationship to ω-VOPO4," *Solid State Sciences*, vol. 11, no. 7, pp. 1258-1264, 2009.

Chapter 6: Processing of and phase selection in oxide ceramics through FSP

6.1 Scalable manufacturing through FSP

Large scale production of flame synthesized nanoparticles has been in existence for quite some time. Industries such as DuPont, Evonik (Degussa), Cabot, and Ishihara have been using flame aerosol technology to synthesize materials in millions of tons[1]. Some of the most notable industrial flame synthesized materials are Carbon blacks, SiO_2, TiO_2 and ZnO. These materials are then used for a variety of applications; TiO_2 finds application in paint industry as a pigment, fumed SiO_2 finds applications in cosmetics and food industries. The commercial synthesis of these materials uses VAFS[2], which require the need of volatile precursors for the synthesis of these materials. The advances in flame spray technology has negated the requirement for use of volatile precursors.

6.2 Factors affecting polymorph formation

Different polymorphs can exhibit different properties, therefore, synthesis of phase-pure materials often becomes a necessity. Currently, no real time techniques exist to determine the polymorphic formation of particle phase composition. However, the formation of polymorphs can be related to the high temperature synthesis and rapid quenching of the flame synthesized particles.

The limitation of polymorph formation lies within the thermodynamics and kinetics of phase formation, where, only polymorphs exhibiting lowest Gibbs free energy at high temperatures can be stabilized and obtained at room temperature with rapid quenching from their high temperature states. The rapid quenching from high temperature state has allowed formation of metastable polymorphs at room temperature, the examples include monoclinic $BaCO_3$ [3], Tetragonal ZrO_2 [4], ε-WO_3 [5], etc. to name a few. The formation of these metastable phases have been related to high flame temperature (~3000°C) and fast cooling rate, conditions that cannot be achieved through conventional solvothermal techniques.

Fast quenching can also result in formation of amorphous structures due to insufficient time for formation of crystalline structure through vapor phase. Such amorphous structures have been reported in case of $FePO_4$ [6] and were witnessed in this thesis during synthesis of MoO_3 with 0.05M concentration and $VOPO_4$. The amorphous materials then require additional treatment (calcination) to obtain crystalline form.

The factors that govern stabilization of a polymorph through FSP are temperature, particle size and residence time. These factors are interrelated and depend on the precursor and process parameters. The effect of these parameters is discussed below.

I. Particle size, Temperature gradient and Residence time:

The particles synthesized through FSP are either aggregates (sinter bonded) or agglomerates (physically bonded). The size of particles are affected by the synthesis temperature and concentration of the precursor. The temperature for synthesis can be controlled by the amount of fuel supplied to generate and operate the flame during synthesis. However, for FSP the precursor plays an important role in regulating the temperature. The combustion enthalpies of the solute and solvent govern the real operating temperature of the process.

Organic compounds are desirable for high temperature synthesis through FSP, the heat of combustion from organic compounds makes the process self-sustainable and leads to higher temperature gradient. The high temperature gradient lowers the residence time of the particles, as a shorter time is allowed for particles to aggregate from start of nucleation. The residence times can also be lowered by introducing a quenching gas, cold air o O_2 are usually used as quenching gases to shorten the residence time and aggregation rate in FSP[7, 8].

6.3 Precursor selection

The selection of liquid precursor is an important step in FSP particle synthesis. The selection of metallic precursor and solvent should be performed with keeping various factors in mind, such as, melting/decomposition temperatures, miscibility and chemical stability. These factors govern the overall particle formation in flame. Nitrates, actetates and acetylacetonates are the natural choices for FSP as they were economical and readily available. However, they do not always yield homogeneous morphology[9].

The low combustion enthalpies of precursors coupled with high melting points results in formation of in-homogenous particles[10]. However, this drawback can sometimes be remediated by processing parameters. Following is how the particle formation is affected by liquid precursor formulation.

Hollow particles are formed when the boiling point of solvent is less than the melting point of solute or if the metal precursor precipitates on the surface of solvent. These parameters can be overcome by providing sufficient heat to the precursor. For formation of homogenous particles the melting point of precursor solute should be lower than the boiling point of solvent.

6.4 Precursor preparation and effect on polymorphic behavior

I. MoO_3

For FSP synthesis of MoO_3, Ammonium molybdate tetrahydrate was selected as a precursor of its low melting point (90ºC), non-volatile nature and ready availability. The precursors were dissolved in water to obtain a homogenous solution. Since aqueous based solution lower the flame temperature, due to endothermic breakdown of water at high temperatures, an organic solvent was added to the precursor in order to generate a self-sustainable process. For low concentration of solute, a differential layer was noticed relating to the amount of organic solvent in the total solution. Combustion of this layer generated molybdenum particles signifying reaction between the solute particles distributed in water and DMF.

The particle phase and morphologies were greatly affected by the concentration of solute and percentage of organic solvent in the precursor. Large particle sizes were observed for solution with higher concentration of solute. For 0.68M solution the particles formed were micron sized and hollow, with a shell structure, as noticed via SEM. The formation of hollow micron particles were due to an inhomogeneous aqueous solution. The combustion enthalpy was significantly lowered due to presence of water in the solution, the lower combustion enthalpy prevented complete atomization of particles and led to the formation of an intermediate ammonium molybdenum oxide phase. The particles synthesized using a 0.05M solution also showed inclusion of some shell like hollow particles, based on the results from 0.68M solution it can be said that these particles were made of ammonium molybdenum oxide. Large amount of nano-sized particles were noticed via SEM analysis. These particles were amorphous in nature as confirmed by SEM. Since there was a higher amount of organic solvent in the 0.05M precursor solution, nano-sized particles were formed. The formation of these nano-sized particles can be attributed to complete vaporization of the solute in flame. However, the nano particles formed were amorphous in nature, the formation of amorphous particles is due to rapid quenching, which in turn doesn't allow the

particles to crystallize. The formation of β-MoO_3 has earlier been obtained through low temperature synthesis[11]. The stability of α-MoO_3 has been found to exist at temperatures as high as 800ºC[12]. The quenching of particles from a temperature higher than 800ºC is the cause for formation of amorphous particles.

The particles were stabilized in their crystalline form upon calcination at 500ºC, powders obtained from both 0.68M and 0.05M solutions changed into α-MoO_3. The phase was verified by XRD and SAED studies. The morphology of the calcined 0.68M particles were in the form of nanosheets. Such morphology was reported earlier for flame synthesized MoO_3 in doped form[13] and by our group for MoO_3 obtained after thermal degradation of electrospun mats[14] . The formation of the nanosheets is due to the low energy configuration for α-MoO_3 particles. The thermodynamically stable form consists of 2 similar chains of MoO_6 octahedra aligned in *ab* configuration[15]. Similar trend was observed upon calcination of as-synthesized particles from 0.05M solution. However, three different morphologies in the form of nanosheets and nanoplates were observed. The formation of nanosheets was a result of oxidation and rearrangement of micron sized ammonium molybdenum oxide particles, as was the case for particles obtained from 0.68M solution. The formation of nanoplates can be attributed to the crystallization of nano-sized particles in the as-synthesized powders.

II. ε-WO_3

Earlier studies have reported the particle size to play an important role in formation of ε-WO_3 polymorphs[5]. The selection of precursor was done in order to obtain a higher flame gradient and lower the residence time for the particles. Tungsten isopropoxide was used as a solute due to its combustible nature. The exothermic nature of the solute upon combustion aids in increasing the flame temperature and in turn lowers the residence time. For precursor solvent, iso-propanol was used. The selection of iso-propanol was done in order to prevent reaction between the isopropoxide chain and the solvent, as a breakdown of solute could affect the operating temperature of the process.

To understand the formation of ε-WO_3, it is important to understand the formation dynamics of particles through FSP. The size of particles formed in FSP depend on ODOP (one droplet to

one particle),ODMP (one droplet to multiple particles) or gas phase transition[16]. For homogenous solutions, ODOP results in formation of uniform particle sizes. Since two distinct particle sizes were obtained for the samples, the path followed by the process was likely the ODMP. This is due to the presence of an organic additive. The cracking of the additives during sintering process leads to formation of multiple particles and gives rise to a broad size distribution. Thus, the organic ligand attached to W atoms is responsible for the formation of multiple particles. For Cr-doped particles, the reaction between ammonium salts and diethylene glycol monobutyl ether/ethanol leads to formation of tungsten compounds attached to organic ligand from diethylene glycol monobutyl ether and NH_4OH. The resulting organometallic compound exhibits solubility in ethanol. The addition of chromium acetylacetonate also plays an important role in facilitating ODMP and the formation of ε-phase[16].

The final size of the crystallites depend on various parameters for ODMP, these are precursor composition, fuel and oxidant flow rate and size of droplet and flame[17]. A direct relation between oxidant flow-rate was noticed for Cr-doped particles. The particles reported here were slightly smaller compared to the particles reported in the literature[18]. With the ODMP mechanism, the formation of ε-WO_3 particles can further be explained. The precursor solutions upon entering the flame lead to vaporization and oxidation of W atoms. The existence of large temperature gradient prefers the formation of ε-WO_3 particles. The particles undergo sintering process, coagulation & agglomeration. The particle size depends on the residence time, which relates to the time the particles spend in the chamber upon atomization. A shorter residence time gives rise to small particle sizes and thus a stabilized ε-WO_3 is received. The formation of γ phase occurs once the critical crystallite size for the particles is crossed, this critical size can be calculated using a heuristic model[19].

The percentage of ε phase was slightly higher in pure WO_3 compared to Cr-doped WO_3. The concentration of metal ions in the isopropoxide solution was slightly lower compared to Cr-doped solution. However, the precursor salt also played an important role in formation of higher ε phase content. A W atom linked together with 6 iso-propoxide organic ligands, enables lower residence time compared to an organometallic-ammonium salt mixture; as was expected during the precursor selection.

III. $VOPO_4$

For synthesis of $VOPO_4$, ammonium salts were used as precursors. Ammonium vandate and ammonium dihydrogen were used due to their ready availability and low melting points. The melting points for ammonium vandate and ammonium dihydrogen phosphate are close to each other which played a major role in their selection. The melting points enables reaction and mixing of the components and formation of mixed oxides in uniform composition. A large variation in melting points of the two systems can significantly impact the reaction of particles in flame and result in secondary compounds.

The precursors were dissolved in water to obtain a homogenous solution. Ammonium dihydrogen phosphate was found to be insoluble in organic solvents at 0.1M concentrations. The homogeneity in solution was required in order to create homogenous droplets with equal concentrations of vanadium and phosphorous in order to obtain homogenous distribution in the processed particles. In order to make the process self-sustainable and generate a higher temperature gradient, organic precursors were added to the solution. The organic additives used were sucrose and DMF. The addition of components were to create a differential temperature gradient for the process and analyze their effect on the morphology and polymorphic nature of the flame synthesized particles.

The resultant powders from flame spray pyrolysis resulted contained a large amount of $NH_4VOVO_2(HPO_4)_2.1.5H_2O$. The formation the compound can be attributed to the reaction between ammonium vandate and ammonium dihydrogen phosphate in aqueous medium. The particles formed from sucrose based solutions were in micron range and hollow, the formation of such particles these large particles were a result of precursors with low enthalpies coupled with high melting/decomposition points[20]. Moreover, due to the usage of an aqueous solution, the temperature of the flame is significantly reduced for complete atomization of particles. The addition of sucrose although helped as few submicron sized particles were noticed, which is the size range for aqueous based precursors[16]. The particle size were further reduced with the addition of DMF. The addition of DMF possibly resulted in formation of organometallic compounds which in turn leads to formation of nanosized particles. The formation of organometallics also led to atomization of the precursor and formation of α_{II}-$VOPO_4$.

Upon calcination of as-synthesized products, the resultant powders were a mixture of α_{II}-$VOPO_4$ & β-$VOPO_4$ and α_{II}-$VOPO_4$ and δ-VOPO4. According to DFT calculations, the β-$VOPO_4$ is the most stable configuration for $VOPO_4$ [21, 22]. However, according to DFT calculations, there is only a small difference in energy between $VOPO_4$. Which suggest that temperature has little effect on phase transformation of $VOPO_4$ polymorphs. Although it has been reported that a slight change in synthesis conditions[23]. The primary difference in $VOPO_4$ structures occur in the form of V-O bond length, which in turn lead to different crystal structures and polymorphs.

The mixed polymorphs obtained here can be associated with the precursor, where, the formation of $NH_4VOVO_2(HPO_4)_2.1.5H_2O$ leads to multiple polymorphs. The precursor salt contains two valence states for VO in the form of $V(IV)O^{2-}$ and $V(V)O_2^-$. The Vanadium oxide with +5 valence state exhibits an orthovandate structure. Based on the results obtained, the orthovandate structure exhibits similar V-O bond length to α_{II}-$VOPO_4$. Hence, formation of α_{II}-$VOPO_4$ was observed in all the samples. The formation of β and δ polymorphs, are a result of the transformation of the +4 valence state VO^{2-} into a +5 valence state in an oxidative atmosphere. The oxidation leads to formation of V-O bond the length of which determines the formation of either β or δ polymorphs. The oxidation was noticed during the TGA analysis of particles synthesized with DMF precursor, where a slight increase in weight was observed at 420°C.

In case of powders synthesized using sucrose solution, the VO^{2-} transforms into the most stable state and thereby leads to the formation of β-$VOPO_4$. The synthesis of the δ polymorph has been reported earlier from the thermal oxidation of a +4 valency Vanadium hydrogen phosphate compound[24]. The compound was held at 400°C for 7 days for successful transformation into δ polymorphs. In this study, the smaller particle sizes led to faster transformations.

6.5 Polymorphic control through FSP

Based on the results obtained, it can be said that the precursor selection has a direct effect on the polymorphs formed through fsp. Organic precursors lead to high temperature gradients and ensure lower residence times. Particles stable in nanocrystalline form can be obtained at room temperature with quenching. The limitation of process lies in the fact that only polymorphs that exhibit stability at high temperatures can be quenched and stabilized at room temperature. In case of unavailability of any stable polymorphs at higher temperatures, quenching of the particles results in formation of amorphous compounds. These amorphous compounds then require a

secondary treatment, such as calcination, for formation of a stable polymorphs. The polymorphic formation in case of amorphous compounds, then depends on the particle sizes and thermodynamic conditions for formation of polymorphs at temperatures < melting point of the amorphous compounds. Even with secondary treatment, the particle sizes are retained (with negligible growth) and the calcined fsp particles are obtained with a homogenous size distribution; which is not the case for processing of these particles through conventional solvent based methods and calcination.

The use of aqueous based solutions and ammonium salts, lowers the operating temperature significantly. The lower temperature of operation results in formation of intermediate compounds and hollow micron sized particles. Similar to amorphous particles, these intermediate compounds can be converted into a stable oxide polymorphs with a secondary treatments, such as calcination. The formation of stable polymorphs is again governed by thermodynamic conditions for formation of polymorphs at temperatures < melting point. In this study, the grain sizes of these intermediate products were found to be in nanometers range. The smaller grain sizes resulted in breakdown of products upon calcination and nano-crystalline particles were obtained. The particles upon calcination were again found to exhibit homogenous size distribution.

To formation of intermediate products can be eradicated with use of either organic precursors that increase the flame gradient and provide temperatures high enough for complete oxidation to occur. In case of unavailability of organic precursors, a higher fuel content for operation of flame will result in higher flame temperature. The higher flame temperature will assist with combustion, vaporization and reaction of the aqueous precursors during fsp process.

References

1. Wegner, K. and S.E. Pratsinis, *Scale-up of nanoparticle synthesis in diffusion flame reactors*. Chemical Engineering Science, 2003. **58**(20): p. 4581-4589.
2. Ulrich, G.D., *Theory of Particle Formation and Growth in Oxide Synthesis Flames*. Combustion Science and Technology, 1971. **4**(1): p. 47-57.
3. Strobel, R., et al., *Unprecedented formation of metastable monoclinic BaCO3 nanoparticles*. Thermochimica Acta, 2006. **445**(1): p. 23-26.

4. Karthikeyan, J., et al., *Nanomaterial powders and deposits prepared by flame spray processing of liquid precursors.* Nanostructured Materials, 1997. **8**(1): p. 61-74.
5. Wang, L., et al., *Ferroelectric WO3 Nanoparticles for Acetone Selective Detection.* Chemistry of Materials, 2008. **20**(15): p. 4794-4796.
6. Rohner, F., et al., *Synthesis, Characterization, and Bioavailability in Rats of Ferric Phosphate Nanoparticles.* The Journal of Nurtition, 2007. **137**(3): p. 614-619.
7. Hansen, J.P., et al., *Synthesis of ZnO particles in a quench-cooled flame reactor.* AIChE Journal, 2001. **47**(11): p. 2413-2418.
8. Schulz, H., et al., *Independent Control of Metal Cluster and Ceramic Particle Characteristics During One-step Synthesis of Pt/TiO2.* Journal of Materials Research, 2005. **20**(9): p. 2568-2577.
9. Teoh, W.Y., R. Amal, and L. Mädler, *Flame spray pyrolysis: An enabling technology for nanoparticles design and fabrication.* Nanoscale, 2010. **2**: p. 1324-1347.
10. Jang, Y.J., C. Simer, and T. Ohm, *Comparison of zinc oxide nanoparticles and its nano-crystalline particles on the photocatalytic degradation of methylene blue.* Materials Research Bulletin, 2006. **41**(1): p. 67-77.
11. Shimizu, R., et al., *Low-temperature deposition of meta-stable β-MoO3(011) epitaxial thin films using step-and-terrace substrates.* Thin Solid Films, 2015. **595, Part A**: p. 153-156.
12. Gouma, P., K. Kalyanasundaram, and A. Bishop, *Electrospun single-crystal MoO3 nanowires for biochemistry sensing probes.* Journal of Materials Research, 2006. **21**(11): p. 2904-2910.
13. Park, G.D., S.H. Choi, and Y.C. Kang, *Electrochemical properties of ultrafine TiO2-doped MoO3 nanoplates prepared by one-pot flame spray pyrolysis.* RSC Advances, 2014. **4**(33): p. 17382-17386.
14. Gouma, P., K. Kalyanasundaram, and A. Bishop, *Electrospun single-crystal MoO3 nanowires for biochemistry sensing probes.* Journal of Materials Research, 2006. **21**(11): p. 23.
15. Oswald, H.R., J.R. Gunter, and E. Dubler, *Topotactic decomposition and crystal structure of white molybdenum trioxide-monohydrate: Prediction of structure by topotaxy.* Journal of Solid State Chemistry, 1975. **13**(4): p. 330-338.

16. Purwanto, A., W.-N. Wang, and K. Okuyama, *Flame Spray Pyrolysis*, in *Handbook of Atomization and Sprays: Theory and Applications*, N. Ashgriz, Editor. 2011, Springer US: Boston, MA. p. 869-879.
17. Strobel, R. and S.E. Pratsinis, *Flame aerosol synthesis of smart nanostructured materials.* Journal of Materials Chemistry, 2007. **17**(45): p. 4743-4756.
18. Wang, L., *Tailored synthesis and characterization of selective metabolite-detecting nanoprobes for handheld breath analysis*, in *Materials Science & Engineering*. 2008, Stony Brook University: Proquest LLC.
19. Sood, S., *Polymorphism control in nanostructured metal oxides*, in *materials science and engineering*. 2014, stony brook university: Proqueest llc.
20. Madler, L.e.a., *Flame Spray Pyrolysis: An enabling technology for nanoparticles design and fabrication.* NANOSCALE, 2010: p. 1324-1347.
21. Sun, W. and J. Du, *Structural stability, electronic and thermodynamic properties of VOPO4 polymorphs from DFT+U calculations.* Computational Materials Science, 2017. **126**: p. 326-335.
22. Ling, C., R. Zhang, and F. Mizuno, *Phase stability and its impact on the electrochemical performance of VOPO4 and LiVOPO4.* Journal of Materials Chemistry A, 2014. **2**(31): p. 12330-12339.
23. Dupré, N., et al., *Phase transition induced by lithium insertion in αI- and αII-VOPO4*. Journal of Solid State Chemistry, 2004. **177**(8): p. 2896-2902.
24. Girgsdies, F., et al., *The crystal structure of δ-VOPO4 and its relationship to ω-VOPO4.* Solid State Sciences, 2009. **11**(7): p. 1258-1264.

Chapter 7: Conclusion and future work

In this thesis, it has been demonstrated that the processing parameters greatly affect the formation of polymorphic ceramics. Metastable polymorphs have been synthesized using FSP process. Self-supported structures have also been obtained through electrospinning process. Following key points have been made

1. The precursor composition affects the polymorphic state of final products from the fsp.
2. Inclusion of organic solvents/metallo-organic component to the precursor solution increases the temperature gradient and favors the formation of metastable polymorphs.

This is the first effort to correlate the processing parameters and precursor dynamics with polymorphic states of ceramics processed through FSP.

7.1 Conclusions

I. Flame Spray Pyrolysis parameters

The precursor used for flame spray pyrolysis greatly affects the formations of ceramic polymorphs. The high temperature of operation and rapid solidification are key components that lead to formation of metastable polymorphs.

a) Flame synthesized MoO_3

For MoO_3, the particles synthesized resulted in thermodynamically stable α-MoO_3. The use of aqueous solution resulted in lowering the flame temperature and resulted in formation of micron sized particles. Smaller particles were obtained by lowering the concentration of solute and increasing the % of organic solvent in the precursor mixture. However, the nanoparticles obtained were amorphous in nature. The formation of small amorphous metal oxide signify that the process resulted in atomization of Mo atoms but the energy provided by the flame wasn't sufficient for crystallization of the oxidized particles. Increasing the organic content further in the precursor solution may result in one step synthesis of MoO_3 through fsp.

b) Flame synthesized WO_3 polymorphs

In case of WO_3, the use of metallo-organic precursor coupled with an organic solvent resulted in formation of nanoparticles (10-50nm). The high temperature of operation coupled with rapid solidification led to the stabilization of metastable ε-polymorph. The content of ε-phase obtained in pure form was higher than the previously reported material synthesized via doping. The particle formation mechanism plays an important role in the higher content of metastable form. It has been shown that the ε-phase exists below a critical particle size. High amount of organic components in the pure WO_3 precursor led to high temperature gradient and formation of particles below the critical particle size. The high concentration of smaller particles translated into higher ε-phase content in pure WO_3. The loss in % phase content was minimal upon heat treatment as the smaller particles didn't cross the critical particle size for $\varepsilon \rightarrow \gamma$ transformation. The content can further be increased with higher flame temperature (less dispersion/oxidant flow and/or higher fuel flow), inclusion of organic components with lower combustion enthalpies (results in larger flame gradient and lowers the residence time) and/or controlling the size by higher flow rate.

c) $VOPO_4$ Polymorphs

$VOPO_4$ polymorphs were successfully synthesized using FSP process. The use of ammonium salts in aqueous solutions led to lower temperatures and resulted information of intermediate compounds and micron sized particles. $VOPO_4$ was easily obtained from the intermediate compounds by calcination. The precursor used favored formation of α_{II}-$VOPO_4$. Addition of organic component resulted in nanoparticles along-with small % of crystalline α_{II}-$VOPO_4$ structures in as-synthesized powders. Secondary phases were formed due to oxidation of lower valence state vanadium compound in the as-synthesized fsp powders. Particle size played an important role in forming a polymorph upon oxidation of lower valence state compound. Smaller particle size favored formation of metastable δ polymorph, whereas, large particle sizes tend to form stable β polymorph. Based on these results, other precursor compounds can be investigated towards formation of other polymorphs for $VOPO_4$. An organic precursor in organic solvent should be the route followed for one-step synthesis of $VOPO_4$ polymorphs via FSP.

III. Flame spray synthesis of polymorphs

From the study, it can be concluded that the precursor parameters have a direct effect on the formation of polymorphs through FSP. The changes in temperature of operation due to combustion enthalpies of the precursors govern the residence time and formation of polymorphs. Metastable polymorphs are achieved by use of organic solute/solvents which increase the flame temperature and lowers residence times. A combustible solute coupled with organic solvent offers least residence time and results in higher amount of metastable phase at RT. The polymorphic behavior can be controlled with the knowledge of high temperature phase formation and engineering of the fsp precursors.

7.2 Future Research Directions

I. Development of process map for formation of polymorphs through FSP

It has been demonstrated that the precursor solute and solvent play an important role in formation of polymorphic ceramics through fsp. Based on the results obtained, further investigations need to be made in the formation of metastable polymorph by developing a theoretical model. The factors taken into account should include combustion enthalpies of solute, boiling point of solvent, residence time, flame temperature, enthalpy of combustion, and enthalpy of formation. The feasibility of the model should be investigated through experiments into formation of other metastable polymorphs.

II. Investigation into self-supported structures for other ceramics

Self-supported structures were obtained via electrospinning by polymer self-assembly. The inability of ceramics to stabilize in for of nanowires led to formation of agglomerated particles which mimicked the intermediate polymer foam structure. The porous foam structures were found to be activated in visible light region and can be applied to photocatalysis. Further investigations need to be made on the photocatalytic activity of these self-supported structures and compare them

with loose powders. The feasibility of formation of self-supported structures for ceramics exhibiting similar behavior should be investigated as well.

Appendix A: Novel synthesis of Cu-Fe mix metal oxides

Introduction

There has been growing interest in self-supported nanostructures, such as metal oxide foams, where the use of dispersed nanostructures may present problems. These include photocatalytic, electrochemical fuel cells, batteries, and gas sensors [1].

$CuFe_2O_4$ finds a wide variety of applications such as gas sensing for H_2 and H_2S sensing[2, 3], catalysts[4, 5], battery electrodes[6] and visible light photocatalysts[7]. Recent studies by our group have resulted in synthesis of self-supported structures of CuO and $CuWO_4$ using blend electrospinning and thermal oxidation of Cu grids[8, 9]. In this study, the same principle is used for synthesis of $CuFe_2O_4$.

Experimental methods

The precursor for the synthesis was performed by mixing iron nitrate nonahydrate in ethanol in a 0.1M concentration. The solution was mixed by ultrasonication for 2 hours and then aged 24h. For electrospinning a 0.1M PVP solution was prepared in ethanol. The iron nitrate and PVP solutions were mixed in the ratio of 1:4 for the final electrospinning solution.

Electrospinning was performed using a lab setup with 22 gauge needle. The parameters used for electrospinning were 20KV voltage, 10cm needle to collector distance, 20µL/min flow rate. The collector used for collecting the electrospun fibers was a copper grid (200 mesh, wire dia. 51µm).

Thermal oxidation of PVP deposited Cu substrate was carried out in a resistively heated furnace at a constant rate of 10ºC/min to the oxidation temperatures of 400 and 500ºC and held for 5 hours then cooled to ambient temperature.

The morphology of synthesized grids was evaluated using SEM (Leo 1550) with EDS capabilities and TEM (JEOL 1400). The structural characterizations were performed using XRD and UV-Vis.

Results

X-Ray Diffraction

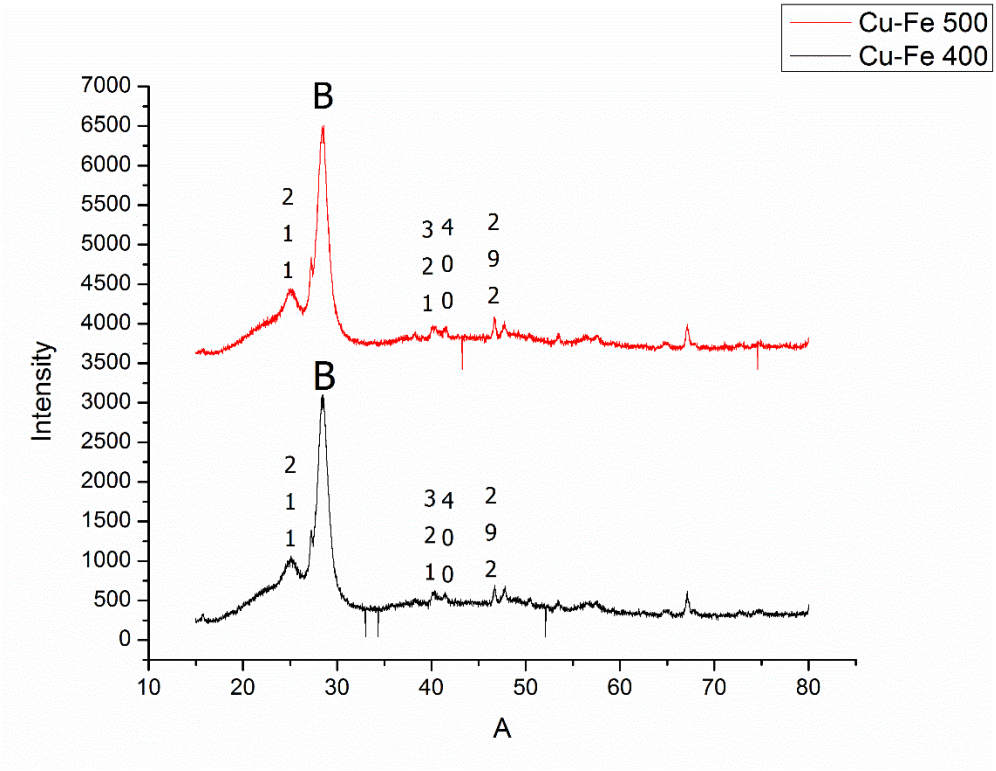

Figure A-1: XRD of self-supported $CuFe_2O_4$ grids

XRD characterization on the samples matched with JCPDS 72-1174 for tetragonal $CuFe_2O_4$. A large peak was noticed at 2Θ values of 29 and was related to the glue used to hold the samples on the substrate

UV-Vis

UV-Vis spectra was collected on both the samples and resulted in absorption in the visible light region. The calculated band gap for sample calcined at 400ºC is 2.07eV. A slight shift in band gap is noticed for the samples calcined at 500ºC, the calculated band gap is 2.05 eV. The slight shift can be related to the $CuFe_2O_4$ grain sizes at different calcination temperatures. Such effect due to calcination temperatures has earlier been observed for TiO_2 nanofibers[10].

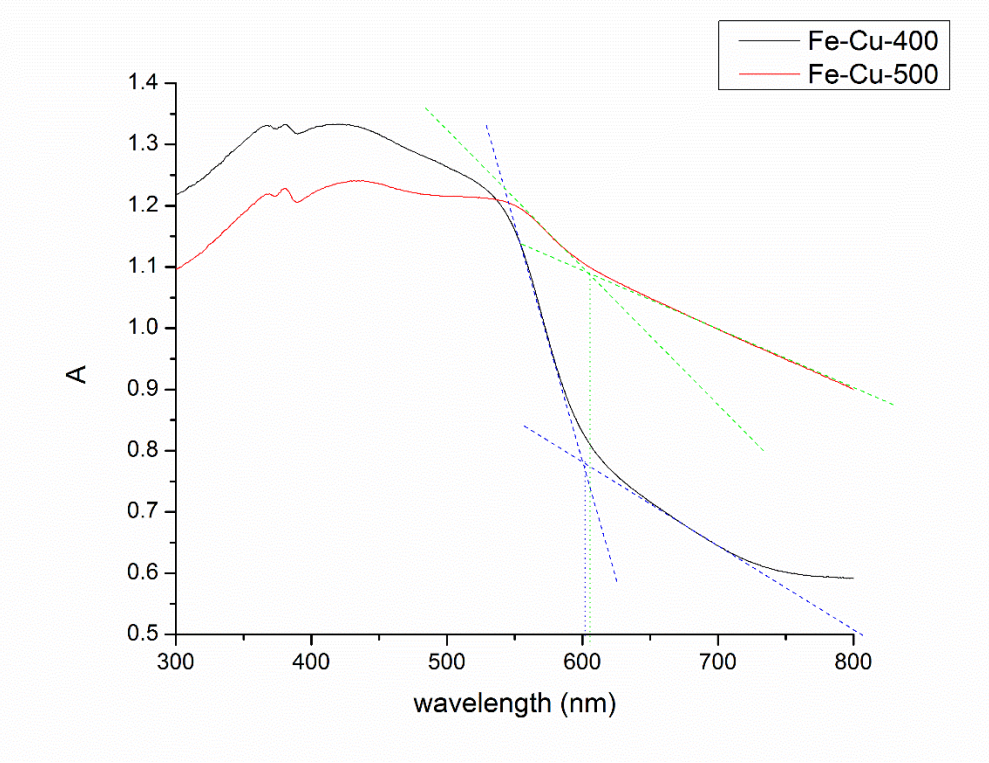

Figure A-2: UV-Vis spectra of $CuFe_2O_4$ after calcination at 400 and 500°C

SEM

SEM imaging was done on electrospun fibers and the grid samples obtained after calcination of Cu-grids and electrospun fibers at 400 and 500ºC. The as-spun fibers were found to be in the range of 200-600nm diameter range. High-magnification using a backscatter detector (Fig. A-3(b)) showed inclusion of Fe particles inside the fibers through atomic contrast. For the calcined samples, the samples calcined at 400ºC show fibers with 100-150nm covered by nanosized particles. EDS spectra (Fig. A-3(d) inset) on the nanosized particles gave high peaks for Fe and O, small peaks were obtained for Cu. The samples calcined at 500ºC show fibers with 50-100nm covered by nanosized particles. EDS spectra (Fig. A-3(f) inset) on the nanosized particles gave high peaks for Fe and O, small peaks were obtained for Cu. However, the Cu peaks for samples calcined at 500 ºC were larger compared to those obtained for samples calcined at 400ºC. The higher peaks could be a result of more Cu diffusion at higher temperatures.

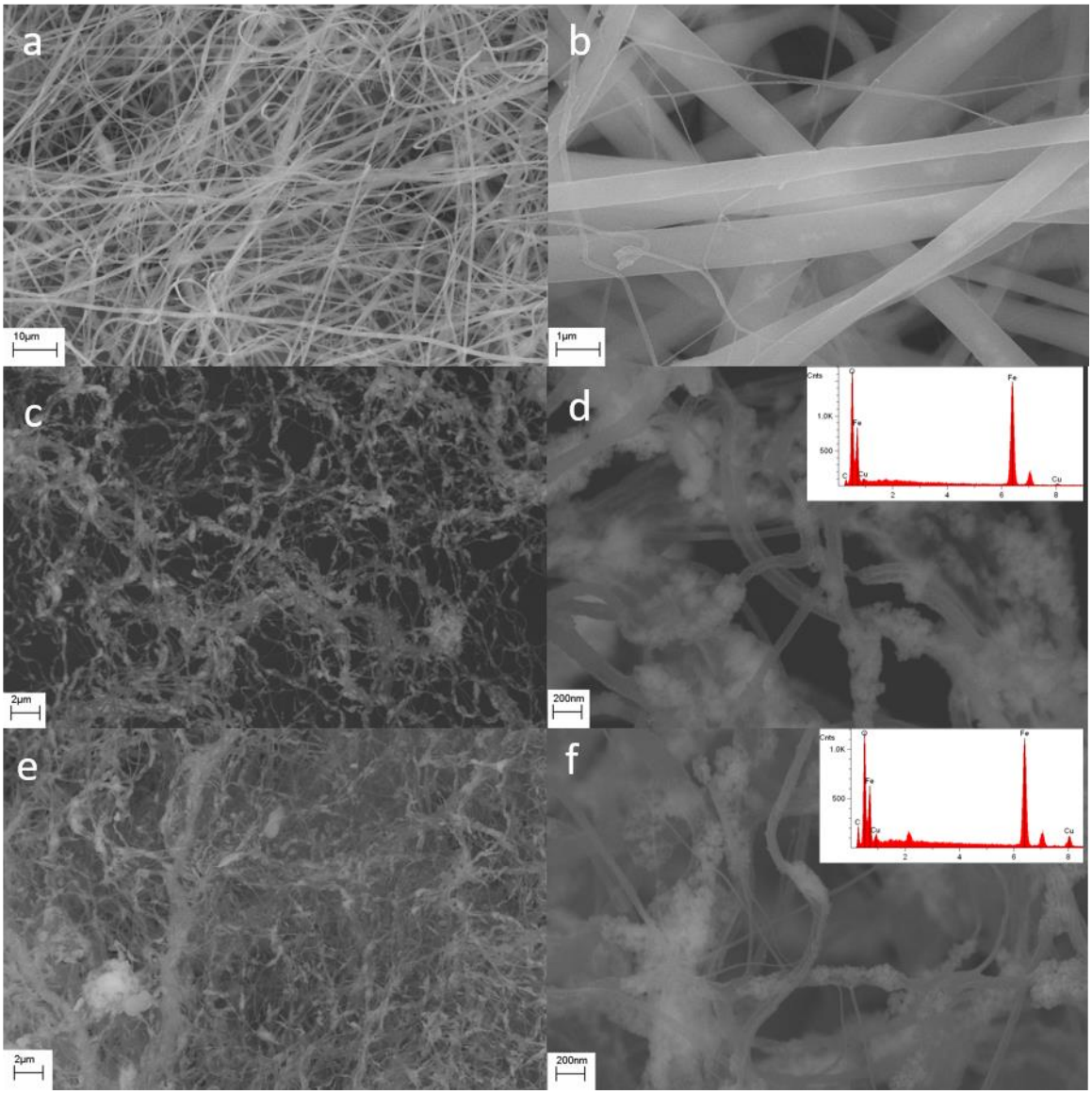

Figure A-3: SEM images of (a) electrospun PVP+$FeNO_3$ nanofibers (b) High-magnification image of electrospun PVP+$FeNO_3$ nanofibers (c) $CuFe_2O_4$ grids calcined at 400°C (d) High-magnification image of $CuFe_2O_4$ grids calcined at 400°C (inset EDS spectra) (e) $CuFe_2O_4$ grids calcined at 500°C (f) High-magnification image of $CuFe_2O_4$ grids calcined at 400°C (inset EDS spectra)

TEM

TEM analysis was done on the calcined samples. The samples were in the form of fibers covered with nanoparticles as was seen in SEM. For the samples calcined at 400ºC the nanoparticles were found to be in the size range of 10-20nm. SAED on the nanoparticles resulted in rings which matched with JCPDS 72-1174 for tetragonal $CuFe_2O_4$. For the samples calcined at 500ºC the

nanoparticles were found to be in the size range of 20-30nm. SAED on the nanoparticles resulted in rings which matched with JCPDS 72-1174 for tetragonal $CuFe_2O_4$. The higher particle size was a result of higher calcination temperature, which resulted in grain growth.

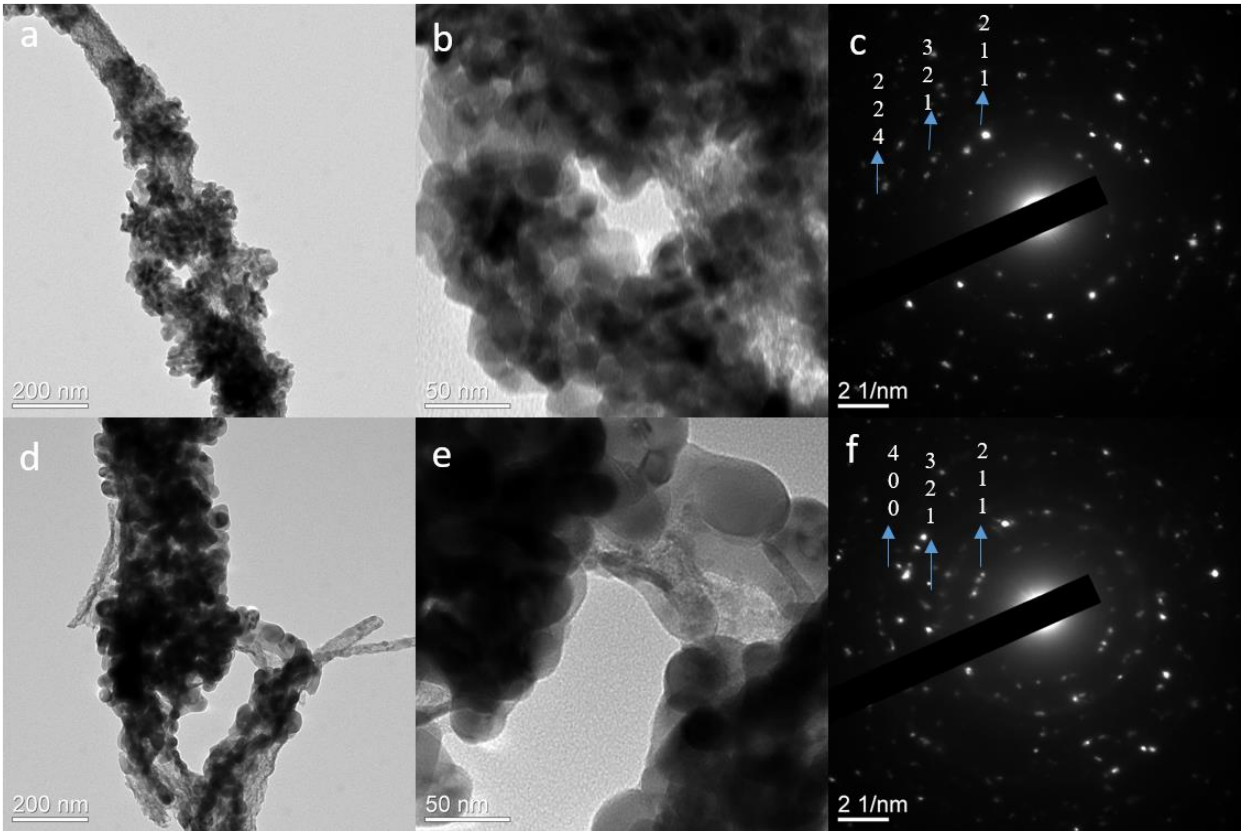

Figure A-4: TEM images and SAED patterns for (a) samples calcined at 400°C (b) high magnification image for samples calcined at 400°C (c) SAED pattern for samples calcined at 400°C (d) samples calcined at 400°C (e) high magnification image for samples calcined at 400°C (f) SAED pattern for samples calcined at 400°C

Discussion

Formation of Fe_2O_3 fibers has earlier been reported by electrospinning polymer+ iron nitrate nonahydrate sol [11, 12]. The degradation and oxidation of iron nitrate nonahydrate and formation into Fe_2O_3 has been found to occur at 300ºC[13]. The oxidation of Cu and its diffusion into the polymer nanofibers have been reported to start at 200ºC[8]. The diffusion of Cu inside the fibers leads to formation of embedded Cu Fibers. When the temperature is raised, the diffused Copper and iron nitrate sol particles start to oxidize and start to form a solid solution. The formation of $CuFe_2O_4$ starts to occur at ~390ºC and it crystallized into cubic $CuFe_2O_4$ at higher temperatures[14]. The earlier reported literature contained peaks for CuO for calcination

temperatures in the range of 300-600ºC. However, no peaks were noticed for CuO during XRD, the peaks could be suppressed due to high peaks from the background. A thin film XRD is needed to better characterize the sample.

Conclusion

Self-supported structures of $CuFe_2O_4$ have successfully been synthesized using blend electrospinning and thermal oxidation. The samples have a band gap energy of 2.05-2.07eV and can be used as visible light photocatalysts.

References

1. Walcarius, A., *Template-directed porous electrodes in electroanalysis.* Analytical and Bioanalytical Chemistry, 2010. **396**(1): p. 261-272.
2. Abu Haija, M., et al., *Characterization of H2S gas sensor based on CuFe2O4 nanoparticles.* Journal of Alloys and Compounds, 2017. **690**: p. 461-468.
3. Abu Haija, M., et al., *Selective hydrogen gas sensor using CuFe2O4 nanoparticle based thin film*. Applied Surface Science, 2016. **369**: p. 443-447.
4. Ghaani, M. and J. Saffari, *Synthesis of CuFe2O4 Nanoparticles by a new co-precipitation method and using them as Efficient Catalyst for One-pot Synthesis of Naphthoxazinones.* Journal of Nanostructures, 2016. **6**(2): p. 172-178.
5. Eisavi, R., et al., *Magnetically separable nano CuFe2O4: an efficient and reusable heterogeneous catalyst for the green synthesis of thiiranes from epoxides with thiourea.* Journal of Sulfur Chemistry, 2016. **37**(5): p. 537-545.
6. Luo, L., et al., *High lithium electroactivity of electrospun CuFe2O4 nanofibers as anode material for lithium-ion batteries.* Electrochimica Acta, 2014. **144**: p. 85-91.
7. Yang, H., et al., *Photocatalytic activity evaluation of tetragonal CuFe2O4 nanoparticles for the H-2 evolution under visible light irradiation.* Journal of Alloys and Compounds, 2009. **476**(1-2): p. 715-719.
8. Lee, J. and P.I. Gouma, *Tailored 3D CuO Nanogrid Formation.* Journal of Nanomaterials, 2011. **2011**: p. 6.
9. Lee, J., *Synthesis and Characterization of Nanostructured Metal Oxide for Water Remediation and Energy Applications*, in *Materials Science & Engineering*. 2013, Stony Brook University: ProQuest LLC.

10. Topcu, S., G. Jodhani, and P. Gouma, *Optimized Nanostructured TiO2 Photocatalysts.* Frontiers in Materials, 2016. **3**(35).
11. Zheng, W., et al., *Electrospinning route for α-Fe2O3 ceramic nanofibers and their gas sensing properties.* Materials Research Bulletin, 2009. **44**(6): p. 1432-1436.
12. Cheng, Y., et al., *Formation mechanism of Fe2O3 hollow fibers by direct annealing of the electrospun composite fibers and their magnetic, electrochemical properties.* CrystEngComm, 2011. **13**(8): p. 2863-2870.
13. Melnikov, P., et al., *Thermal decomposition mechanism of iron(III) nitrate and characterization of intermediate products by the technique of computerized modeling.* Journal of Thermal Analysis and Calorimetry, 2014. **115**(1): p. 145-151.
14. Köferstein, R., et al., *Crystallite-growth, phase transition, magnetic properties, and sintering behaviour of nano-CuFe2O4 powders prepared by a combustion-like process.* Journal of Solid State Chemistry, 2014. **213**: p. 57-64.

Appendix B. Self-Supported Nano-WO_3 Foams formed by Self-Assembly of Non-Woven Mats

B1 Introduction:

There has been growing interest in self-supported nanostructures, such as metal oxide foams, where the use of dispersed nanostructures may present problems. These include photocatalytic, electrochemical fuel cells, batteries, and gas sensors [1]. The reported techniques for synthesizing foams either require complex processing (e.g. templating [2, 3] filling with metal oxide sol and later calcined or subjected to combustion to obtain foams; or by the thermal treatment of pure metal blocks where the precursors are typically costly [4].

Wei et al. [5] produced thin-walled WO_3 networks by mixing tungsten powder in H_2O_2/Methanol and poly-vinylpyrrolidone(PVP). The mixture formed a gel and foams were obtained following calcination. The formation of foams was due to the oxidation of tungsten particles inside the polymer matrix, which led to a network like structure. The formation of network like structure was attributed to a viscous gel formation between the tungsten powder in H_2O_2/methanol and PVP upon evaporation of excess water. Crystalline foams were obtained after calcination of the viscous mixture and decomposition of PVP. The foams obtained through the process had a wide range of pore sizes; porosity control was not possible, as the pore formation of foams occurred by calcination.

A recent study has reported formation of *polymer foams* through the electrospinning process [6]. Nanofibrous foams of Poly(3-caprolactone) were formed with relative ease by the electrospinning process. The polymer foams were obtained by the decomposition of polymer beads in the honeycomb mats. Furthermore, electrospinning-based manufacturing of metal oxides was reported before by our group [7-9]. Blend electrospinning involving tungsten isopropoxide ($C_{18}H_{42}O_6W$) and Poly-Vinyl acetate, was the path followed. Earlier results showed formation of WO_3 nanowires upon calcination. The formation of fiber structures were a result of high sol gel concentration in the composite nanofibers.

In this study, a straightforward and cost effective route to produce metal oxide foams is explored involving the electrospinning process. Tungsten trioxide was chosen as candidate for the study as it finds diverse applications (as visible light photocatalyst, gas sensor, electrochromic material, etc.) and occurs in a variety of polymorphs. Electrospinning of self-supported metal oxide

nanofibrous architectures were achieved before by our group [8-10]. Blend electrospinning involving tungsten isopropoxide ($C_{18}H_{42}O_6W$) and cellulose acetate, is explored in this work to make nanostructured foams of WO_3.

B2 Experimental Methods:

WO_3 sol was prepared using tungsten isopropoxide (All Chemie Ltd.) as a precursor to blend electrospinning. The sol was prepared with 0.2M concentration in butanol and was subjected to ultrasonic mixing and 48h aging, to allow sufficient time for butoxide substitution. A solution of 0.1M cellulose acetate (CA) (Aldrich 419028) in 40% acetic acid and 60% acetone was prepared; the aged sol was mixed with CA solution in the ratio of 1:4 respectively. The resultant solution was prepared for electrospinning and the resulting as-spun mats were heat treated at 375°C for 8h; the heating and cooling rate were set at 175°C/h.

To study the effect of electrospinning on formation of foam structures, thin films were formed on glass substrate by spin coating. Formation of layer on the substrate occurred in 2 cycles, for the first cycle the spin coating parameters were 1000RPM for 9 seconds and for the second cycle the parameters were 200 RPM for 20 seconds. The thickness of the film was controlled by the number of layers deposited on the substrate (1-3), each previous layer was completely dried before the next layer was deposited on top. The spin-coated thin films were subjected to same thermal treatment as the electrospun samples. Scanning Electron microscopy (SEM, LEO 1550) was conducted on the electrospun and spin coated samples. The electrospun samples, obtained upon thermal treatment, were further characterized using transmission electron microscopy (TEM, JEOL 1400), selected area diffraction (SAED), FTIR (Thermo Scientific Nicolet 6700) (XRD, Rigaku Miniflex II) and UV-Vis Spectrometer (Jasco J-815).

B3 Results

B3.1 X-Ray Diffraction

Figure 1 below shows the XRD patterns of the WO3 foams. The peaks obtained come from two phases and were matched to the cubic WO_3 (JCPDS 41-905) and a non-stoichiometric oxide of tungsten $WO_{2.9}$ (JCPDS 18-1417). Formation of cubic WO_3 has earlier been reported by our group when annealing the as-spun mats at these temperatures[11]. The formation of non-stoichiometric phase is attributed to an oxygen deficient environment occurring during polymer

degradation upon heat-treatment. The relative phase distribution is 60% cubic WO_3 and 40% tetragonal $WO_{2.9}$, based on the relative peak intensities from the XRD pattern.

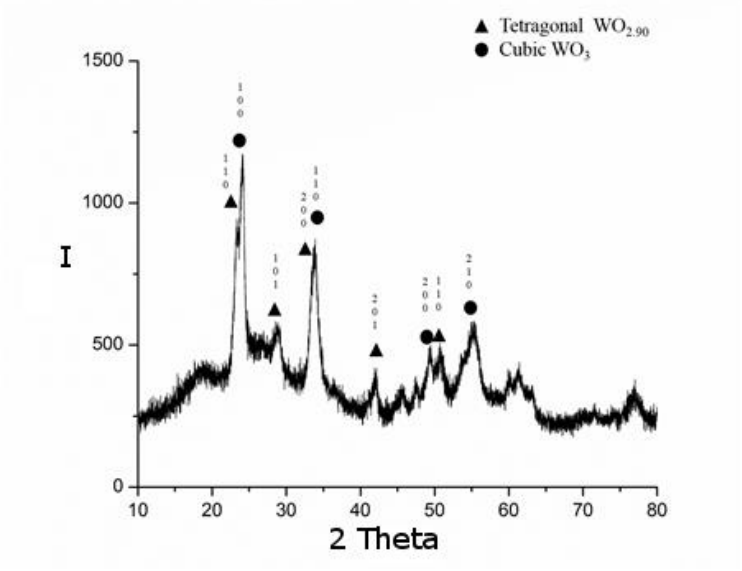

Figure B-1: X-ray Diffraction pattern for foam structure

B3.2 Fourier Transform Infrared Spectroscopy

The FTIR analysis carried out on the samples resulted in broad peak centered at 750cm^{-1}. The peak can be associated with formation of tungstate[12]. The occurrence of a broad peak can be attributed to a two phase system. The non-stoichiometric $WO_{2.9}$ leads to multiple valence state of tungsten atoms, which results in a broad region during the FTIR characterization. Small peaks were noticed at 1080 cm^{-1}, 1260 cm^{-1} and 1600 cm^{-1}, the inclusion of these peaks indicate small amounts of undecomposed carbon in the sample.

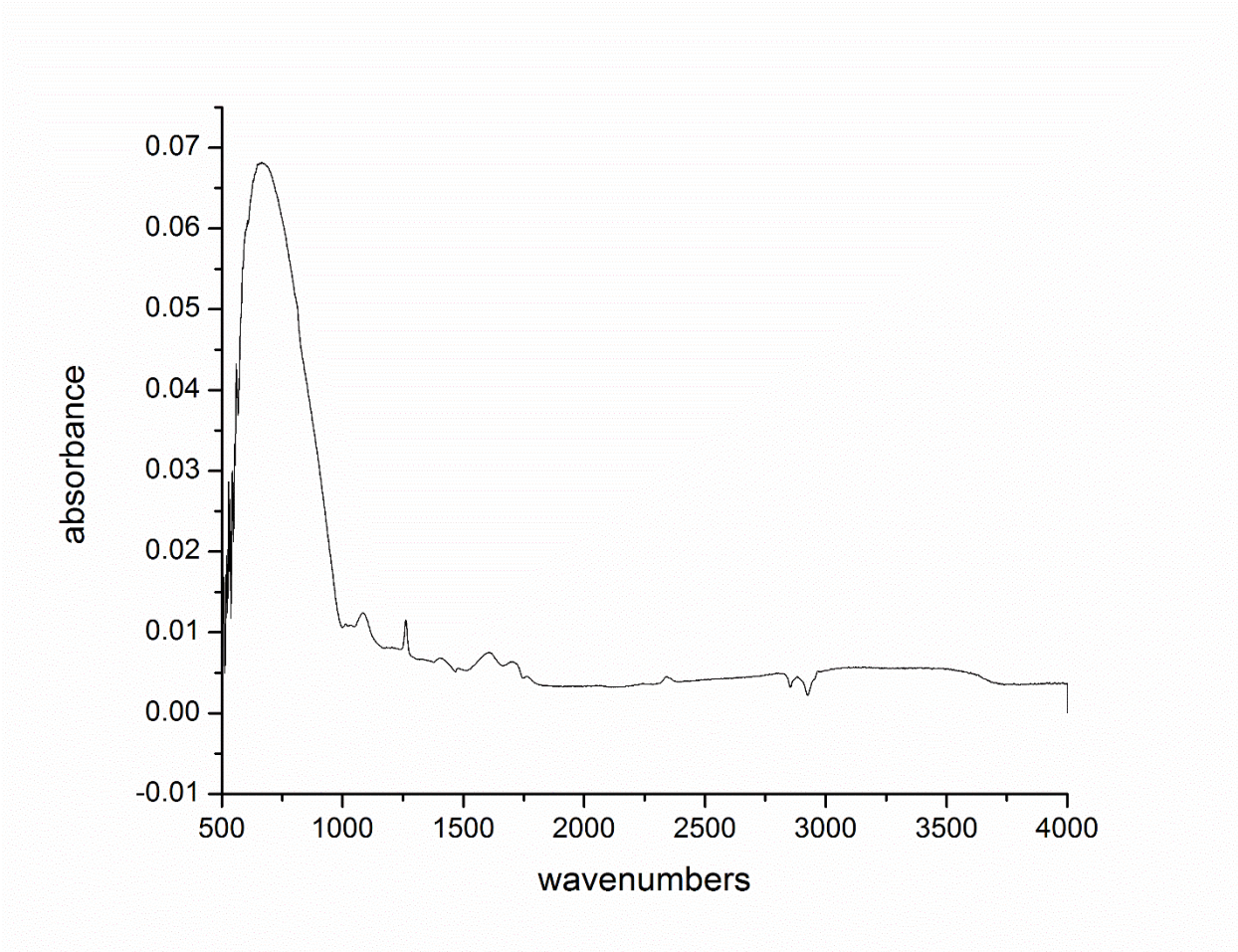

Figure B-2: FTIR spectra of foams

B3.3 Scanning electron microscopy

I. Foam samples

Figure B3 (a) below shows the Scanning Electron Micrographs for as spun CA-sol-gel nanofibers. Bead formation is seen in the fibers, the formation of beads being the result of a viscous gel formation of the polymer and oxide precursor. Figure B3(c) shows Scanning Electron Micrographs of the heat-treated samples that further reveal the foam structure. Highly porous foams with a large pore density were obtained by the calcination of the electrospun mats. Typical pore sizes were in the range of 50-70μm.

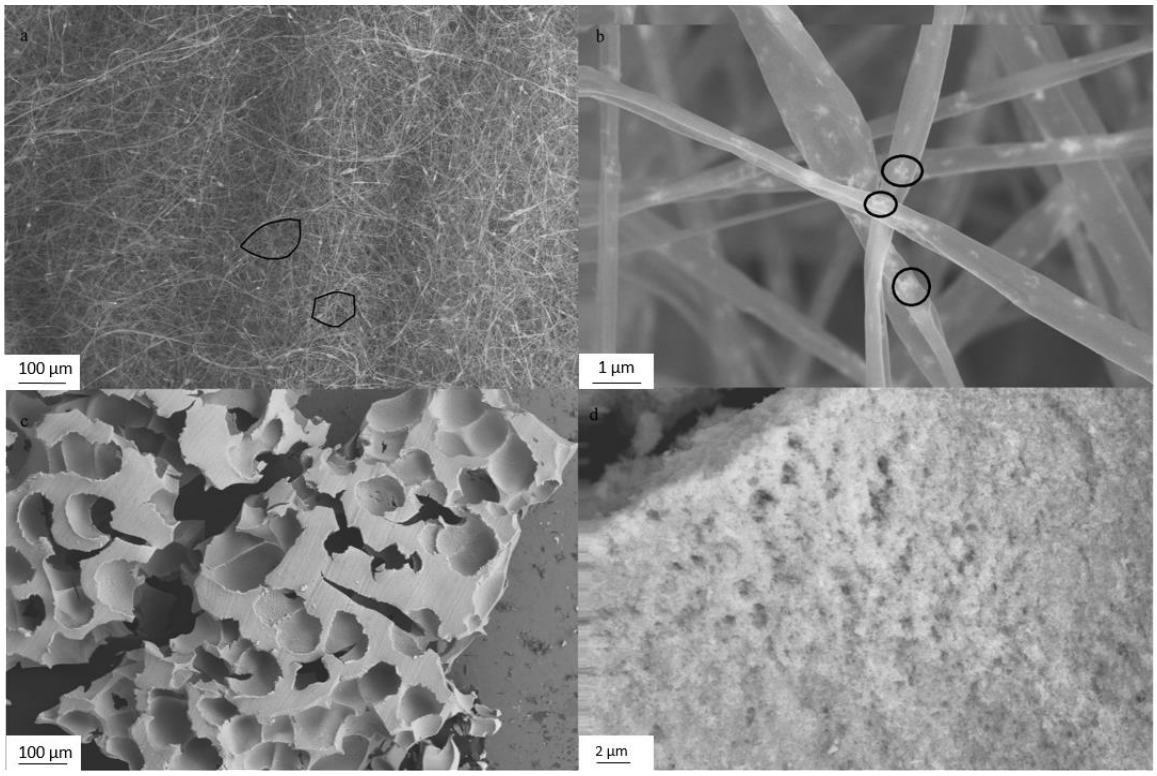

Figure B-3:a) SEM image of as spun fibers, highlighting the formation of honeycomb structures b) High magnification SEM image of fibers highlighting the sol particles in the fibers c) SEM image of foam structures obtained after thermal treatment at 375^0C d) High magnification SEM image of foam surface showing the agglomerated sol particles and nano porosity.

II. Comparison with spin coated films

Figure B4 shows the SEM images for the spin-coated films. As the number of layers increased, the distribution of particles on the surface of the substrate increased upon heat-treatment. This corresponds to a higher amount of sol being present in the thicker films. Upon thermal treatment and degradation of polymer, the metal oxide film appears to have collapsed and the nanoparticles are now randomly distributed all over the substrate.

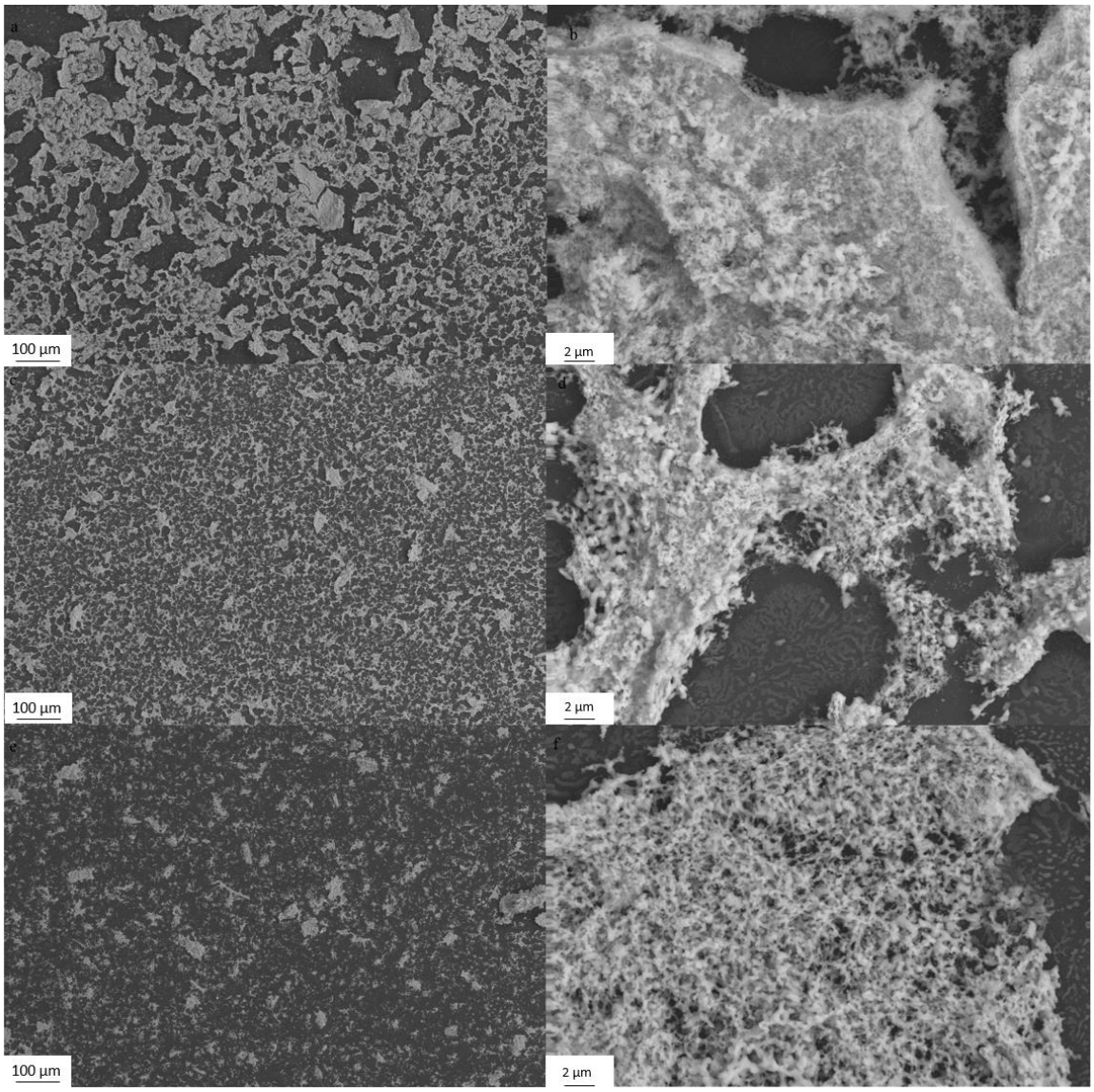

Figure B-4: SEM image of thermally treated spin coated films coated (a,b) 3 times, (c,d) 2 times (e,f) 1 time

Whereas self-supported foams were obtained via elecrospinning process, loose powder networks were seen on the as-spun samples. Figure 6 compares and contrasts the morphologies of (a) foams obtained upon heat treatment of electrospun mats and (b) heat treated thin films.

B3.4 Transmission Electron Microscopy

Figure B-5a and B-5b show TEM micrographs and SAED patterns for the thermally-threated material. Highly crystalline WO_3 grains of 20-30nm could be observed inside the foam

matrix. A dense distribution of nano sized pores was also observed inside the matrix. The electron diffraction pattern (Fig. B-5b) show rings that correspond to the cubic phase of WO_3(JCPDS #41-905) and match with XRD analysis results.

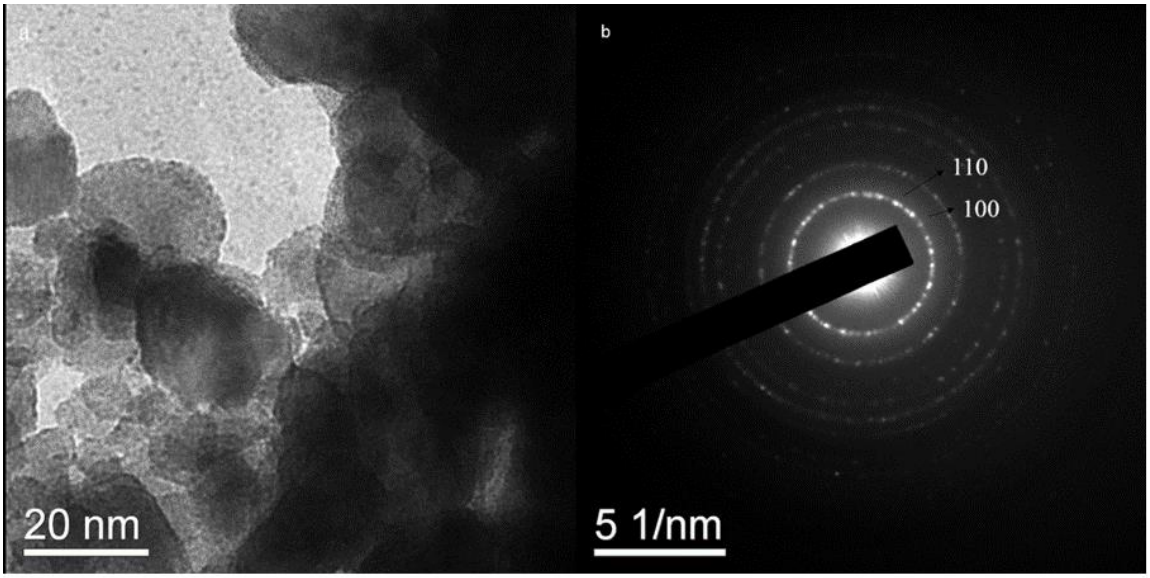

Figure B-5: (a, b) TEM images and SAED pattern of foam structure respectively

B3.5 UV-Vis Spectroscopy

Optical absorption spectra of the WO_3 foam are shown in Fig. 4a.The light adsorption spectrum and the band gap energy of the samples were calculated using the formula $(\alpha h\nu)^2 = A(h\nu - E_g)$. This equation applies to a direct band gap material.(α:absorption coefficient, h:Planck constant = 6.63 x 10-34 J s, v: light frequency, E_g: band gap and A: constant with a value of 1, respectively[13]. The value of the band gap (E_g) is obtained by extrapolating the slope of the $(\alpha h\nu)^2$ - hv plot to where it crosses the x axis (as shown in Fig 4b). Thus, the value of E_g is estimated to be 2.53eV for this material. The band gap is the lowest reported for WO_3 nanostructures. The foam, thus, absorbs light with wavelengths in the visible part of the solar spectrum.

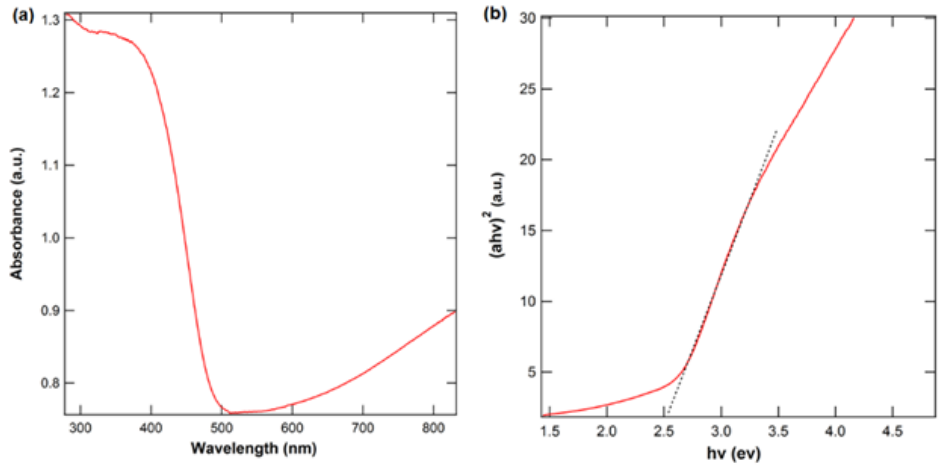

Figure B-6: (a) UV-Vis absorption spectra of foam (b) the plot of band gap energy and $(\alpha h\nu)^2$ of WO_3 foam

Table B-0-1 Reported Band Gap values for WO_3 Structures

Material	Morphology	Polymorph	Band Gap, eV	Reference
Commercial WO_3 (Sigma Aldrich)	Nanoparticles	Monoclinic	**2.61**	[14]
WO_3	flake shaped particles	Monoclinic	**2.6**	[15]
WO_3	Nanospheres	Monoclinic	**2.53**	[16]
WO_3	Nanoplates	Orthorhombic	**2.73**	[16]
WO_3	Nanorods	Hexagonal	**3.12**	[16]
WO_3	3D Nanoporous Films	Orthorhombic	**2.73**	[17]

B4 Discussion

The foam structure has likely resulted from the formation of a thick, viscous gel by the sol+CA solution used for electrospinning. The gel formation was the outcome of the interaction of the polymer with metal oxide sol. Such polymer-metal oxide interaction has been reported earlier

for hydrated zirconia (HZ)/alumina(HA) with PVP[18]. It was observed that the addition of PVP enhanced the crystallization and dehydration of HZ/HA. The interaction between the PVP and HZ/HA changed during the dehydration process where formation of poly-N-butyl-γ-aminobutyric acid was observed instead. Upon thermal treatment of the mixture at 500ºC, pure metal oxides were obtained without any carbon traces.

In this study the polymer-sol gel interactions resulted in a non-homogenous solution. Upon electrospinning beaded fibers were noticed; the formation of beads were partly due to the lack of homogeneity in the solution. Figure 2b is a high magnification image revealing a high concentration of the sol-gel material within the polymer beads. Figure 2a highlights in black polygonal areas of porosity outlined by a high density of beads. The shape and area of these polygons are consistent with the shape and size of the large pores in the foam. Previous work by Schlatter et al. [6] has described the formation of self-assembled honeycomb structures in electrospun polymers. Beads or thicker fibers typically "framed" the walls in these structures.

In the case of CA+sol electrospun mats, when subjected to thermal treatment at 375^0C, the polymer component melts between 170-240^0C and breaks down at 370^0C to water, carbon oxides (CO and CO_2) and methane under an oxidative atmosphere[19]. Upon the polymer decomposition, the sol particles agglomerate to form a dense structure while maintaining a nano structure and nano- sized surface porosity (fig 2d). The macroscopic porosity seen in the foams can be attributed to the honeycomb structures formed during the self-assembly of electrospun mats as discussed above.

5.5 Conclusion:

We have successfully demonstrated the synthesis of self-supported WO_3 foams via the self-assembly of electrospun fibers. The foams have a band gap of 2.53eV and can be used as visible light photocatalysts.

References

1. Walcarius, A., *Template-directed porous electrodes in electroanalysis.* Analytical and Bioanalytical Chemistry, 2010. **396**(1): p. 261-272.

2. Walsh, D., et al., *Dextran templating for the synthesis of metallic and metal oxide sponges.* Nat Mater, 2003. **2**(6): p. 386-390.
3. Maekawa, H., et al., *Meso/Macroporous Inorganic Oxide Monoliths from Polymer Foams.* Advanced Materials, 2003. **15**(7-8): p. 591-596.
4. Park, E.S. and S.D. Poste, *Ceramic foams*. 1989, Google Patents.
5. Wei, X. and P. Shen, *Fabrication and characterization of multidimensional tungsten oxide networks.* Science in China Series B: Chemistry, 2005. **48**(6): p. 511-515.
6. Ahirwal, D., et al., *From self-assembly of electrospun nanofibers to 3D cm thick hierarchical foams.* Soft Matter, 2013. **9**(11): p. 3164-3172.
7. Sawicka, K. and P. Gouma, *Electrospun composite nanofibers for functional applications.* Journal of Nanoparticle Research, 2006. **8**(6): p. 769-781.
8. Sawicka, K.M., A.K. Prasad, and P.I. Gouma, *Metal Oxide Nanowires for Use in Chemical Sensing Applications.* Sensor Letters, 2005. **3**(1-1): p. 31-35.
9. Wang, G., et al., *Fabrication and Characterization of Polycrystalline WO3 Nanofibers and Their Application for Ammonia Sensing.* The Journal of Physical Chemistry B, 2006. **110**(47): p. 23777-23782.
10. Sawicka, K.M. and P. Gouma, *Electrospun composite nanofibers for functional applications.* Journal of Nanoparticle Research, 2006. **8**(6): p. 769-781.
11. Sood, S., K. Kisslinger, and G. P, *Nanowire Growth by an Electron-Beam-Induced Massive Phase Transformation.* JOURNAL OF THE AMERICAN CERAMIC SOCIETY, 2014. **97**(12): p. 3733-3736.
12. Socrates, G., *Infrared and Raman Characteristic Group Frequencies: Tables and Charts.* #rd ed. 2004: Wiley.
13. Xu, Z., et al., *Preparation of platinum-loaded cubic tungsten oxide: A highly efficient visible light-driven photocatalyst*. Materilas Letters, 2011. **65**: p. 1252-1256.
14. Wicaksana, Y., et al., *Tungsten Trioxide as a Visible Light Photocatalyst for Volatile Organic Carbon Removal.* Molecules 2014: p. 19, 17747-17762.
15. Luevano-Hipolito, E., et al., *Synthesis, characterization and photocatalytic activity of WO3/TiO2 for NO removal under UV and visible light irradiation.* Materials Chemistry&Physics, 2014: p. 208-213.

16. Farhadiana, M., P. Sangpouta, and G. Hosseinzadeh, *Morphology dependent photocatalytic activity of WO3 nanostructures*. Journal of Energy Chemistry, 2015: p. 171-177.
17. Oua, J.Z., et al., *Anodic formation of a thick three-dimensional nanoporous WO3 film and its photocatalytic property*. Electrochemistry Communications, 2013: p. 128-132.
18. Zima, T.M., I.A. Vorsina, and N.Z. Lyakhov, *Interaction of poly-N-vinylpyrrolidone with hydrated metal oxides*. Inorganic Materials, 2009. **45**(5): p. 524-532.
19. Lucena, M.d.C.C., et al., *The effect of additives on the thermal degradation of cellulose acetate*. Polymer Degradation and Stability, 2003. **80**(1): p. 149-155.